Freie Universität Berlin

GeoΣim

Atmospheric vortex stability under vertical shear

Dissertation zur Erlangung des Grades
eines Doktors der Naturwissenschaften (Dr. rer. nat.)
am Fachbereich Mathematik und Informatik
der Freien Universität Berlin

vorgelegt von

Ariane Papke

2016

1. Gutachter und Betreuer:
Prof. Dr.-Ing. Rupert Klein

2. Gutachter:
Priv.-Doz. Dr. Peter Névir

Datum der Disputation:
10.02.2017

Acknowledgements

A few years have passed and I am grateful for the many experiences I could make during my PhD studies. I wish to express my gratitude to my advisor Rupert Klein for the opportunity he has given me, his support and fruitful discussions. I am glad that he encouraged me to participate in the 2014 EULAG workshop and become a part of the community. Also, I wish to thank Piotr Smolarkiewicz for his invitation and guidance with EULAG, introducing me to the vast capabilities of the code. Furthermore, I thank Thomas von Larcher for his constructive concepts of tackling coding issues. Many thanks to Peter Spichtinger and Vera Bense for the exchange of even more EULAG details and applications. I would like to thank Stephan Gerber and Patrik Marschalik for their insight and feedback.

GeoSim offered many exciting opportunities and I am deeply grateful for the support received. Fellow members of GeoSim and the Berlin Mathematical School made this time special, we share our interest in science and beyond, meeting at manifold seminars and workshops. I wish to thank Peter Névir for his interest in my work and for reviewing this dissertation.

I wish to thank my parents for their ongoing support and motivation.

I thank Martin for believing in me. For everything we are and will be.

Contents

List of figures

1. Introduction

Processes involving atmospheric vortices cover a vast range of temporal and spatial scales, the underlying mechanisms are difficult to grasp. Creation, development and resilience of such a vortex have been subject of intensive research, e.g. by Dunkerton *et al.* (2009), Frank & Ritchie (1999), Jones (1995) and Reasor & Montgomery (2015). In particular, our focus lies on the spin-up from a tropical storm to hurricane strength. The theory developed by Paeschke *et al.* (2012) gives insight to a new mechanism driving the vortex. Their findings will be the subject of a numerical study.

A commonly used model assumes a Gaussian distribution of vorticity (Reasor & Montgomery, 2001) which well describes tropical cyclones at an incipient stage (Shapiro & Montgomery, 1993, Willoughby, 1990). The setup is constructed along the lines of Reasor & Montgomery (2001) who investigated the alignment process of tilted vortices. Embedded in a geostrophic background we numerically solve the flow equations utilizing Durran's pseudo-incompressible model (Durran, 1989). The flow solver EULAG has been extensively used to model atmospheric flow phenomena, e.g. by Spichtinger & Gierens (2009) and Wedi (2006). Its capability and versatility provide a good basis for our simulations.

We study the interplay of vortex tilt and non-axisymmetric patterns of diabatic heating effects following the analysis of Paeschke *et al.* (2012). The derived evolution equations for centerline and core structure are numerically tested for several regimes.

2. Modeling atmospheric flows

We begin with an introduction to the general framework of atmospheric flows including the governing equations and commonly used approximations and numerical models.

2.1. Framework of the fluid flow

In a first step we present the modeling concepts of fluid flows. In a 3D space spanned by the orthonormal, positively oriented vectors $\boldsymbol{i}, \boldsymbol{j}, \boldsymbol{k}$ we consider at time t a fluid parcel located at $\boldsymbol{x} = (x_1, x_2, x_3)^\top$ with density ρ, pressure p and temperature T. Inside the parcel is a velocity field $\boldsymbol{U}(\boldsymbol{x}, t)$. Due to the movement of the fluid parcel, quantities can be described with respect to the moving frame of reference, or with respect to an absolute origin. These different perspectives are referred to as Lagrangian or Eulerian formulations, respectively. The latter gives a non-trivial total derivative for any quantity $\boldsymbol{C}(\boldsymbol{x}, t)$,

$$\frac{\mathrm{d}\boldsymbol{C}}{\mathrm{d}t} = \frac{\partial \boldsymbol{C}}{\partial t} + \frac{\partial \boldsymbol{C}}{\partial x_n}\frac{\mathrm{d}x_n}{\mathrm{d}t} = \frac{\partial \boldsymbol{C}}{\partial t} + \boldsymbol{U} \cdot \nabla \boldsymbol{C} \tag{2.1.1}$$

where repeatedly occurring indices indicate the use of the Einstein summation convention. Accordingly, this is mostly referred to as the advective derivative:

$$\frac{\mathrm{D}\boldsymbol{C}}{\mathrm{D}t} := \frac{\partial \boldsymbol{C}}{\partial t} + \boldsymbol{U} \cdot \nabla \boldsymbol{C}. \tag{2.1.2}$$

It takes into account the frame of reference when observing changes in time. We choose our origin to be rooted at a fixed point in the Earth's atmosphere, following its rotation. This leaves us with extra terms that need to be added to the acceleration in the rotating frame in order to equal the acceleration seen from a fixed point at rest. Our derivation is along the lines of Holton (2004).
To simplify the notation, we identify the basis vectors with $(\boldsymbol{h}_1, \boldsymbol{h}_2, \boldsymbol{h}_3) = (\boldsymbol{i}, \boldsymbol{j}, \boldsymbol{k})$ and the respective components of a vector with the same indices, i.e. $\boldsymbol{C} = C_n \boldsymbol{h}_n$. The system is rotating with an angular velocity $\boldsymbol{\Omega}$. The inertial frame of reference is spanned by the orthonormal, positively oriented $(\hat{\boldsymbol{h}}_1, \hat{\boldsymbol{h}}_2, \hat{\boldsymbol{h}}_3)$, thus

$$\boldsymbol{C} = C_n \boldsymbol{h}_n = \hat{C}_n \hat{\boldsymbol{h}}_n. \tag{2.1.3}$$

The transformation between both bases is assumed to be isometric.

We can split the expression for the total derivative of any vector $\boldsymbol{C}$ in two parts, one representing the co-moving component. The convective derivative in our frame of reference is

$$\frac{\mathrm{D}\boldsymbol{C}}{\mathrm{D}t} = \frac{\mathrm{D}C_n}{\mathrm{D}t}\boldsymbol{h}_n. \tag{2.1.4}$$

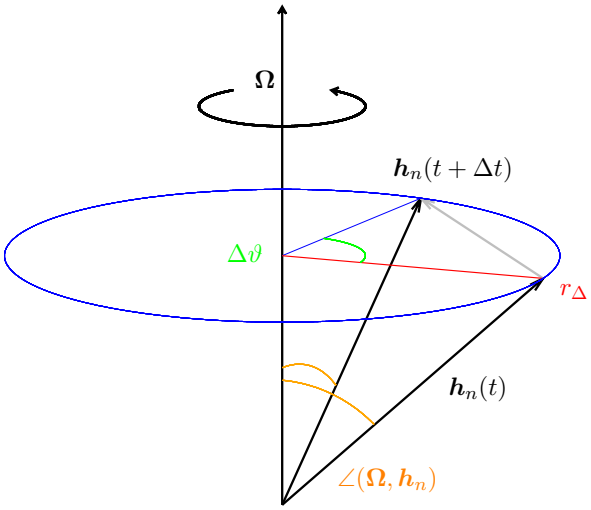

Fig. 2.1.: Rotation of a basis vector $\boldsymbol{h}_n$, displayed at time levels t and $t + \Delta t$. The rotation axis is $\boldsymbol{\Omega}$.

Let $\frac{\hat{\mathrm{D}}}{\hat{\mathrm{D}}t}$ denote the component-wise total derivative with respect to $\hat{\boldsymbol{h}}_n$ in the inertial frame, i.e.

$$\frac{\hat{\mathrm{D}}\boldsymbol{C}}{\hat{\mathrm{D}}t} = \frac{\mathrm{D}\hat{C}_n}{\mathrm{D}t}\hat{\boldsymbol{h}}_n \tag{2.1.5a}$$

$$= \frac{\mathrm{D}C_n}{\mathrm{D}t}\boldsymbol{h}_n + C_n\frac{\hat{\mathrm{D}}\boldsymbol{h}_n}{\hat{\mathrm{D}}t} \tag{2.1.5b}$$

$$= \frac{\mathrm{D}\boldsymbol{C}}{\mathrm{D}t} + C_n\frac{\hat{\mathrm{D}}\boldsymbol{h}_n}{\hat{\mathrm{D}}t}. \tag{2.1.5c}$$

The latter term is discussed following the considerations by Klein & Vater (2003), a sketch of the problem is shown in figure 2.1. Because the basis vectors $\boldsymbol{h}_n$ rotate with the earth, their derivative is non-zero. As mentioned earlier, they only depend on time, i.e. $\boldsymbol{h}_n(t)$, leaving

$$\frac{\hat{\mathrm{D}}\boldsymbol{h}_n}{\hat{\mathrm{D}}t} = \frac{\partial\boldsymbol{h}_n}{\partial t}. \tag{2.1.6}$$

Specifically, to investigate this term further we now set the origin of the inertial frame at the Earth's center, the rotation axis by construction goes through the origin. To calculate the differential quotient

$$\frac{\partial\boldsymbol{h}_n}{\partial t} = \lim_{\Delta t\to 0}\frac{\boldsymbol{h}_n(t+\Delta t) - \boldsymbol{h}_n(t)}{\Delta t} \tag{2.1.7}$$

we now consider an arbitrarily small time interval $\Delta t > 0$, then $\boldsymbol{h}_n$ is rotated by an angle of $\Delta\vartheta = |\boldsymbol{\Omega}|\Delta t$ and changes by $\Delta\boldsymbol{h}_n = \boldsymbol{h}_n(t+\Delta t) - \boldsymbol{h}_n(t)$.

A first order approximation is $|\Delta \boldsymbol{h}_n| = r_\Delta \Delta\vartheta$, the length of the arc that the rotation of $\boldsymbol{h}_n$ around $\boldsymbol{\Omega}$ within Δt describes. The radius r_Δ of this arc is the shortest distance from $\boldsymbol{h}_n$ to the rotation axis, i.e.

$$r_\Delta = \frac{|\boldsymbol{\Omega} \times \boldsymbol{h}_n|}{|\boldsymbol{\Omega}|}. \tag{2.1.8}$$

Higher order terms $\mathcal{O}((\Delta\vartheta)^2)$ are negligible for $\Delta \boldsymbol{h}_n/\Delta t$ in the limit of an infinitesimal time step since also $\Delta\vartheta$ vanishes then with the same speed, because $\Delta\vartheta = |\boldsymbol{\Omega}|\Delta t$.
The direction of $\Delta \boldsymbol{h}_n$ becomes tangential to the described arc in the limit of an infinitesimal time step, i.e. is parallel to $\boldsymbol{\Omega} \times \boldsymbol{h}_n$. Thus, the unit vector is

$$\lim_{\Delta t \to 0} \frac{\Delta \boldsymbol{h}_n}{|\Delta \boldsymbol{h}_n|} = \frac{\boldsymbol{\Omega} \times \boldsymbol{h}_n}{|\boldsymbol{\Omega} \times \boldsymbol{h}_n|}. \tag{2.1.9}$$

Together, we have $r_\Delta = |\boldsymbol{\Omega} \times \boldsymbol{h}_n|\ \Delta t/\Delta\vartheta$ and therefore

$$\lim_{\Delta t \to 0} \frac{\Delta \boldsymbol{h}_n}{\Delta t} = |\boldsymbol{\Omega} \times \boldsymbol{h}_n|\ \frac{\boldsymbol{\Omega} \times \boldsymbol{h}_n}{|\boldsymbol{\Omega} \times \boldsymbol{h}_n|}, \tag{2.1.10}$$

arriving at

$$\frac{\partial \boldsymbol{h}_n}{\partial t} = \boldsymbol{\Omega} \times \boldsymbol{h}_n. \tag{2.1.11}$$

Concluding,

$$C_n \frac{\hat{\mathrm{D}} \boldsymbol{h}_n}{\hat{\mathrm{D}} t} = \boldsymbol{\Omega} \times (C_n \boldsymbol{h}_n) = \boldsymbol{\Omega} \times \boldsymbol{C}. \tag{2.1.12}$$

and for the co-moving total derivative

$$\frac{\hat{\mathrm{D}} \boldsymbol{C}}{\hat{\mathrm{D}} t} = \frac{\mathrm{D} \boldsymbol{C}}{\mathrm{D} t} + \boldsymbol{\Omega} \times \boldsymbol{C}. \tag{2.1.13}$$

2.1.1. Governing equations

To start with, we state here the full system of equations and will derive it in the following paragraphs:

$$\frac{\mathrm{D}\rho}{\mathrm{D}t} + \rho \nabla \cdot \boldsymbol{U} = 0, \tag{2.1.14a}$$

$$\frac{\mathrm{D}\boldsymbol{U}}{\mathrm{D}t} + \frac{1}{\rho}\nabla p + f \boldsymbol{k} \times \boldsymbol{U} = \mathbf{g}, \tag{2.1.14b}$$

$$\frac{\mathrm{D}\Theta}{\mathrm{D}t} = Q_\Theta, \tag{2.1.14c}$$

$$\Theta = \frac{p_{\mathrm{ref}}}{\rho R} \left(\frac{p}{p_{\mathrm{ref}}} \right)^{1/\gamma}. \tag{2.1.14d}$$

We refer to the whole set as the Euler equations. These are conservation of mass, momentum, energy, and a thermodynamic relationship in order to close the system

of equations, leaving six equations for six unknowns $p, \rho, \Theta, \boldsymbol{U}$. Underlying this set of equations is, in the same way as before, an origin that is a fixed point within the fluid domain, i.e. the frame of reference moves with the fluid due to the Earth's rotation. We choose $\boldsymbol{k} = (0,0,1)^\top$ as the vector in vertical direction, instead of referring to $\boldsymbol{x} = (x_1, x_2, x_3)^\top$ we also refer synonymously to $\boldsymbol{x} = (x, y, z)^\top$, and the respective velocities are $\boldsymbol{U} = (u, v, w)^\top$. A useful notation to consider horizontal and vertical components separately is $\boldsymbol{u} = (u, v)^\top$.

2.1.2. Continuity equation

In order to conserve the mass in the system we look at the mass flow. For any fluid element bounded by the area $\mathrm{d}\mathbf{A}$ the mass of fluid flowing through it per unit time is $\rho \boldsymbol{U} \cdot \mathrm{d}\mathbf{A}$, amounting to the total outflow

$$\oint \rho \boldsymbol{U} \cdot \mathrm{d}\mathbf{A}. \tag{2.1.15a}$$

On the other hand, the existing mass in the volume element $\mathrm{d}V$ bounded by $\mathrm{d}\mathbf{A}$ is $\int \rho \, \mathrm{d}V$, thus we observe a decrease per unit time of

$$-\frac{\partial}{\partial t} \int \rho \, \mathrm{d}V. \tag{2.1.15b}$$

Together, the mass flowing out in (2.1.15a) balances the change in mass in (2.1.15b), and it follows with the divergence theorem

$$\int \frac{\partial \rho}{\partial t} + \nabla \cdot (\rho \boldsymbol{U}) \, \mathrm{d}V = 0. \tag{2.1.16}$$

Since this is true for any arbitrarily chosen volume element $\mathrm{d}V$ we arrive at

$$\frac{\partial \rho}{\partial t} + \nabla \cdot (\rho \boldsymbol{U}) = 0. \tag{2.1.17}$$

Finally, in terms of the total derivative, we arrive at the continuity equation (2.1.14a)

$$\frac{\mathrm{D}\rho}{\mathrm{D}t} + \rho \nabla \cdot \boldsymbol{U} = 0.$$

2.1.3. Momentum equation

The full momentum equation is given by

$$(2.1.14b): \qquad \frac{\mathrm{D}\boldsymbol{U}}{\mathrm{D}t} + \frac{1}{\rho} \nabla p + f \boldsymbol{k} \times \boldsymbol{U} = \mathbf{g}, \tag{2.1.18}$$

it is a balance of acceleration, gravity, pressure gradient and Coriolis force per unit mass. We neglect viscosity, i.e. internal friction.

In the Eulerian frame of reference, the acceleration is the convective derivative of the velocity, giving rise to the first term of (2.1.14b). The second term is due to the pressure

exerted by the fluid on a volume element $\mathrm{d}V$ bounded by the surface $\mathrm{d}\mathbf{A}$, rewritten with the divergence theorem

$$-\oint p\,\mathrm{d}\mathbf{A} = -\int \nabla p\,\mathrm{d}V. \tag{2.1.19}$$

Consequently, the force on a unit volume is $-\nabla p$, and the force per unit mass is $-\rho^{-1}\nabla p$.

The term on the right hand side in (2.1.14b) is due to gravity that the fluid experiences. On the scales that we consider, the acceleration $\mathbf{g} = -g\boldsymbol{k}$ is constant with $g = 9.81\mathrm{m\,s^{-2}}$.

Among the "forces" acting on a fluid parcel is also the Coriolis force, an artifact from the choice of the non-inertial reference frame and not negligible on scales comparable to the rotation length scale as considered. Due to the rotation of the Earth with constant angular frequency $\boldsymbol{\Omega}$ a linear trajectory in an inertial frame of references becomes a curved path in a rotating frame.
In equation (2.1.13) we have derived a general transformation law from the view of the inertial reference frame. With the position vector $\boldsymbol{x}$ we find

$$\frac{\hat{\mathrm{D}}\boldsymbol{x}}{\hat{\mathrm{D}}t} = \frac{\mathrm{D}\boldsymbol{x}}{\mathrm{D}t} + \boldsymbol{\Omega}\times\boldsymbol{x}, \quad \text{and since} \quad \frac{\mathrm{D}\boldsymbol{x}}{\mathrm{D}t} \equiv \boldsymbol{U} \tag{2.1.20a}$$

$$\frac{\hat{\mathrm{D}}^2\boldsymbol{x}}{\hat{\mathrm{D}}t^2} = \frac{\mathrm{D}}{\mathrm{D}t}\left(\boldsymbol{U} + \boldsymbol{\Omega}\times\boldsymbol{x}\right) + \boldsymbol{\Omega}\times\left(\boldsymbol{U} + \boldsymbol{\Omega}\times\boldsymbol{x}\right). \tag{2.1.20b}$$

Simplifying the latter equation, reminding that $\boldsymbol{\Omega}$ is constant, gives

$$\frac{\hat{\mathrm{D}}^2\boldsymbol{x}}{\hat{\mathrm{D}}t^2} = \frac{\mathrm{D}\boldsymbol{U}}{\mathrm{D}t} + 2\boldsymbol{\Omega}\times\boldsymbol{U} + \boldsymbol{\Omega}\times(\boldsymbol{\Omega}\times\boldsymbol{x}). \tag{2.1.21}$$

We will omit the last term, the centrifugal acceleration, in these considerations because it is of order $a|\boldsymbol{\Omega}|^2 \approx 1/30\mathrm{ms^{-2}}$ where radius and rotation rate of the Earth are $a = 6.37\cdot 10^6\mathrm{m}$ and $|\boldsymbol{\Omega}| = 7.29\cdot 10^{-5}\mathrm{s^{-1}}$, respectively. This makes it negligible in many cases for atmospheric flows, the extent of the atmosphere is small compared to the Earth's radius. A part of it can also be absorbed in the gravity force,

$$\boldsymbol{\Omega}\times(\boldsymbol{\Omega}\times\boldsymbol{x}) = \boldsymbol{\Omega}(\boldsymbol{\Omega}\cdot\boldsymbol{x}) - \boldsymbol{x}(\boldsymbol{\Omega}\cdot\boldsymbol{\Omega}) \tag{2.1.22}$$

the latter will be parallel to $\mathbf{g}$. Comparing the magnitude of gravitational or centrifugal acceleration is also a good hint that the latter is commonly neglected.
Concluding the momentum balance, the Coriolis acceleration is $-f\boldsymbol{k}\times\boldsymbol{U}$ with the Coriolis parameter $f = 2|\boldsymbol{\Omega}|\sin\varphi$ and latitude φ.

Commonly, the β-plane approximation for the Coriolis parameter is used. In that case, we choose a Cartesian coordinate system where the z-axis is orthogonal to the Earth's surface, x- and y-axis denote the tangential plane. Specifically, x is the zonal and y the meridional coordinate. Consequently, for f we find

$$\frac{\partial f}{\partial x} = 0, \quad \text{but} \quad \frac{\partial f}{\partial y} \neq 0. \tag{2.1.23}$$

Then, the Coriolis parameter is approximated to first order about a reference latitude φ_0,

$$f = f_0 + \beta y, \quad \text{where } \beta = \left.\frac{\mathrm{d}f}{\mathrm{d}y}\right|_{\varphi_0} = \frac{2|\boldsymbol{\Omega}|\cos\varphi_0}{a} \tag{2.1.24}$$

where $y(\varphi_0) = 0$ and β a constant parameter.

2.1.4. Energy equation

Besides mass and momentum the energy of a system is also subject to change. The derivation is conducted along the lines of Holton (2004).

2.1.4.1. Thermodynamics of dry air

Atmospheric air is well described by assuming an ideal gas. The thermodynamics of the atmosphere are fully determined by pressure, density and temperature. Therefore, we revisit the thermodynamic relationships of an ideal gas.
We consider a volume V of a gas with pressure p and temperature T. It consists of N molecules each with a mass of m^*, thus its density is $\rho = Nm^*/V$. The ideal gas law states

$$pV = Nk_\mathrm{B}T, \tag{2.1.25}$$

where $k_\mathrm{B} = 1.38 \cdot 10^{-23}\mathrm{J/K}$ is the Boltzmann constant. This law has been derived from first principles (Nolting, 2014, eq. (1.122)).
For a constant number of molecules the specific heat capacities for an ideal gas at constant volume c_v or constant pressure c_p, respectively, are connected as follows,

$$c_p - c_v = \frac{p}{Nm^*}\left(\frac{\partial V}{\partial T}\right)_{p,N} = \frac{k_\mathrm{B}}{m^*}. \tag{2.1.26}$$

We introduce the specific gas constant $R = k_\mathrm{B}/m^*$ and rewrite (2.1.25) to obtain our equation of state

$$p = \rho RT. \tag{2.1.27}$$

For dry air we find $R = 287\,\mathrm{J\,kg^{-1}K^{-1}}$. This equation will be used to close our system of equations, providing us with as many equations as unknowns.

2.1.4.2. Energy balance

Another conservation law applies to the energy of a system. We consider the transition of a system from and to a thermodynamic equilibrium, specifically the state where no energy or mass is exchanged. The first law of thermodynamics states how internal (E) and kinetic energy ($\boldsymbol{U}\cdot\boldsymbol{U}/2$) change due to heating (rate Q) and work done by external forces such as pressure and gravity, all acting on a unit mass fluid element. Since the Coriolis force is orthogonal to velocity it does not contribute to the energy of the fluid parcel. In the same way as in the momentum equation, we take into account that

the element moves with the flow, and the convective derivative denotes the change in thermodynamic energy, such that the energy balance is:

$$\frac{\mathrm{D}}{\mathrm{D}t}\left(E+\frac{1}{2}\boldsymbol{U}\cdot\boldsymbol{U}\right)=Q-\frac{1}{\rho}\nabla\cdot(p\boldsymbol{U})+\mathbf{g}\cdot\boldsymbol{U}. \tag{2.1.28a}$$

Looking back at (2.1.14b) we can combine these two equations, the first one can be rewritten to

$$\frac{1}{2}\frac{\mathrm{D}}{\mathrm{D}t}(\boldsymbol{U}\cdot\boldsymbol{U})+\frac{1}{\rho}\boldsymbol{U}\cdot\nabla p=\mathbf{g}\cdot\boldsymbol{U}. \tag{2.1.28b}$$

Consequently, from (2.1.28) we get

$$\frac{\mathrm{D}E}{\mathrm{D}t}+\frac{1}{\rho}p\nabla\cdot\boldsymbol{U}=Q. \tag{2.1.29}$$

For dry air the internal energy is $E=c_vT$ where $c_v=717\,\mathrm{J\,kg^{-1}K^{-1}}$. Further taking into account the continuity equation (2.1.14a) and the equation of state (2.1.27), we obtain

$$c_p\frac{\mathrm{D}T}{\mathrm{D}t}-\frac{1}{\rho}\frac{\mathrm{D}p}{\mathrm{D}t}=Q \tag{2.1.30}$$

where $c_p=1004\,\mathrm{J\,kg^{-1}K^{-1}}$, and we remind the specific gas constant $R=c_p-c_v$. The preceding equation is divided by T and rewritten, such that

$$\frac{\mathrm{D}}{\mathrm{D}t}(c_p\ln T-R\ln p)=\frac{Q}{T}. \tag{2.1.31}$$

Regarding (2.1.31) we define the entropy S by

$$\frac{\mathrm{D}S}{\mathrm{D}t}:=\frac{Q}{T}. \tag{2.1.32}$$

2.1.4.3. Potential temperature

A useful quantity to describe adiabatic processes, i.e. reversible and without heat exchange, is the potential temperature Θ. We obtain it from the first law of thermodynamics, i.e. we integrate (2.1.31) from a state (p,T) to $(p_{\mathrm{ref}},\Theta)$ and get

$$\Theta=T\left(\frac{p_{\mathrm{ref}}}{p}\right)^{R/c_p}. \tag{2.1.33}$$

It is the temperature a parcel would obtain if it is adiabatically moved from pressure p to a reference pressure p_{ref}. Although originally designed for adiabatic processes the change of this quantity along a streamline is connected to a heat source or sink via the energy equation (2.1.31). We show this by

$$\frac{\mathrm{D}\Theta}{\mathrm{D}t}=\frac{\Theta}{c_p}\frac{\mathrm{D}S}{\mathrm{D}t}, \tag{2.1.34}$$

which is just another form of (2.1.31), i.e.

$$\frac{\mathrm{D}\Theta}{\mathrm{D}t} = \frac{\Theta}{T}\frac{Q}{c_p} =: Q_\Theta \tag{2.1.35}$$

utilizing the entropy definition (2.1.32) and defining an according heat rate Q_Θ. Thus, the energy conservation of the system is described hereby, heating results in a change of potential temperature.
To close the system of equations we proposed the equation of state (2.1.27), which can be rewritten using the potential temperature,

$$\Theta = \frac{p_{\mathrm{ref}}}{\rho R}\left(\frac{p}{p_{\mathrm{ref}}}\right)^{1/\gamma} \tag{2.1.36}$$

with the isentropic exponent $\gamma = c_p/c_v$. We introduce for the ratio

$$\frac{R}{c_p} = \frac{\gamma - 1}{\gamma} =: \Gamma. \tag{2.1.37}$$

By construction, it is a conserved quantity for (dry) adiabatic processes, i.e. $Q_\Theta = 0$. More specifically, the source term Q_Θ could include dissipation or latent heat release.

2.1.4.4. Exner function

Similarly, we define the Exner pressure π via

$$\pi = \left(\frac{p}{p_{\mathrm{ref}}}\right)^{R/c_p}, \tag{2.1.38}$$

it will enable us to rewrite the pressure gradient in the momentum equations later on.

2.1.5. Geostrophic model

Since the Euler equations are rather complicated to solve there are approximative regimes offering an insight to the flow's dynamics. We introduce the concept of the geostrophic model.

Firstly, we split the momentum conservation with $\boldsymbol{U} = (\boldsymbol{u}, w)^\top$ in horizontal and vertical part,

$$\frac{\partial \boldsymbol{u}}{\partial t} + \boldsymbol{u}\cdot\nabla_\parallel \boldsymbol{u} + w\frac{\partial \boldsymbol{u}}{\partial z} + \frac{1}{\rho}\nabla_\parallel p + f\boldsymbol{k}\times\boldsymbol{u} = 0 \tag{2.1.39a}$$

$$\frac{\partial w}{\partial t} + \boldsymbol{u}\cdot\nabla_\parallel w + w\frac{\partial w}{\partial z} + \frac{1}{\rho}\frac{\partial p}{\partial z} = -g \tag{2.1.39b}$$

where $\nabla_\parallel = \boldsymbol{i}\partial/\partial x + \boldsymbol{j}\partial/\partial y$. Suppressing vertical movement, we recover the *hydrostatic balance*

$$\frac{1}{\rho}\frac{\partial p}{\partial z} = -g. \tag{2.1.40a}$$

Then, for a 2D steady flow the horizontal balance reduces to

$$f\boldsymbol{k} \times \boldsymbol{u}^\dagger = -\frac{1}{\rho}\nabla_\parallel p, \tag{2.1.40b}$$

$\boldsymbol{u}^\dagger$ is the so-called *geostrophic wind* in the according *geostrophic approximation*. In this regime pressure and Coriolis force balance each other, and a simple expression for the velocity is obtained taking the cross product with $\boldsymbol{k}$, remembering $\boldsymbol{k} \times (\boldsymbol{k} \times \boldsymbol{u}^\dagger) = -\boldsymbol{u}^\dagger$:

$$\boldsymbol{u}^\dagger = \boldsymbol{k} \times \frac{1}{f\rho}\nabla_\parallel p. \tag{2.1.41}$$

This allows the definition of a corresponding vorticity. With solely horizontal flow the corresponding *geostrophic vorticity* is

$$q^\dagger = \boldsymbol{k} \cdot \nabla \times \boldsymbol{u}^\dagger. \tag{2.1.42}$$

As a result the velocity field of the flow is determined by the vorticity. Appropriate boundary conditions to solve this inversion will be specified later on for the problem at hand.

Motions that exhibit approximately geostrophic horizontal velocities are called *quasi-geostrophic*. The respective *quasi-geostrophic model* is the result of an asymptotic expansion applied to the hydrodynamic variables, considering first- and leading-order terms of the Euler equations (2.1.14). Beyond the hydrostatic balance (2.1.40a), geostrophic balance (2.1.40b) and vorticity (2.1.42), it comprises of an anelastic constraint and transport of potential temperature and vorticity. Hence, the model equations give rise to the evolution in time and cover also higher orders of velocities and potential temperature. A detailed derivation of the quasi-geostrophic model is provided by Paeschke *et al.* (2012), it is well-suited for atmospheric synoptic-scale motions.

2.2. Stability of atmospheric flows

While the dynamics of the atmosphere are generally determined by the Euler equations, specific cases can be singled out. Any quantity that characterizes the fluid flow can separately describe a certain state and its deviation from it. This background state is commonly stationary, i.e. without fluid motion, and beyond this there are three szenarios:

(i) Returning to equilibrium, a stable state;

(ii) Moving away from equilibrium, an unstable state;

(iii) Remaining in equilibrium, a neutral state.

Along the lines of Durran (2010) we will discuss at this point the implications that arise specifically for atmospheric flows.

Firstly, we introduce another formulation of the Euler equations (2.1.14). With the new pressure variable π (2.1.38), the pressure gradient in (2.1.14b) can be transformed to

$$\frac{1}{\rho}\nabla p = c_p \Theta \nabla \pi, \tag{2.2.1}$$

and the rewritten Euler equations for the six unknowns $\boldsymbol{U}, \rho, \Theta$ and π are

$$\frac{\mathrm{D}\rho}{\mathrm{D}t} + \rho \nabla \cdot \boldsymbol{U} = 0, \tag{2.2.2a}$$

$$\frac{\mathrm{D}\boldsymbol{U}}{\mathrm{D}t} + c_p \Theta \nabla \pi + f \boldsymbol{k} \times \boldsymbol{U} = \mathbf{g}, \tag{2.2.2b}$$

$$\frac{\mathrm{D}\Theta}{\mathrm{D}t} = Q_\Theta, \tag{2.2.2c}$$

$$\pi = \left(\frac{\rho R \Theta}{p_{\mathrm{ref}}} \right)^{\gamma - 1}. \tag{2.2.2d}$$

2.2.1. Background state

Let $\overline{\pi}$ and $\overline{\Theta}$ denote a state with no vertical fluid motion, then from the third component of (2.2.2b) we get the hydrostatic balance

$$c_p \overline{\Theta} \frac{\mathrm{d}\overline{\pi}}{\mathrm{d}z} = -g. \tag{2.2.3}$$

Specifically, we choose the state variables $(\overline{\pi}, \overline{\rho}, \overline{\Theta})$ as the respective horizontally averaged quantities, leaving only a dependence on the vertical coordinate z,

$$\pi = \overline{\pi}(z) + \pi'(x, y, z, t), \tag{2.2.4a}$$

$$\Theta = \overline{\Theta}(z) + \Theta'(x, y, z, t). \tag{2.2.4b}$$

In turn, utilizing the hydrostatic balance (2.2.3), the momentum equations (2.2.2b) transform to

$$\frac{\mathrm{D}\boldsymbol{U}}{\mathrm{D}t} + c_p \Theta \nabla \pi' + f \boldsymbol{k} \times \boldsymbol{U} = -\mathbf{g} \frac{\Theta'}{\overline{\Theta}}. \tag{2.2.5}$$

2.2.2. Approximative regime

Some simplifications to the Euler equations allow us to learn more about the dynamics of the flow under the imposed assumptions. A rigorous analysis of selected approximations is given in section 2.3.

While the continuity equation stands for mass conservation,

$$\nabla \cdot \boldsymbol{U} = 0 \tag{2.2.6a}$$

describes volume conservation and follows from (2.2.2a) for flows with $\dfrac{\mathrm{D}\rho}{\mathrm{D}t} = 0$ that we refer to as *incompressible*. The flow behaves according to the transformed momentum

equations (2.2.5), and specifically for a constant reference potential temperature Θ_0 we find

$$\frac{\mathrm{D}\boldsymbol{U}}{\mathrm{D}t} + c_p\Theta_0\nabla\pi' + f\boldsymbol{k}\times\boldsymbol{U} = -\mathbf{g}\frac{\Theta'}{\Theta_0}, \tag{2.2.6b}$$

while still $\Theta' = \Theta - \overline{\Theta}$, we retain the variation in the bouyancy term.
A last equation describing this specific flow, and closing the system without needing the equation of state, is the energy equation (2.2.2c), with the decomposition:

$$\frac{\mathrm{D}\Theta'}{\mathrm{D}t} + w\frac{\mathrm{d}\overline{\Theta}}{\mathrm{d}z} = Q_\Theta. \tag{2.2.6c}$$

Together, this set of equations (2.2.6) is called the Boussinesq system.

2.2.3. Internal waves

We recover wave equations under the Boussinesq approximation that lead us to the question in the beginning: how will a deviation from the background state evolve?
To get an insight, we combine the vertical momentum equation (2.2.6b) and the energy balance (2.2.6c), assuming that the deviation is small and the background state remains undisturbed, i.e. $\pi = \overline{\pi}$ and leaving

$$\frac{\mathrm{D}w}{\mathrm{D}t} = g\frac{\Theta'}{\Theta_0}. \tag{2.2.7}$$

From the energy equation, we also obtain an expression for the vertical velocity,

$$\frac{\mathrm{D}\Theta'}{\mathrm{D}t} = -w\frac{\mathrm{d}\overline{\Theta}}{\mathrm{d}z}, \tag{2.2.8}$$

we insert this in (2.2.7) after applying $\frac{\mathrm{D}}{\mathrm{D}t}$,

$$\frac{\mathrm{D}^2w}{\mathrm{D}t^2} = -\frac{g}{\Theta_0}\frac{\mathrm{d}\overline{\Theta}}{\mathrm{d}z}\,w. \tag{2.2.9}$$

Thus, the vertical velocity follows a wave equation of frequency

$$N = \sqrt{\frac{g}{\Theta_0}\frac{\mathrm{d}\overline{\Theta}}{\mathrm{d}z}} \tag{2.2.10}$$

that is the bouyancy frequency, also referred to as *Brunt-Väisälä frequency*. The resulting waves are called gravity waves. We deduct that any small state deviation will evolve according to the sign and amplitude of N^2. If the potential temperature $\overline{\Theta}(z)$ decreases with height, we find exponential growth, while an increase with height gives rise to an oscillation about the equilibrium state. We refer to the atmosphere as stably or unstably stratified, respectively. A stationary state is found for neutral stratification, i.e. constant potential temperature.

With this knowledge we can rewrite the governing equations (2.2.6)

$$\nabla \cdot \boldsymbol{U} = 0 \tag{2.2.11a}$$

$$\frac{\mathrm{D}\boldsymbol{U}}{\mathrm{D}t} + \nabla P^{\prime} + f\boldsymbol{k} \times \boldsymbol{U} = G^{\prime}\boldsymbol{k} \tag{2.2.11b}$$

$$\frac{\mathrm{D}G^{\prime}}{\mathrm{D}t} + N^2 w = Q_\Theta \frac{g}{\Theta_0} \tag{2.2.11c}$$

introducing

$$P^{\prime} = c_p \Theta_0 \pi^{\prime}, \quad G^{\prime} = g\frac{\Theta^{\prime}}{\Theta_0}. \tag{2.2.12}$$

Beyond the Brunt-Väisälä frequency that focuses on vertical motion we are interested in the wave-like behavior of the whole system, giving rise to general internal waves. In particular, we restrict our analysis to an adiabatic flow and linear effects. This motivates a traveling wave ansatz of the form

$$(\boldsymbol{U}^\top, P^{\prime}, G^{\prime}) = (\hat{\boldsymbol{U}}^\top, \hat{P}^{\prime}, \hat{G}^{\prime}) e^{\imath(\mathbf{a}\cdot\boldsymbol{x} - \psi t)}, \tag{2.2.13}$$

with wavenumbers $\mathbf{a} = (a, b, c)$ and frequency ψ. Coriolis and bouyancy frequency are regarded as constant within this approach, emphasized as f_0 and N_0. We linearize the advective derivative in (2.2.11) with respect to a background state with a constant wind field $\mathbf{U}^{\prime}$ and insert the wave solutions, obtaining the linear system,

$$\begin{pmatrix} a & b & c & 0 & 0 \\ \imath\left(\mathbf{U}^{\prime}\cdot\mathbf{a} - \psi\right) & -f_0 & 0 & \imath a & 0 \\ f_0 & \imath\left(\mathbf{U}^{\prime}\cdot\mathbf{a} - \psi\right) & 0 & \imath b & 0 \\ 0 & 0 & \imath\left(\mathbf{U}^{\prime}\cdot\mathbf{a} - \psi\right) & \imath c & -1 \\ 0 & 0 & N_0^2 & 0 & \imath\left(\mathbf{U}^{\prime}\cdot\mathbf{a} - \psi\right) \end{pmatrix} \begin{pmatrix} \hat{u} \\ \hat{v} \\ \hat{w} \\ \hat{P}^{\prime} \\ \hat{G}^{\prime} \end{pmatrix} = 0. \tag{2.2.14}$$

A non-trivial solution to this linear problem is obtained looking at the determinant, which vanishes if

$$\left(\psi - \mathbf{U}^{\prime}\cdot\mathbf{a}\right)^2 = \frac{f_0^2 c^2 + (a^2 + b^2) N_0^2}{a^2 + b^2 + c^2}. \tag{2.2.15}$$

This *dispersion relation* determines phase ($\mathbf{v}_p$) and group velocity ($\mathbf{v}_g$) by

$$\mathbf{a}\cdot\mathbf{v}_p = \psi, \qquad \mathbf{v}_g = \nabla_{\mathbf{a}}\,\psi. \tag{2.2.16}$$

Given the frequency, one can also deduct the characteristic time scale of internal waves via

$$t_{\text{internal}} = \frac{2\pi}{\psi}, \tag{2.2.17}$$

the scaling factor with the constant number π arises from the traveling wave ansatz.

Besides the constant advection speed and wave numbers, the frequency of an internal wave depends on the Coriolis and the Brunt-Väisälä frequency. Its envelope propagates with the corresponding group velocity and we find that its deviation from the background state is orthogonal to the wave vector, i.e.

$$\mathbf{a} \cdot \left(\mathbf{v}_g - \mathbf{U}^l \right) = 0. \tag{2.2.18}$$

It follows from the derivative of the angular frequency (2.2.15) according to (2.2.16),

$$\nabla_{\mathbf{a}} \psi = \mathbf{U}^l \pm \frac{c \left(N_0^2 - f_0^2 \right)}{|\mathbf{a}|^4 \left(\psi - \mathbf{U}^l \cdot \mathbf{a} \right)} \begin{pmatrix} ac \\ bc \\ -(a^2 + b^2) \end{pmatrix} \tag{2.2.19}$$

for $\psi \neq \mathbf{U}^l \cdot \mathbf{a}$.

2.3. Numerical models

Atmospheric flows are well described by the Euler equations (2.2.2), however they cannot be solved by analytical means and we need numerical methods to solve them. There are different approximations to the Euler equations that are well suitable for atmospheric flows and solving them turns out to be more efficient than solving the full set of equations. To be precise, sound waves are incorporated in the Euler equations, and although their influence on the dynamics of the atmosphere is small, they dictate a small time step in a numerical model as their time scale is the smallest compared to other processes Klein (2010). Therefore, some models have been introduced that filter negligible sound waves, so called soundproof models. We will present them following the considerations of Klein (2009).

To start with, we bring (2.2.2) in conservative form by subsequently applying the continuity equation, transforming the advective derivative and using the tensor product $\boldsymbol{U} \circ \boldsymbol{U}$, such that

$$\rho_t + \nabla \cdot (\rho \boldsymbol{U}) = 0, \tag{2.3.1a}$$

$$(\rho \boldsymbol{U})_t + \nabla \cdot (\rho \boldsymbol{U} \circ \boldsymbol{U}) + c_p \rho \Theta \nabla \pi + f \boldsymbol{k} \times \rho \boldsymbol{U} = -\rho g \boldsymbol{k}, \tag{2.3.1b}$$

$$(\rho \Theta)_t + \nabla \cdot (\rho \Theta \boldsymbol{U}) = \rho Q_\Theta, \tag{2.3.1c}$$

$$\pi = \left(\frac{\rho R \Theta}{p_{\text{ref}}} \right)^{\gamma - 1}, \tag{2.3.1d}$$

while the differentiation in time is indicated by the lower index t.

2.3.1. Rescaling

To account for different scales it is necessary to first nondimensionalize the involved variables with respect to characteristic values of the quantities in the atmosphere. We choose the reference values $[p_{\text{ref}}, \rho_{\text{ref}}, T_{\text{ref}}, g_{\text{ref}}]$ for pressure, density, gravitational constant and potential temperature as repeating variables and apply Buckingham's Π theorem (Kundu

& Cohen, 2002). Nondimensional quantities, as they arise from the theorem, are denoted with a check, we remind the equation of state that relates the reference quantities and arrive at

$$\overset{\star}{\rho}_{\overset{\star}{t}} + \overset{\star}{\nabla} \cdot (\overset{\star}{\rho}\overset{\star}{\boldsymbol{U}}) = 0, \tag{2.3.2a}$$

$$(\overset{\star}{\rho}\overset{\star}{\boldsymbol{U}})_{\overset{\star}{t}} + \overset{\star}{\nabla} \cdot (\overset{\star}{\rho}\overset{\star}{\boldsymbol{U}} \circ \overset{\star}{\boldsymbol{U}}) + \frac{1}{\Gamma}\overset{\star}{\rho}\overset{\star}{\Theta}\overset{\star}{\nabla}\overset{\star}{\pi} + \overset{\star}{f}\boldsymbol{k} \times \overset{\star}{\rho}\overset{\star}{\boldsymbol{U}} = -\overset{\star}{\rho}\overset{\star}{g}\boldsymbol{k}, \tag{2.3.2b}$$

$$(\overset{\star}{\rho}\overset{\star}{\Theta})_{\overset{\star}{t}} + \overset{\star}{\nabla} \cdot (\overset{\star}{\rho}\overset{\star}{\Theta}\overset{\star}{\boldsymbol{U}}) = \overset{\star}{\rho}\overset{\star}{Q}_{\Theta}, \tag{2.3.2c}$$

$$\overset{\star}{\pi} = (\overset{\star}{\rho}\overset{\star}{\Theta})^{\gamma-1}. \tag{2.3.2d}$$

Reminding the definition of Γ in (2.1.37), the nondimensional equation of state is $\overset{\star}{p}^{\Gamma} = \overset{\star}{\pi}$, and thus we have $\overset{\star}{p}^{1/\gamma} = \overset{\star}{\rho}\overset{\star}{\Theta}$. We point out the nondimensional distance, velocity and time. For any space variable we found for its coefficient

$$\frac{p_{\mathrm{ref}}}{\rho_{\mathrm{ref}}\, g_{\mathrm{ref}}} =: h_{\mathrm{sc}}, \tag{2.3.3a}$$

which is the pressure scale height. As for velocity, the factor is

$$\sqrt{\frac{p_{\mathrm{ref}}}{\rho_{\mathrm{ref}}}} =: c_{\mathrm{ref}}, \tag{2.3.3b}$$

up to $\sqrt{\gamma}$ equal to the speed of sound. However, the speed of sound is not a good measure for atmospheric velocities since they are usually much smaller, and our goal is to eliminate the acoustic waves. Instead, we introduce another nondimensional quantity, the Mach number

$$\mathrm{M} := \frac{u_{\mathrm{ref}}}{c_{\mathrm{ref}}} \tag{2.3.3c}$$

that relates a suitable velocity scale u_{ref} to the speed of sound. Up to a rescaling factor the presented dimensionless quantities are identical with the nondimensional products that are obtained with Buckingham's method. With these definitions, time scales with $t_{\mathrm{ref}} = h_{\mathrm{sc}}/c_{\mathrm{ref}}$. While discussing numerical models we will focus on adiabatic flows. Nevertheless, it is worthwhile to take a look at the heating rate $\overset{\star}{Q}_{\Theta}$ for later reference. With an appropriate scaling factor $Q_{\Theta,\mathrm{ref}}$ we recover the Damköhler number

$$\mathrm{Da} := \frac{t_{\mathrm{ref}}}{T_{\mathrm{ref}}}\, Q_{\Theta,\mathrm{ref}}. \tag{2.3.3d}$$

The dimensionless system in (2.3.2) then becomes

$$\rho_t + \nabla \cdot (\rho \boldsymbol{U}) = 0, \tag{2.3.4a}$$

$$(\rho\boldsymbol{U})_t + \nabla \cdot (\rho\boldsymbol{U} \circ \boldsymbol{U}) + \frac{1}{\Gamma}\rho\Theta\nabla\pi + f\boldsymbol{k} \times \rho\boldsymbol{U} = -\rho g\boldsymbol{k}, \tag{2.3.4b}$$

$$(\rho\Theta)_t + \nabla \cdot (\rho\Theta\boldsymbol{U}) = 0, \tag{2.3.4c}$$

$$\pi = (\rho\Theta)^{\gamma-1}, \tag{2.3.4d}$$

for simplicity dropping the star from here on only for this chapter. We refer to (2.3.4) as the *compressible* model. In a next step, we will discuss approximations to these equations.

Continuity, momentum and energy equations are approximated with regards to a specific expansion parameter, comparable to Klein (2009) we choose it based on the Mach number M. We aim to expand our variables with respect to M, and therefore rescale time and velocity in (2.3.4) according to (2.3.3c),

$$t_{\mathrm{ref}} = \frac{h_{\mathrm{sc}}}{u_{\mathrm{ref}}} \quad \text{with} \quad u_{\mathrm{ref}} = \mathrm{M}c_{\mathrm{ref}}. \tag{2.3.5}$$

Only the shape of the momentum equation changes under this transformation to

$$(\rho \boldsymbol{U})_t + \nabla \cdot (\rho \boldsymbol{U} \circ \boldsymbol{U}) + \frac{1}{\mathrm{M}^2}\frac{1}{\Gamma}\rho\Theta\nabla\pi + f\boldsymbol{k} \times \rho\boldsymbol{U} = -\frac{g}{\mathrm{M}^2}\rho\boldsymbol{k}. \tag{2.3.6}$$

In the subsequent asymptotic framework the scales are narrowed down to the advection time scale t_{ref} and the pressure scale height h_{sc}. For low Mach number flows, i.e. $\mathrm{M} \to 0$, we then state the expansion scheme

$$\pi(\boldsymbol{x}, t; \mathrm{M}) = \overline{\pi}(z) + \mathrm{M}^2\pi'(\boldsymbol{x}, t) + o(\mathrm{M}^2) \tag{2.3.7a}$$
$$\rho(\boldsymbol{x}, t; \mathrm{M}) = \overline{\rho}(z) + \mathrm{M}^2\rho'(\boldsymbol{x}, t) + o(\mathrm{M}^2) \tag{2.3.7b}$$
$$\Theta(\boldsymbol{x}, t; \mathrm{M}) = \overline{\Theta}(z) + \mathrm{M}^2\Theta'(\boldsymbol{x}, t) + o(\mathrm{M}^2) \tag{2.3.7c}$$
$$\boldsymbol{U}(\boldsymbol{x}, t; \mathrm{M}) = \boldsymbol{U}_0(\boldsymbol{x}, t) + o(1) \tag{2.3.7d}$$

that we will exploit in the following. Regarding (2.3.6) we recover the hydrostatic balance in leading order

$$\frac{1}{\Gamma}\overline{\Theta}\frac{\mathrm{d}\overline{\pi}}{\mathrm{d}z} = -g \tag{2.3.8}$$

that has also been obtained by the decomposition in section 2.2.1.

2.3.2. Pseudo-incompressible model

The first case that we will consider is the pseudo-incompressible approximation proposed by Durran (1989, 2008).
To start with, we define the *pseudo-incompressible* density ρ^* that fulfills

$$\overline{\pi} = (\rho^*\Theta)^{\gamma-1}. \tag{2.3.9}$$

Accordingly, it is connected to the density as

$$\rho = \rho^* \left(\frac{\pi}{\overline{\pi}}\right)^{\frac{1}{\gamma-1}}. \tag{2.3.10}$$

The assumption of Durran's pseudo-incompressible model is that $\mathrm{M}^2\pi' \ll \overline{\pi}$ (Durran, 1989), i.e. the pressure deviation from the background state is small. Then, (2.3.10) can be linearized,

$$\rho = \rho^* \left(1 + \mathrm{M}^2\frac{\pi'}{\overline{\pi}} + o(\mathrm{M}^2)\right)^{\frac{1}{\gamma-1}} \approx \rho^* \left(1 + \frac{\mathrm{M}^2}{\gamma-1}\frac{\pi'}{\overline{\pi}}\right), \tag{2.3.11}$$

and in leading order we have

$$\rho^* \Theta = \overline{\rho}\overline{\Theta}, \tag{2.3.12}$$

the mean variables satisfy an equation of state.
To obtain a soundproof model we filter the effect of pressure deviations on density, and the mass conservation (2.3.4a) reads

$$\rho^*_t + \nabla \cdot (\rho^* \boldsymbol{U}) = 0. \tag{2.3.13a}$$

Considering momentum in (2.3.6), we make use of (2.3.12) and the hydrostatic balance (2.3.8), expanding Θ and π, and drop higher order terms,

$$(\rho^* \boldsymbol{U})_t + \nabla \cdot (\rho^* \boldsymbol{U} \circ \boldsymbol{U}) + \frac{1}{\Gamma}\overline{\rho}\overline{\Theta}\nabla\pi + f\boldsymbol{k} \times \rho^* \boldsymbol{U} = -\rho^* g \boldsymbol{k} \tag{2.3.13b}$$

having rescaled it back to the original nondimensional variables from Buckingham's Π theorem. For the energy conservation (2.3.4c) we remind the definition of the pseudo-density in (2.3.9), in leading order the pressure is steady. With the same preceding considerations, we arrive at

$$\nabla \cdot (\overline{\rho}\overline{\Theta}\boldsymbol{U}) = 0. \tag{2.3.13c}$$

Together, (2.3.13) represent the pseudo-incompressible model. Compared to the compressible model (2.3.4) we have a time independent leading-order pressure and $\rho\Theta = \overline{\rho}\overline{\Theta}(z)$.

2.3.3. Anelastic models

Subsequently, we will consider anelastic models, several approximations of this kind have been introduced, attaining different goals. Regarding the specific numerical model that we will apply in the progress of this thesis, we focus on the proposed model of Lipps & Hemler (1982) and the Boussinesq approximation. At this point, we expand all variables according to their form in (2.3.7).

2.3.3.1. Lipps & Hemler's model

Then, to leading order the continuity equation in (2.3.4a) is

$$\nabla \cdot (\overline{\rho}\, \boldsymbol{U}_0) = 0, \tag{2.3.14}$$

which is also called *anelastic* compressibility. Similarly, we make use of (2.3.8) and consider the zeroth order of (2.3.6), giving

$$(\overline{\rho}\boldsymbol{U}_0)_t + \nabla \cdot (\overline{\rho}\boldsymbol{U}_0 \circ \boldsymbol{U}_0) + \frac{1}{\Gamma}\overline{\rho}\nabla(\overline{\Theta}\pi') + f\boldsymbol{k} \times \overline{\rho}\boldsymbol{U}_0 = \overline{\rho} g \frac{\Theta'}{\overline{\Theta}}\boldsymbol{k} \tag{2.3.15}$$

where we used the assumption of weak potential temperature stratification as proposed by Lipps & Hemler (1982) to simplify

$$\overline{\Theta}\nabla\pi' = \nabla(\overline{\Theta}\pi') - \pi'\nabla\overline{\Theta}. \tag{2.3.16}$$

The last term is of lower order and omitted, assuming that the stratification behaves like

$$\frac{1}{\overline{\Theta}}\frac{\mathrm{d}\overline{\Theta}}{\mathrm{d}z} = \mathcal{O}\left(\mathrm{M}^2\right). \tag{2.3.17}$$

For the potential temperature evolution (2.3.4c) we find in second order

$$(\overline{\rho}\Theta')_t + \nabla\cdot(\overline{\rho}\Theta'\boldsymbol{U}_0) = 0 \tag{2.3.18}$$

utilizing zeroth order results of this equation, and the zeroth and second order of the continuity equation (2.3.4a). Concluding, (2.3.14), (2.3.15) and (2.3.18) motivate the anelastic model of Lipps & Hemler (1982)

$$\nabla\cdot(\overline{\rho}\boldsymbol{U}) = 0, \tag{2.3.19a}$$

$$(\overline{\rho}\boldsymbol{U})_t + \nabla\cdot(\overline{\rho}\boldsymbol{U}\circ\boldsymbol{U}) + \frac{1}{\Gamma}\overline{\rho}\nabla(\overline{\Theta}\pi') + f\boldsymbol{k}\times\overline{\rho}\boldsymbol{U} = \overline{\rho}g\frac{\Theta'}{\overline{\Theta}}\boldsymbol{k}, \tag{2.3.19b}$$

$$(\overline{\rho}\Theta')_t + \nabla\cdot(\overline{\rho}\Theta'\boldsymbol{U}) = 0. \tag{2.3.19c}$$

While in the pseudo-incompressible model we assumed a steady pressure to leading order, we here find a similar restriction for the density, and additionally weak temperature stratification is a condition. In fact, with the asymptotic expansion scheme (2.3.7) the leading-order of the energy equation (2.3.4c) requires that for stronger mean stratification than (2.3.17) internal waves are suppressed in the low Mach number limit.

2.3.3.2. Boussinesq approximation

Another class of an anelastic model is the Boussinesq approximation that has been applied in section 2.2.2 already. At this point, we target low Mach number flows, thus the representation here is a reduced variant of (2.2.6). It comprises the anelastic equations (2.3.19) and additionally assumes a small density variation, essentially requiring a constant $\overline{\rho}$. Further, we account for the small variation in potential temperature by replacing $\overline{\Theta}$ with Θ_0 in the anelastic model, however retaining the variation in the bouyancy force due to stratification:

$$\nabla\cdot\boldsymbol{U} = 0, \tag{2.3.20a}$$

$$\boldsymbol{U}_t + \boldsymbol{U}\cdot\nabla\boldsymbol{U} + \frac{1}{\Gamma}\Theta_0\nabla\pi' + f\boldsymbol{k}\times\boldsymbol{U} = g\frac{\Theta'}{\Theta_0}\boldsymbol{k}, \tag{2.3.20b}$$

$$\Theta'_t + \boldsymbol{U}\cdot\nabla\Theta' = 0. \tag{2.3.20c}$$

2.3.4. Validity

While the presented models were constructed in the same spirit, to filter sound waves, they rely on different conditions. For the anelastic model we need a time independent leading-order density and a weakly stratified potential temperature distribution, whereas the pseudo-incompressible model assumes a steady pressure to leading order and is also

valid for large density and potential temperature variations.

For a detailed discussion on the suitability of these models when modeling atmospheric flows we refer to Klein *et al.* (2010). Via a scale analysis they argue that for typical conditions in the atmosphere the compressible, pseudo-incompressible and anelastic model provide a good approximation to the low Mach number flow.

3. Implementation

So far we have presented analytical means to model atmospheric flows, while in the present chapter we focus on the numerical implementation. The computational model EULAG[1] has been successfully applied to a plethora of environmental systems, among others Charbonneau & Smolarkiewicz (2013), Prusa *et al.* (2008), Rosa *et al.* (2011), Spichtinger & Gierens (2009). It can handle Eulerian and Lagrangian frameworks, adaptive moving meshes, generalized coordinates, just to name a few capabilities. In order to solve the underlying set of differential equations an elliptic solver (Smolarkiewicz & Margolin, 1994) is coupled with an advection scheme (Smolarkiewicz & Margolin, 1998), also with a non-oscillatory option (Smolarkiewicz & Grabowski, 1990).

We will investigate vortical flows in the atmosphere and start with an overview of the advection algorithm, followed by a few words on the structure of the code and some of the applied methods. Lastly, we use a well-known 2D test-case to double-check the performance of EULAG on vortical flows.

3.1. Computational framework

EULAG offers besides the compressible also the anelastic model by Lipps and Hemler, cf. section 2.3.3.1 consistent with Smolarkiewicz & Margolin (1997) and Smolarkiewicz *et al.* (2001), and Durran's pseudo-incompressible model, cf. 2.3.2, see (Prusa *et al.*, 2008, Smolarkiewicz & Dörnbrack, 2008).

3.1.1. Flow solver

An introduction to the flow solver is given along the lines of Smolarkiewicz (1984). The explicit method with optional extensions is presented in great detail in Smolarkiewicz & Margolin (1998). It is designed to solve the transport equation for a scalar variable $\Psi(\boldsymbol{x}, t)$, e.g.

$$\frac{\partial G\Psi}{\partial t} + \nabla \cdot (\boldsymbol{U}\Psi) = GR, \tag{3.1.1}$$

where $R(\boldsymbol{x}, t)$ takes the role of a source or combines forcings (Smolarkiewicz, 1991) and $G(\boldsymbol{x}, t)$ accounts for curvilinearity of coordinates (Smolarkiewicz & Margolin, 1993). The density is part of either G, Ψ or R, depending on the model type (Smolarkiewicz, 2006). In the original idea Ψ was required to be nondiffusive and nonnegative.
Advective terms are approximated by the multidimensional positive definite advection transport algorithm (MPDATA), a generally sign-preserving, conservative scheme and a

[1] The name EULAG indicates its capability to solve equations in both the Eulerian and Lagrangian framework.

correction to the upwind method. For finite-difference algorithms such as MPDATA the *Courant number* C is an important measure for the stability and numerical diffusion of the method. Its local value for a grid cell of size Δx_I in the Ith dimension is

$$C_{\text{loc}} = \Delta t \sum_{I=1}^{3} \frac{U_{I,\text{loc}}}{\Delta x_I} \tag{3.1.2}$$

with a time step Δt. A necessary condition for the original upwind scheme to be stable is that the Courant number is everywhere smaller than unity, for solenoidal flow fields it is even sufficient, while for divergent ones the bound is 0.5 (Smolarkiewicz, 1984). MPDATA inherits this condition for stability at least in our scope, for a thorough discussion the reader is referred to (Smolarkiewicz & Szmelter, 2005).

Varying the number of corrective steps $IORD - 1$ influences the rate of convergence of the algorithm, i.e. for $IORD = 1$ we recover first-order upwind and $IORD = 2$ results in a second-order scheme in time and space, the standard MPDATA. Increasing the number of iterations only gives a higher order of accuracy in space but not in time (Smolarkiewicz, 1984).

Another point of discussion is the change of the convergence rate with the Courant number. The value $C = 0.5$ rises a non-trivial artifact for $IORD = 3$ and $IORD = 4$, indicating a third-order accuracy (Smolarkiewicz, 1984, Smolarkiewicz & Grabowski, 1990).

With a slight modification, MPDATA can handle quantities with variable sign, specifically of interest for the transport of momenta. The so-called "infinite-gauge" stems from the asymptotic form of MPDATA when (3.1.1) is extended, such that

$$\frac{\partial G(\Psi + A\chi)}{\partial t} + \nabla \cdot (\boldsymbol{U}(\Psi + A\chi))) = GR \tag{3.1.3}$$

and the limit $A \to \infty$ is observed. We added the mass conservation equation A times that is obtained from (3.1.1) by replacing ψ with χ and adjusting the variables to the respective system. Originally presented by Smolarkiewicz & Clark (1986), it has been generalized in Smolarkiewicz & Margolin (1998) to this form and named MPDATM in EULAG. As a consequence, the method is not sign preserving anymore, but its approximation is better: The test case with $IORD = 2$ and nonvanishing A is in good agreement with $IORD = 3$ for $A = 0$. A further increase in the number of iterations gives only slight improvement and typically $IORD = 2$ suffices. The appearing deviations can be accounted for by extending MPDATM to a non-oscillatory forward-in-time (NFT) algorithm (Smolarkiewicz & Grabowski, 1990) preserving monotonicity as proposed by Smolarkiewicz & Margolin (1998). In the spirit of a flux-corrected transport (FCT) algorithm the pseudo velocities are modified, they correspond to the advection of the diffusive error in the donor-cell scheme. It has been shown by Smolarkiewicz & Grabowski (1990) that the convergence rate is only slightly diminished. Concluding, when momenta are to be advected numerically a viable option is non-oscillatory MPDATM.

To visualize the different behavior we conduct a series of 1D tests with uniform grid and velocity for both with and without the variable sign variant. The 1D setup is borrowed from Klein (2009), however we build it on a number of cell-rows in two dimensions in EULAG. Technically, the levels in the second dimension do not differ. An initial distribution $c(x,t)$ of a scalar quantity, e.g. a chemical species, is advected by a constant velocity field $(u,v) = (1,0)$. Gravity and other external forces and diffusion are neglected, and the conservation equation reads

$$\frac{\partial c}{\partial t} + u\frac{\partial c}{\partial x} = 0. \tag{3.1.4}$$

Since the chemical species is passively advected, i.e. does not influence velocity, pressure, density or temperature, the conservation equations remain unchanged. The only difference is that now the evolution of $c(x,t)$ is added to the system of equations. In that way, only advection plays a role and we observe the evolution calculated by MPDATA. In this simple case we recover the Courant number

$$C = u\frac{\Delta t}{\Delta x}. \tag{3.1.5}$$

We observe the performance of non-oscillatory MPDATA and MPDATM on four different cases mentioned in Klein (2009), depending on the Courant number: a rectangle, a triangle, a parabola and a cosine-shaped distribution are advected. The number of grid points is $n = 152$ in streamwise and $l = 3$ in perpendicular direction. Periodic boundary conditions are imposed. We fix the spatial increments and the background velocity, but vary the time step in order to have different Courant numbers. Therefore, roughly 10 periods have passed after

$$t_e = 10\left\lfloor \frac{(n-1)}{C} \right\rfloor \Delta t. \tag{3.1.6}$$

Background density, temperature and pressure are assumed to be constant justifying the use of the anelastic Boussinesq system in EULAG. The advected distributions are shown in figure 3.1.

3.1.2. Elliptic solver

Besides advection the Euler equations contain more terms that need to be accounted for when solving them numerically. The conservation equations are reformulated to obtain an elliptic equation for the pressure that is solved with a preconditioned conjugate residual (CR) scheme (Prusa & Smolarkiewicz, 2003, Smolarkiewicz & Margolin, 1994, Smolarkiewicz *et al.*, 2004).

3.1.3. Operator splitting

We have now introduced two different solvers that can each handle a specific part of the Euler equations well. Normally, they are designed to calculate the solution at time $n+1$ starting from the integer time level n. However, it is intuitive to look at them separately and consider them at an intermediate time level $n + 1/2$ (Smolarkiewicz,

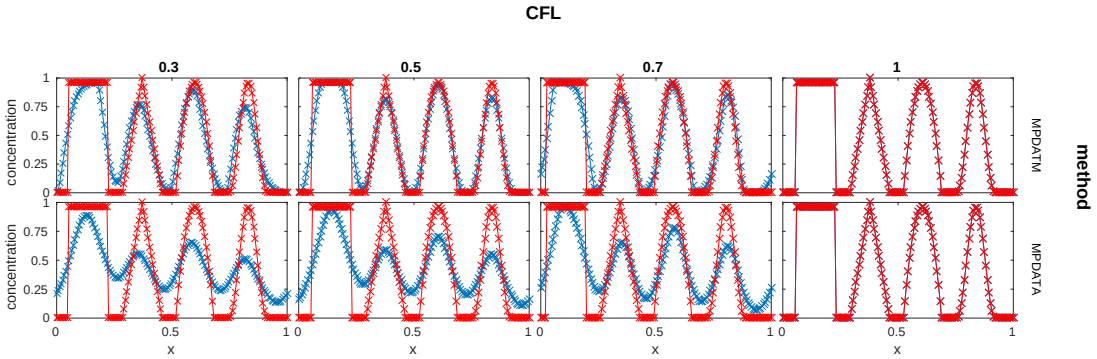

Fig. 3.1.: Distribution after t_e with $u = 1\text{ms}^{-1}$ and $\Delta t \in \{15\text{s}, 25\text{s}, 35\text{s}, 50\text{s}\}$, the number of grid points is $n = 152$ in streamwise and $l = 3$ in perpendicular direction. The horizontal axis x is normalized by its maximum value. The red curve is the advected analytical distribution, blue denotes the numerical result.

1991, Smolarkiewicz & Margolin, 1993). This kind of operator splitting resembles the one proposed by Strang (1968) (Smolarkiewicz & Margolin, 1998, Smolarkiewicz & Szmelter, 2005).
To be more precise, the idea in EULAG in each time step is the following: Firstly, half the forcing is added to the fields, therefore accounting for half of the forcing operator. Secondly, the resulting fields are advected. Lastly, another half of a forcing operator is applied, but this time utilizing the elliptic CR scheme.

3.1.4. Initial and boundary conditions

A background state is initialized in EULAG, there are several options implemented to choose from and they specifically fulfill the conditions requested in some of the common models for atmospheric flows. We point out the one designed for the anelastic model of Clark & Farley (1984): The equation of state and the definition of potential temperature are linearized and expressions for $\overline{\Theta}(z), \overline{p}(z)$ and $\overline{\rho}(z)$ are derived. Potential temperature is decreasing exponentially with height and depends on the constant stability parameter s,

$$\overline{\Theta}(z) = \Theta_0\, e^{sz}, \tag{3.1.7a}$$

and the density follows

$$\overline{\rho}(z) = \overline{\rho}_0\, e^{-sz} \left[1 - \frac{g}{c_p s \Theta_0}\left(1 - e^{-sz}\right)\right]^{1/(\gamma-1)}. \tag{3.1.7b}$$

It will be used in a later course of this work.

In addition to initial conditions also boundary conditions are imposed to solve the underlying set of equations, discretized on a finite grid. One can choose between periodic and open boundary conditions, the latter rather meaning that the variables attain a

certain value in accordance with the predefined background state. Optionally, one can request no-slip boundaries.

3.1.5. Sponge layer

In a stably stratified atmosphere vertical movement is suppressed, however internal waves can be part of the solution and disturb this balance. In the case of a Neumann condition incoming waves are reflected at the boundary. Atmospheric flows however are not bounded, and the idea is to imitate an infinite domain, specifically suppressing reflection. This motivates a sponge layer in the vicinity of the edge absorbing these kind of disturbances. While it can be placed along any of the edges we present the basic idea in the horizontal direction x. Waves are absorbed if a suitable term is added to the evolution equation within this layer. For example, they could be included by "viscosity" or "friction" (Israeli & Orszag, 1981). The latter is also known as Rayleigh damping (Durran, 2010) and filters a broader range of waves. Generally, we have a damping profile $\tau(x)$ determining what kind of waves are absorbed (Klemp & Lilly, 1978). Setting up the absorber correctly is crucial, otherwise waves will not dissipate sufficiently.

In EULAG the Rayleigh sponge damping field is utilized (Clark, 1977, Smolarkiewicz & Margolin, 1998) and the damping profile is characterized by the layer thickness D_R and the absorber time scale t_R in each dimension. Therefore, we utilize the time and spatial scales typical for gravity waves explained in 2.2.3. If we aim to suppress vertical motion we need to look at the vertical propagation of the internal waves. Equation (2.2.15) indicates that the frequency spectrum is dominated by the Coriolis and the Brunt-Väisälä frequency determining the time scale $t_\mathrm{R} = 2\pi/\psi$ by (2.2.17). The thickness should be chosen with regards to a dominating wavelength $\boldsymbol{\lambda}_\mathrm{R}$ (Klemp & Lilly, 1978) that is obtained from frequency and group velocity (2.2.19), therefore $\boldsymbol{\lambda}_\mathrm{R} = t_\mathrm{R}\mathbf{v}_g$.
In case of a still environmental state the analysis yields a vanishing layer, however we allow for disturbances to this state and can consider this as an estimate.

3.2. Suitability for vortical flows

A series of tests for two-dimensional setups is conducted, borrowed from Klein (2009) and Kadioglu *et al.* (2008) to double-check EULAG's performance on concentrated vortical flows.

3.2.1. Setup

In order to construct a consistent setup we will determine how, for a specific problem, the variables $\boldsymbol{U}$, p and Θ are connected. In case of vortical flows rotation is involved, and we will utilize a rotating frame of reference with constant angular frequency $\boldsymbol{\Omega}$ to arrive at a relation between velocity and pressure. So as to derive this balance the frequency proves useful, it is connected to other variables via the transformation rule (2.1.13). It will not play a role in the numerical test.

Firstly, we consider a three-dimensional space spanned by the perpendicular unit vectors $\boldsymbol{i}, \boldsymbol{j}$ and $\boldsymbol{k}$, and an inviscid fluid of density ρ, pressure p and temperature T. The location and velocity field of a fluid parcel are $\boldsymbol{x} = (x, y, z)^\top$ and $\boldsymbol{U} = (\boldsymbol{u}, w)^\top$, respectively. Conservation of mass (2.1.14a) and energy (2.1.14c) are assumed for an adiabatic flow and neglecting gravity the momentum balance in an inertial frame is

$$\frac{\hat{\mathrm{D}}^2 \boldsymbol{x}}{\hat{\mathrm{D}}t^2} + \frac{1}{\rho}\nabla p = 0. \tag{3.2.1}$$

The co-moving frame rotates with a constant angular frequency $\boldsymbol{\Omega}$ and is subject to horizontal translation relatively to the inertial frame. We assume rotation takes place in a 2D subspace with center $\mathbf{X}(t)$, $\boldsymbol{\Omega} = \mathbf{X}(t) + |\boldsymbol{\Omega}| \cdot \boldsymbol{k}$, and introduce polar coordinates $(r, \vartheta)^\top$ with respect to the orthonormal basis vectors $\boldsymbol{e}_r$ and $\boldsymbol{e}_\vartheta$, each perpendicular to $\boldsymbol{k}$, such that the transformation is given by

$$\boldsymbol{r}(\boldsymbol{x}) = \boldsymbol{x} - \mathbf{X}, \quad \vartheta = \arctan\left(\frac{y - \mathrm{Y}}{x - \mathrm{X}}\right). \tag{3.2.2}$$

Then, for the radius $\boldsymbol{r}$ we find

$$\frac{\hat{\mathrm{D}}\boldsymbol{r}}{\hat{\mathrm{D}}t} = \frac{\hat{\mathrm{D}}\boldsymbol{x}}{\hat{\mathrm{D}}t} - \frac{\hat{\mathrm{D}}\mathbf{X}}{\hat{\mathrm{D}}t} = \boldsymbol{U} - \boldsymbol{U}_0 \quad \text{defining} \quad \boldsymbol{U}_0 := \frac{\hat{\mathrm{D}}\mathbf{X}}{\hat{\mathrm{D}}t}. \tag{3.2.3a}$$

Accordingly, we introduce the difference velocity

$$\boldsymbol{U}_* := \boldsymbol{U} - \boldsymbol{U}_0 \tag{3.2.3b}$$

that has the property

$$\boldsymbol{U}_* = \frac{\hat{\mathrm{D}}\boldsymbol{r}}{\hat{\mathrm{D}}t} = \frac{\mathrm{D}\boldsymbol{r}}{\mathrm{D}t} + \boldsymbol{\Omega} \times \boldsymbol{r}, \tag{3.2.3c}$$

utilizing the transformation rule (2.1.13) for a rotating frame of reference. If the radius was changing within the rotating system it would contradict the steadiness of $\boldsymbol{\Omega}$ or the constant distance between origin and rotation axis. Therefore, by construction we have

$$\boldsymbol{U}_* = \boldsymbol{\Omega} \times \boldsymbol{r}. \tag{3.2.4}$$

Taking a step towards the momentum equation we differentiate with respect to time again and with (3.2.3) it holds

$$\frac{\hat{\mathrm{D}}^2 \boldsymbol{x}}{\hat{\mathrm{D}}t^2} = \frac{\hat{\mathrm{D}}\boldsymbol{U}_*}{\hat{\mathrm{D}}t} + \frac{\hat{\mathrm{D}}\boldsymbol{U}_0}{\hat{\mathrm{D}}t}. \tag{3.2.5}$$

Clearly, $\boldsymbol{U}_0$ accounts for advection of the rotation axis that in our case of interest is set to be uniform, i.e.

$$\frac{\hat{\mathrm{D}}\boldsymbol{U}_0}{\hat{\mathrm{D}}t} = 0. \tag{3.2.6}$$

Further, again from (2.1.13) we obtain

$$\frac{\hat{\mathrm{D}}\boldsymbol{U}_*}{\hat{\mathrm{D}}t} = \frac{\mathrm{D}\boldsymbol{U}_*}{\mathrm{D}t} + \boldsymbol{\Omega} \times \boldsymbol{U}_*, \tag{3.2.7}$$

and $\boldsymbol{U}_*$ is, with the same reasoning as for $\boldsymbol{r}$, uniform in the co-moving framework, cf. the derivative of (3.2.4) and remember that $\boldsymbol{\Omega}$ is constant in space and time with respect to the rotating frame. Consequently, this leaves us with the centrifugal acceleration

$$\frac{\hat{\mathrm{D}}^2\boldsymbol{x}}{\hat{\mathrm{D}}t^2} = \boldsymbol{\Omega} \times \boldsymbol{U}_* \quad \text{where} \quad (3.2.4) \quad \boldsymbol{U}_* = \boldsymbol{\Omega} \times \boldsymbol{r}. \tag{3.2.8}$$

For the specific case of interest only a horizontal subspace is considered, i.e. $\boldsymbol{r} \perp \boldsymbol{\Omega}$. Note that for any $\boldsymbol{x}_\parallel \perp \boldsymbol{\Omega}$ it is

$$\boldsymbol{\Omega} \times (\boldsymbol{\Omega} \times \boldsymbol{x}_\parallel) = \boldsymbol{\Omega}(\boldsymbol{\Omega} \cdot \boldsymbol{x}_\parallel) - \boldsymbol{x}_\parallel(\boldsymbol{\Omega} \cdot \boldsymbol{\Omega}) = -|\boldsymbol{\Omega}|^2\boldsymbol{x}_\parallel. \tag{3.2.9}$$

It simplifies the right hand side of (3.2.8) to

$$\boldsymbol{\Omega} \times (\boldsymbol{\Omega} \times \boldsymbol{r}) = \boldsymbol{\Omega}(\boldsymbol{\Omega} \cdot \boldsymbol{r}) - \boldsymbol{r}(\boldsymbol{\Omega} \cdot \boldsymbol{\Omega}) = -\frac{|\boldsymbol{U}_*|^2}{r}\boldsymbol{e}_r \tag{3.2.10a}$$

since

$$\boldsymbol{r} \times \boldsymbol{U}_* = \boldsymbol{r} \times (\boldsymbol{\Omega} \times \boldsymbol{r}) = \boldsymbol{\Omega}(\boldsymbol{r} \cdot \boldsymbol{r}) - \boldsymbol{r}(\boldsymbol{r} \cdot \boldsymbol{\Omega}) \quad \text{such that} \quad \boldsymbol{\Omega} = \frac{\boldsymbol{r} \times \boldsymbol{U}_*}{r^2} \tag{3.2.10b}$$

where $r := |\boldsymbol{r}|$ and $\boldsymbol{U}_* \perp \boldsymbol{r}$ by definition. Lastly, concerning the momentum balance (3.2.1) we also express the pressure gradient in polar coordinates. The recent considerations have shown that only a radially symmetric pressure distribution is consistent with the case, and inserting (3.2.8) with (3.2.10) in (3.2.1) we arrive at

$$\frac{|\boldsymbol{U}_*|^2}{r}\boldsymbol{e}_r = \frac{1}{\rho}\frac{\mathrm{d}p}{\mathrm{d}r}\boldsymbol{e}_r. \tag{3.2.11}$$

Concluding, the case that we study is described by this momentum balance and conservation of mass (2.1.14a) and energy (2.1.14c).
The system is nondimensionalized with respect to $[p_{\mathrm{ref}}, \rho_{\mathrm{ref}}, T_{\mathrm{ref}}, x_{\mathrm{ref}}]$, typical values are $T_{\mathrm{ref}} = 300\,\mathrm{K}$, $p_{\mathrm{ref}} = 10^5\,\mathrm{Pa}$ and, for an ideal gas, $\rho_{\mathrm{ref}} \approx 1.1614\,\mathrm{kg/m^2}$. Similar to 2.3.1 we rescale the velocity with the Mach number and introduce $u_{\mathrm{ref}} = \mathrm{M}c_{\mathrm{ref}}$, such that time is $t = \overset{\star}{t}x_{\mathrm{ref}}/u_{\mathrm{ref}} = \overset{\star}{t}x_{\mathrm{ref}}/\mathrm{M}c_{\mathrm{ref}}$ and velocity $\boldsymbol{U} = u_{\mathrm{ref}}\overset{\star}{\boldsymbol{U}} = \mathrm{M}c_{\mathrm{ref}}\overset{\star}{\boldsymbol{U}}$. Further, the radius is rescaled with a nondimensional factor $\mathring{R}$, i.e. $r = \overset{\star}{r} \cdot x_{\mathrm{ref}} \cdot \mathring{R}$. Then, the nondimensional form is

$$\overset{\star}{\rho}_{\overset{\star}{t}} + \overset{\star}{\nabla} \cdot (\overset{\star}{\rho}\overset{\star}{\boldsymbol{U}}) = 0, \tag{3.2.12a}$$

$$\overset{\star}{\rho}\frac{|\overset{\star}{\boldsymbol{U}} - \overset{\star}{\boldsymbol{U}}_0|^2}{\overset{\star}{r}} - \frac{1}{\mathrm{M}^2}\frac{\mathrm{d}\overset{\star}{p}}{\mathrm{d}\overset{\star}{r}} = 0, \tag{3.2.12b}$$

$$\overset{\star}{P}_{\overset{\star}{t}} + \overset{\star}{\nabla} \cdot (\overset{\star}{P}\overset{\star}{\boldsymbol{U}}) = 0, \tag{3.2.12c}$$

where

$$\overset{\star}{P} := \overset{\star}{p}^{1/\gamma} = \overset{\star}{\rho}\overset{\star}{\Theta} \tag{3.2.12d}$$

is the equation of state.

3.2.2. Initial state

We assume a constant, isothermal and balanced background state with the aforementioned reference values for an ideal gas.

A vortex of fixed radius $\mathring{R}$ is placed inside a domain of length and width x_{ref}, $\overset{\star}{\mathbf{X}}(t)$ denotes its center. Initially in the middle of the domain, it is advected with a velocity $\overset{\star}{\boldsymbol{u}}_0 = (\overset{\star}{u}_0, \overset{\star}{v}_0)$, such that

$$\overset{\star}{\mathbf{X}}(\overset{\star}{t}) = \frac{1}{2}(\boldsymbol{i} + \boldsymbol{j}) + \overset{\star}{t} \cdot \overset{\star}{\boldsymbol{u}}_0. \tag{3.2.13}$$

A density profile $\overset{\star}{\rho}(\overset{\star}{r})$ and a velocity field $\overset{\star}{\boldsymbol{u}}(\overset{\star}{r}, \vartheta, t)$ are prescribed, fully describing the initial state: pressure is obtained from the conservation of momentum (3.2.12b) and temperature follows from the equation of state (3.2.12d).

A density variation as follows is imposed

$$\overset{\star}{\rho}(\overset{\star}{r}) = \begin{cases} \overset{\star}{\rho}_c + \frac{1}{2}\left(1 - \overset{\star}{r}^2\right)^6 & \overset{\star}{r} \leq 1 \\ \overset{\star}{\rho}_c & \overset{\star}{r} > 1 \end{cases} \tag{3.2.14}$$

and the divergence-free velocity field $\boldsymbol{u} = (u, v)^\top$ reads

$$\overset{\star}{u}(\overset{\star}{r}, \vartheta) = \begin{cases} \overset{\star}{u}_0 - 1024(1 - \overset{\star}{r})^6 \overset{\star}{r}^6 \sin\vartheta & \overset{\star}{r} \leq 1 \\ \overset{\star}{u}_0 & \overset{\star}{r} > 1 \end{cases} \tag{3.2.15a}$$

$$\overset{\star}{v}(\overset{\star}{r}, \vartheta) = \begin{cases} \overset{\star}{v}_0 + 1024(1 - \overset{\star}{r})^6 \overset{\star}{r}^6 \cos\vartheta & \overset{\star}{r} \leq 1 \\ \overset{\star}{v}_0 & \overset{\star}{r} > 1 \end{cases}. \tag{3.2.15b}$$

The parameters $\overset{\star}{u}_0, \overset{\star}{v}_0$ and $\overset{\star}{\rho}_c$ are constant, let $\overset{\star}{\rho}_c = 0.5$ and $\overset{\star}{\boldsymbol{u}}_0 = (1, 0)$. Then, the vortex is advected horizontally. Solving equation (3.2.12b) gives the pressure perturbation $\overset{\star}{p}_*$ that is necessary to balance the rotational movement, such that the vortex is steady, depending on density distribution and velocity field, for $0 < \overset{\star}{R} \leq 1$:

$$
\begin{aligned}
\frac{\overset{\star}{p}_*(\overset{\star}{R})}{\mathrm{M}^2} &= \int_1^{\overset{\star}{R}} \overset{\star}{\rho}(\overset{\star}{r})\, \frac{|\overset{\star}{\boldsymbol{u}}(\overset{\star}{r},\vartheta) - \overset{\star}{\boldsymbol{u}}_0|^2}{\overset{\star}{r}}\, \mathrm{d}\overset{\star}{r} \\
&= \int_1^{\overset{\star}{R}} \left(\frac{1}{2} + \frac{1}{2}\left(1 - \overset{\star}{r}^2\right)^6\right) \frac{1024^2 (1-\overset{\star}{r})^{12} \overset{\star}{r}^{12}}{\overset{\star}{r}}\, \mathrm{d}\overset{\star}{r} \\
&= 1024^2 \left(\overset{\star}{R}^{12} \left[\frac{1}{12} - \frac{12\overset{\star}{R}^1}{13} + \frac{9\overset{\star}{R}^2}{2} - \frac{184\overset{\star}{R}^3}{15} + \frac{609\overset{\star}{R}^4}{32} - \frac{222\overset{\star}{R}^5}{17} \right.\right. \\
&\quad - \frac{38\overset{\star}{R}^6}{9} + \frac{54\overset{\star}{R}^7}{19} + \frac{783\overset{\star}{R}^8}{20} - \frac{558\overset{\star}{R}^9}{7} + \frac{1053\overset{\star}{R}^{10}}{22} + \frac{1014\overset{\star}{R}^{11}}{23} \\
&\quad - \frac{1473\overset{\star}{R}^{12}}{16} + \frac{204\overset{\star}{R}^{13}}{5} + \frac{510\overset{\star}{R}^{14}}{13} - \frac{1564\overset{\star}{R}^{15}}{27} + \frac{153\overset{\star}{R}^{16}}{8} + \frac{450\overset{\star}{R}^{17}}{29} \\
&\quad \left. - \frac{269\overset{\star}{R}^{18}}{15} + \frac{174\overset{\star}{R}^{19}}{31} + \frac{57\overset{\star}{R}^{20}}{32} - \frac{74\overset{\star}{R}^{21}}{33} + \frac{15\overset{\star}{R}^{22}}{17} - \frac{6\overset{\star}{R}^{23}}{35} + \frac{\overset{\star}{R}^{24}}{72} \right] \\
&\quad \left. - \frac{34373}{1805044411170} \right)
\end{aligned}
\tag{3.2.16}
$$

where $\overset{\star}{p}_*(1) = 0$. The full pressure profile $\overset{\star}{p}$ is then given by

$$
\overset{\star}{p}(\overset{\star}{r}) = \begin{cases} 1 + \mathrm{M}^2\, \overset{\star}{p}_*(\overset{\star}{r}) & \overset{\star}{r} \le 1 \\ 1 & \overset{\star}{r} > 1 \end{cases}, \tag{3.2.17a}
$$

and the corresponding potential temperature $\overset{\star}{\Theta}$ is

$$
\overset{\star}{\Theta}(\overset{\star}{r}) = \begin{cases} \left(1 + \mathrm{M}^2\, \overset{\star}{p}_*(\overset{\star}{r})\right)^{1/\gamma} / \overset{\star}{\rho}(\overset{\star}{r}) & \overset{\star}{r} \le 1 \\ 1/\overset{\star}{\rho}_c & \overset{\star}{r} > 1 \end{cases}. \tag{3.2.17b}
$$

We choose $\mathring{R} = 0.4$ and the reference values $u_{\mathrm{ref}} = 1\mathrm{ms}^{-1}$ and $x_{\mathrm{ref}} = 1\mathrm{m}$. The dimensional form of the initial velocities (3.2.15), pressure and potential temperature (3.2.17) is depicted in figure 3.2.

3.2.3. Numerical model

In order to solve this problem now in EULAG we need to choose a numerical model among the ones presented in 2.3 and feed it with our initial data. We consider a low Mach-number flow and choose u_{ref} accordingly. A review of the pseudo-incompressible model deems it well-suited for the underlying case, since $\overset{\star}{P}_{\overset{\star}{t}}$ is negligible:

$$
\overset{\star}{P}_{\overset{\star}{t}} = (\overset{\star}{u}_0 \cos\vartheta + \overset{\star}{v}_0 \sin\vartheta)\overset{\star}{P}_{\overset{\star}{r}}, \quad \text{where} \tag{3.2.18}
$$

$$
\overset{\star}{P}_{\overset{\star}{r}} = \partial_{\overset{\star}{r}} \overset{\star}{p}^{1/\gamma} = \frac{1}{\gamma} \overset{\star}{p}^{-1+1/\gamma} \partial_{\overset{\star}{r}} \overset{\star}{p} \tag{3.2.19}
$$

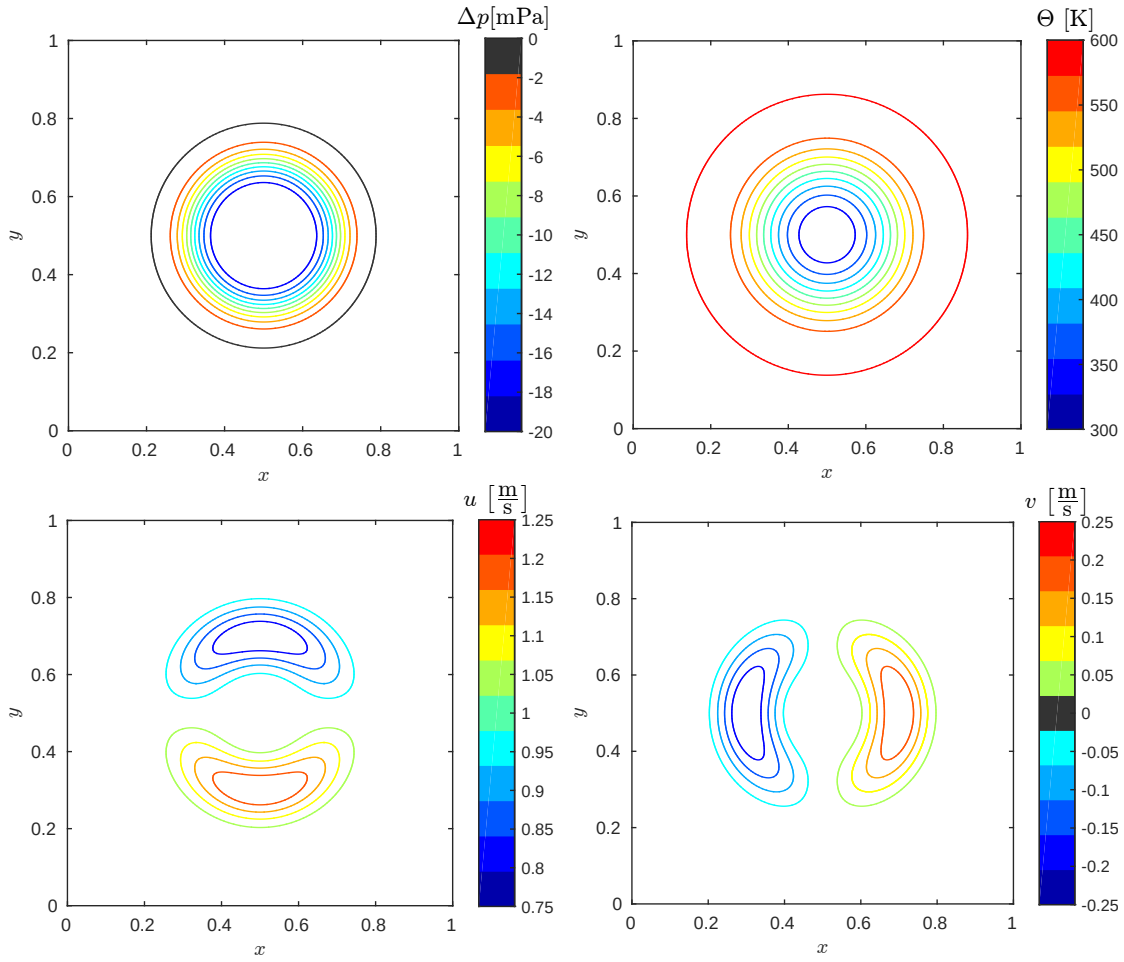

Fig. 3.2.: Initial state of the vortex. Pressure difference $\Delta p = p - p_{\text{ref}}$ (top left), potential temperature Θ (top right), horizontal velocity u (bottom left) and vertical velocity w (bottom right) are shown. Note that 1mPa= 10^{-3}Pa.

and $\partial^{\star}_{r^{\star}}\tilde{p} \sim \mathcal{O}(\mathrm{M}^2)$.

The domain is discretized on a grid with 256×256 points and $\Delta x = \Delta y = 255^{-1}\mathrm{m}$. The time step is chosen in a way that the Courant number is bounded by 0.45, i.e.

$$\Delta t = \Delta x \, \frac{0.45}{1 + 0.25\,\mathrm{m}} \frac{\mathrm{s}}{\mathrm{m}} \approx 1.2 \cdot 10^{-3}\mathrm{s}. \tag{3.2.20}$$

3.2.4. Consistency

In EULAG the initial velocities and potential temperature are set according to (3.2.15) and (3.2.17b). We gain the discrete pressure $p^{\diamond}$ for the specific problem utilizing the construction of the flow solver. Initially, the pressure field is constant, e.g. $p^{\diamond}_0 \equiv p_{\mathrm{ref}}$. Subsequently, we consistently set the pressure to the correct value: After the first time step the discretized pressure is updated to

$$p^{\diamond}_{1/2} = \frac{1}{2}\left(p^{\diamond}_0 + p^{\diamond}_1\right), \tag{3.2.21}$$

the subscripts indicate the time level. The initial pressure $p^{\diamond}_0$ and the pressure after one time step $p^{\diamond}_1$ are linearly interpolated in order to gain the pressure at an intermediate time level $1/2$. The general forcings are handled in the same way,

$$R^{\diamond}_{1/2} = \frac{1}{2}\left(R^{\diamond}_0 + R^{\diamond}_1\right). \tag{3.2.22}$$

Consequently, in the second time step the intermediate forcing and pressure are the starting point to calculate the variable $\Psi^{\diamond}_2$, followed by the regular sequence of half explicit forcing, advection and half implicit forcing. At every time the pressure and forcing are half a step behind, i.e. after $n+1$ time steps we have $\Psi^{\diamond}_{n+1}$ but $p^{\diamond}_{n+1/2}$ and $R^{\diamond}_{n+1/2}$. In this way the pressure distribution is determined with help of the elliptic solver matching the state dynamics, it is further only subject to advection.

Concluding, in the second time step we arrive at a pressure as in (3.2.17a). It solves the momentum equation and depends only on the absolute value of the radius. Therefore, we expect that the pressure field is solely advected, as the vortex center is, and its shape remain unchanged.

3.2.5. Results

The vortex is advected over roughly one period, i.e. for a time

$$t_e = 20 \left\lfloor \frac{256 - 1}{20} \frac{\mathrm{s}^2}{\mathrm{m}} \frac{\Delta x}{\Delta t} \right\rfloor. \tag{3.2.23}$$

In that way, 20 time splits of one period are available. The final fields of velocities, pressure and potential temperature are shown in figure 3.3. They differ only slightly from the initial state. We gain a deeper insight subtracting the initial fields, cf. figure 3.2, that evolve according to (3.2.13). This means that we compare the final fields with

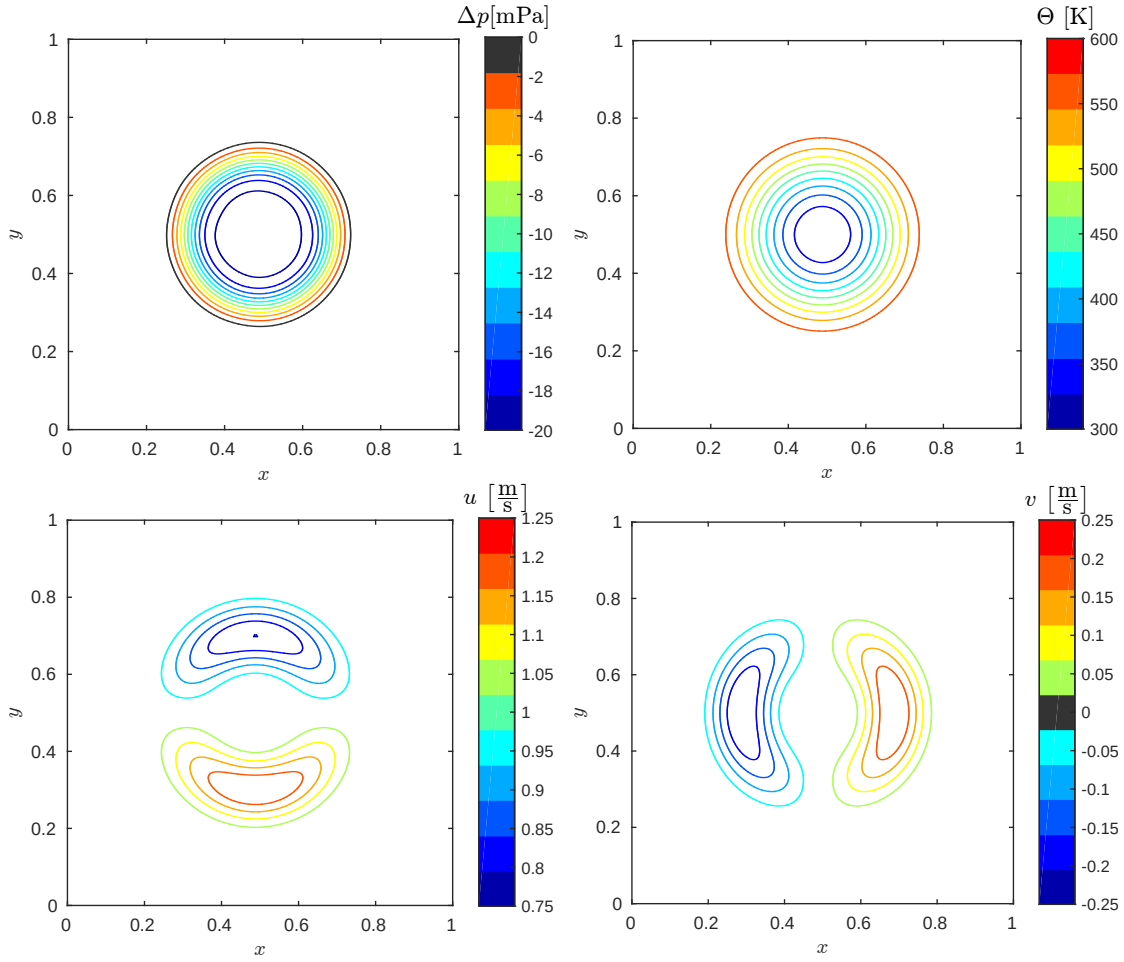

Fig. 3.3.: Horizontally advected vortex. Same variables as in figure 3.2 but after $t = t_e$.

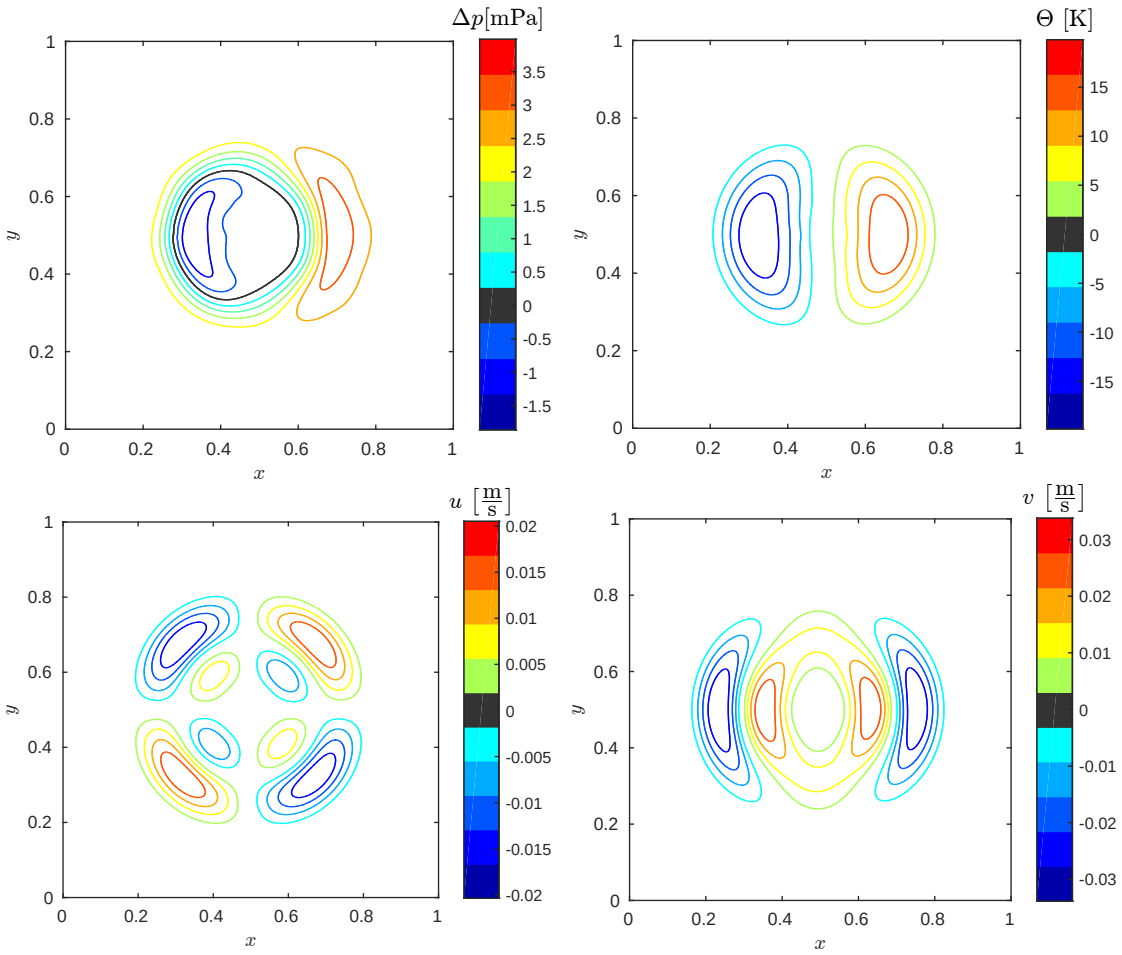

Fig. 3.4.: Difference fields, initial state with $t = 0$ is subtracted from the final state with $t = t_e$.

the analytically advected initial fields at the same point in time. Hence, an exact determination of one period, matching the positions of final and initial fields, is not necessary. The difference fields are pictured in 3.4. Compared to the order of magnitude of the respective variables the error is small, yet non-negligible. Specifically, the pressure deviates the strongest after t_e. This is not astonishing since the maximum deviation from the background state is still much smaller than p_{ref}. We investigate this further and analyze the intermediate states of pressure and potential temperature. Good measures for their evolution are the mean value and the standard deviation, figure 3.5 distinguishes them over one period for the available time splits. We observe that the potential temperature distribution is only subject to small changes, while the pressure changes notably for $t/t_2 < 0.4$. As for the mean value the slightest pressure oscillations influence it strongly, it is small and changes sign. The curve of the standard deviation allows a clear distinction when the pressure is an almost perfect match to the other variables. The fact that the pressure only reaches this state after some time is due to smallest errors in the initialization.
To sum it up, the characteristic state variables of the vortex are advected with minor errors and EULAG is well suited to model vortical flows.

3.3. Averaging techniques

Extending the previous 2D example to three dimensions leads to the question of certain vortex specific quantities such as the centerline and the circumferential velocity. Initially the vortex is embedded in a geostrophic environment and exhibits certain symmetries that serve specific averaging methods that we present in the following.

3.3.1. Vortex centerline

Beyond the initial state the vortex is subject to advection, gravity, pressure and Coriolis force. The core of the vortex is a measure for its position, and in order to describe its evolution we need to determine the center. Rotational flow has a non-vanishing curl, and the vorticity

$$\boldsymbol{\omega}(\boldsymbol{x}, t) = \nabla \times \boldsymbol{U}(\boldsymbol{x}, t) \tag{3.3.1}$$

is a quantity of interest. More precisely, the vortex initially exhibits a vertical rotation axis, therefore we restrict ourselves to the vertical component of vorticity when determining the vortex center. In the style of the center of mass calculation we consider ω_3 as density function and get the horizontal components of the eye location in the domain Σ for each level,

$$\mathrm{X}(z, t) = \frac{1}{\Omega(z, t)} \int_{\Sigma} x\omega_3(x, y, z, t)\, \mathrm{d}(x, y) \tag{3.3.2a}$$

$$\mathrm{Y}(z, t) = \frac{1}{\Omega(z, t)} \int_{\Sigma} y\, \omega_3(x, y, z, t)\, \mathrm{d}(x, y) \tag{3.3.2b}$$

normalized by

$$\Omega(z, t) = \int_{\Sigma} \omega_3(x, y, z, t)\, \mathrm{d}(x, y). \tag{3.3.2c}$$

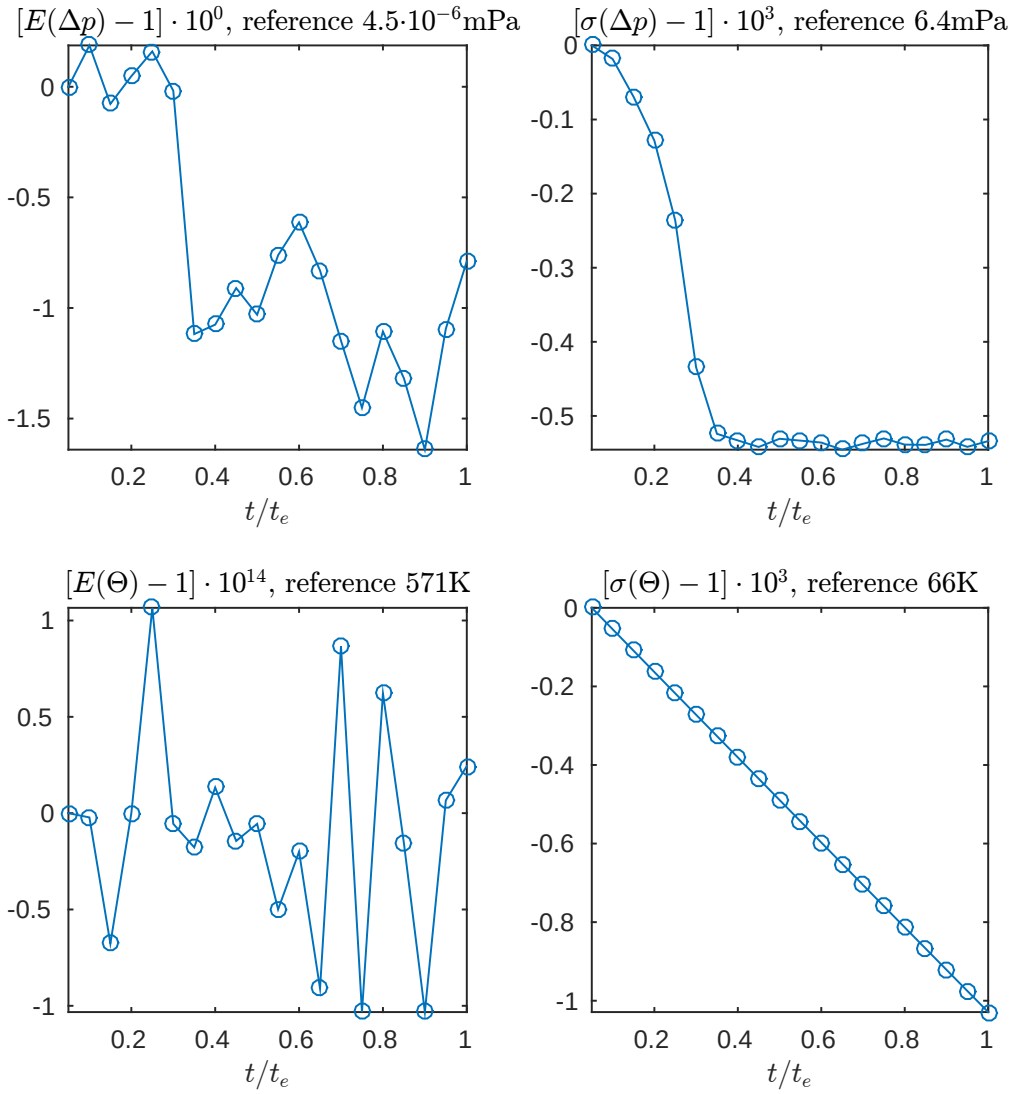

Fig. 3.5.: Normalized mean value (E) and standard deviation (σ) of pressure difference and potential temperature over time in units of one period t_e. The value for $t = 0$ is omitted to emphasize the less abrupt changes in the further course of the simulation. The denoted reference is the value for $t = t_e/20$ and the dimensionless deviation from it is shown on the vertical axis, i.e. the first point is zero by construction. Rescaling factors in orders of 10 emphasize the magnitude of the difference.

While the centerline $\mathbf{X}(z,t) = (\mathrm{X},\mathrm{Y})^\top$ is likewise characterized by a maximum of vorticity this averaged measure is better suited, also promising reliable results when the data is fluctuating. Typically the centerline will be located within the center of the domain reducing the influence of the boundary. The integrals are easily solved over a rectangular domain Σ with the trapezoidal rule, i.e. with $(M+1)\times(M+1)$ evenly spaced grid points for any integrand $s(x,y)$ we find

$$\int_\Sigma s(x,y)\,\mathrm{d}(x,y) = \frac{(\Delta x)^2}{4}\sum_{i=1}^{M}\sum_{j=1}^{M}\left(s_{i,j}+s_{i,j+1}+s_{i+1,j}+s_{i+1,j+1}\right) \tag{3.3.2d}$$

where the subscripts i and j stand for the evaluation at the grid point (x_i, y_j), i.e. $s_{i,j} := s(x_i, y_j)$.
If the density norm (3.3.2c) vanishes one can not specify a vortex core, a weakness when using this approach. However, the later object of interest features a non-zero Ω, justifying the primarily discussed averaging technique. We will just note here that many other dedicated approaches to this kind of problem exist, e.g. by determining the vortex core size (Schielicke *et al.*, 2016).

3.3.2. Circumferential velocity

3.3.2.1. Measure

Once we obtained the vortex centerline we are able to calculate further characteristic quantities of a vortex. A crucial one is the azimuthal velocity $u_\vartheta(r,z,t)$. Since numerical quantities are subject to local oscillations, we introduce an averaged definition at this point. A useful quantity in rotational flows is the circulation Γ_r along a closed circle $B_r(\mathbf{X})$ with radius r and center $\mathbf{X}$, embedded in the horizontal plane. For each level z and time t we have

$$\Gamma_r(z,t) = \oint_{\partial B_r(\mathbf{X})} \boldsymbol{u}\cdot\mathrm{d}\mathbf{L}, \tag{3.3.3a}$$

and remembering that the azimuthal velocity is given by $\boldsymbol{u}\cdot\boldsymbol{e}_\vartheta = u_\vartheta$ the line integral is

$$\Gamma_r(z,t) = \int_0^{2\pi} u_\vartheta(r,\vartheta,z,t)\; r\mathrm{d}\vartheta. \tag{3.3.3b}$$

Following Stokes' theorem the circulation (3.3.3a) is also determined by

$$\Gamma_r(z,t) = \int_{B_r(\mathbf{X})} \boldsymbol{\omega}\cdot\mathrm{d}\mathbf{S} \tag{3.3.4a}$$

and according to the integration path this integral becomes

$$\Gamma_r(z,t) = \int_{B_r(\mathbf{X})} \omega_3(\boldsymbol{x},t)\;\mathrm{d}S. \tag{3.3.4b}$$

For a radially symmetric velocity we find, equating both expressions for circulation (3.3.3b) and (3.3.4b):

$$2\pi r u_\vartheta(r,z,t) = \int_{B_r(\mathbf{X})} \omega_3(\boldsymbol{x},t)\;\mathrm{d}S. \tag{3.3.5}$$

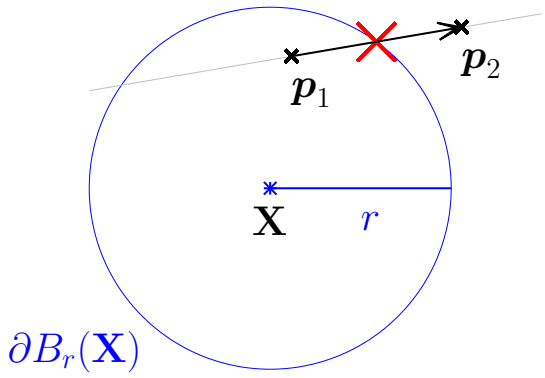

Fig. 3.6.: Sketch of intersecting line and circle at $\boldsymbol{p}$.

Solving the integral on the right hand side gives an averaged expression for $u_\vartheta(r, z, t)$ for each circle $B_r(\mathbf{X})$. The challenge is now to determine the area a circle occupies on a rectangular grid. For each cell of the grid a function is needed that returns the area of the circle section inside. After a brief outline of the task at hand we will present a method for numerical discretization.

3.3.2.2. Intersection of line and circle

The resolution dictates how many cells of the grid cover just a section of the circle $B_r(\mathbf{X})$, this portion of the cell is needed for an area calculation. We first look at a 1D problem.

Let $\boldsymbol{p}_1$ and $\boldsymbol{p}_2$ denote the position vectors of two distinct points where either of the points lies inside and the other outside of a circle with center $\mathbf{X}$ and radius r (figure 3.6). We aim to determine a function $\mathcal{I}(\boldsymbol{p}_1, \boldsymbol{p}_2)$ that determines the distance of $\boldsymbol{p}_1$ to the circle boundary pointing from $\boldsymbol{p}_1$ to $\boldsymbol{p}_2$. That is, we are searching for the point $\boldsymbol{p}$ that is both on the line between $\boldsymbol{p}_1$ and $\boldsymbol{p}_2$,

$$\boldsymbol{p} = \boldsymbol{p}_1 + \mathcal{I}\frac{\boldsymbol{p}_2 - \boldsymbol{p}_1}{|\boldsymbol{p}_2 - \boldsymbol{p}_1|} \tag{3.3.6a}$$

and on the boundary of the circle,

$$|\boldsymbol{p} - \mathbf{X}|^2 = r^2. \tag{3.3.6b}$$

Inserting (3.3.6a) in (3.3.6b) gives a quadratic equation for $\mathcal{I}$, and its two solutions are

$$\mathcal{I}_\pm = -\frac{(\boldsymbol{p}_1 - \mathbf{X}) \cdot (\boldsymbol{p}_2 - \boldsymbol{p}_1)}{|\boldsymbol{p}_2 - \boldsymbol{p}_1|} \pm \sqrt{\frac{|\boldsymbol{p}_1 - \mathbf{X}|^2 |\boldsymbol{p}_2 - \boldsymbol{p}_1|^2}{|\boldsymbol{p}_2 - \boldsymbol{p}_1|^2} - |\boldsymbol{p}_1 - \mathbf{X}|^2 + r^2}. \tag{3.3.7a}$$

Since this line intersects the circle twice, we assumed $\boldsymbol{p}_1$ and $\boldsymbol{p}_2$ to be on separate sides of the circle boundary, also two solutions for $\mathcal{I}$ exist. Considering that the function $\mathcal{I}(\boldsymbol{p}_1, \boldsymbol{p}_2)$ is designed to calculate the area of circle sections in a cell, we request that the distance lies between 0 and $|\boldsymbol{p}_2 - \boldsymbol{p}_1|$, i.e.

$$\mathcal{I}(\boldsymbol{p}_1, \boldsymbol{p}_2) = \begin{cases} \mathcal{I}_+ & \text{if} \quad 0 \leq \mathcal{I}_+ \leq |\boldsymbol{p}_2 - \boldsymbol{p}_1| \\ \mathcal{I}_- & \text{else} \end{cases} . \tag{3.3.7b}$$

3.3.2.3. Cut-cells

With the function $\mathcal{I}$ (3.3.7) at hand we can now approach the 2D problem, utilizing our function from 1D. There are five cases that we distinguish as pointed out in figure 3.7: $\boxed{0}$, $\boxed{1}$, $\boxed{2}$, $\boxed{3}$ and $\boxed{4}$ correspond to the number of cell vertices that lie inside the circle. By design $B_r(\mathbf{X})$ is constructed starting from a specific r of a grid point. Consequently there is no cell that covers the whole circle and at the same time has no vertex inside of it. If no cell vertices are inside the circle this means that the cell lies completely outside of it: the circle cannot be embedded in any cell without containing at least one vertex. As before we assume a horizontally uniform grid, i.e. with the same spacing in each horizontal direction. This assumption greatly simplifies the following considerations without restricting the generality. It is well suited for the applications that we will consider. In a next step, we will transform all cells in any of these five forms, and integration is the sum of each contribution.

3.3.2.4. Universal vertices

Regarding the possible cases in figure 3.7 we emphasize that the vertices r_1, r_2, r_3, r_4 denote the distance to the circle center $\mathbf{X}$ and that they are in ascending order. This is a result of the case design, differing by the number of vertices inside the circle.

In all, it motivates the following ansatz: for any cell vertex i positioned at $\boldsymbol{p}_i$ determine its distance to $\mathbf{X}$ and call it $\mathcal{R}_i = |\boldsymbol{p}_i - \mathbf{X}|$. Denote the integrand to be evaluated at $\mathcal{R}_i$ with $\mathcal{S}_i$. A bubble sort algorithm on $\mathcal{Q}_i = \{\boldsymbol{p}_i, \mathcal{R}_i, \mathcal{S}_i\}$ gives the desired order, i.e. in pseudocode:

```
do i=4,1,−1 ! for any cell vertex i
   do j=1,i−1
      if R_j > R_{j+1} then ! if not ordered ascendingly
         swap(Q_j, Q_{j+1}) ! swap position, radius and integrand
      endif
   enddo
enddo
```

Geometrically, this is equivalent to rotation and/or reflection of the cell, i.e. an isometric transformation. As a result, the vertices are in ascending distance from the circle center and any of the integration problems reduces to one of the five cases in figure 3.7. Lastly, we approximate the area in those circle sections.

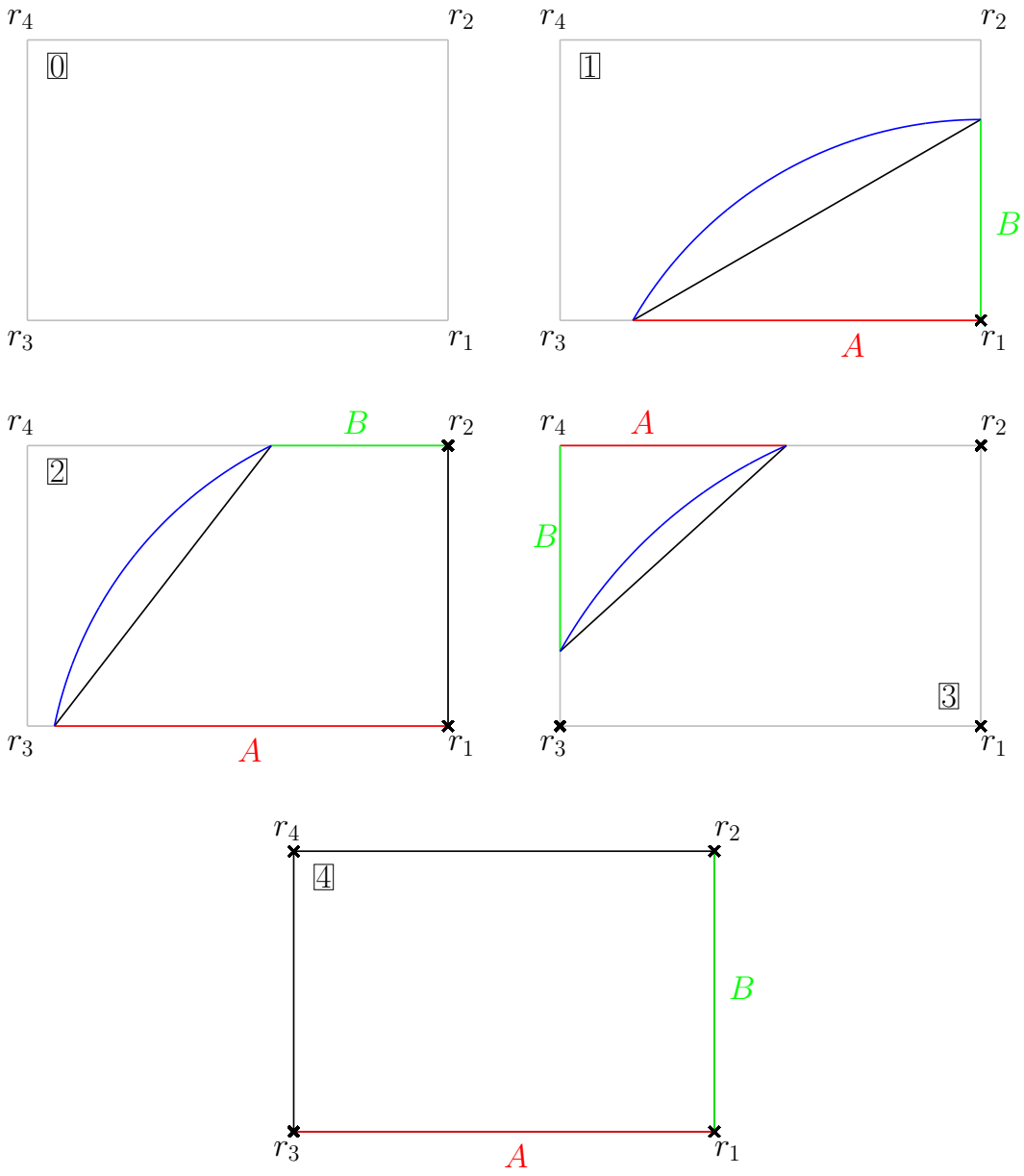

Fig. 3.7.: Sketch of different cases that arise when integrating a circle with boundary $\partial B_r(\mathbf{X})$ on a rectangular grid. The corners r_1, r_2, r_3, r_4 of each grid cell lie inside the circle if they are denoted with a cross ✕. The characteristic lengths A and B for each geometrical object are highlighted.

3.3.2.5. Quadrature

Let s_i denote the integrand evaluated at r_i and Δx be the spacing of the uniform 2D grid. For each of the geometric shapes in figure 3.7 we use a quadrature formula to calculate the integral, S, over the circle, i.e.

$$\boxed{0}: \quad \text{empty}, \qquad S = 0 \tag{3.3.8a}$$

$$\boxed{1}: \quad \text{triangle}, \qquad S = \frac{1}{2} AB s_1 \tag{3.3.8b}$$

$$\boxed{2}: \quad \text{trapezoidal}, \qquad S = \frac{\Delta x}{2} (A + B)\, \overline{s_{12}} \tag{3.3.8c}$$

$$\boxed{3}: \quad \text{square} - \text{triangle}, \qquad S = \left[(\Delta x)^2 - \frac{1}{2} AB \right] \overline{s_{123}} \tag{3.3.8d}$$

$$\boxed{4}: \quad \text{square}, \qquad S = (\Delta x)^2 \overline{s_{1234}} \tag{3.3.8e}$$

where the overlined s denote an average of the discretized integrand at the respective vertices, i.e.

$$\overline{s_{12}} := \frac{1}{2} (s_1 + s_2), \quad \overline{s_{123}} := \frac{1}{3} (s_1 + s_2 + s_3), \quad \overline{s_{1234}} := \frac{1}{4} (s_1 + s_2 + s_3 + s_4). \tag{3.3.8f}$$

3.3.2.6. Integration and interpolation

With the preceding ideas the integral in (3.3.5) can be approximated in n^2 steps on a grid with n^2 points. Regarding that the grid resolution is rather high and this needs to be done for each level and in each time step we aim to reduce the number of steps. We benefit from the design of the problem, a rather centrally positioned vortex core within the domain. Utilizing an interpolation method less steps are needed:
The function u_ϑ is determined along a horizontal line, e.g. $\vartheta = \pi/2$, for discrete radii $\overline{r}$ integrating along $B_{\overline{r}}(\mathbf{X})$ for each of them. Since the azimuthal velocity close to the boundary is not of greater interest we choose, without loss of generality, to move along the horizontal x-axis from $\mathbf{X}$ towards the boundary. In that way, we obtain in roughly $n/2$ steps a discrete function $u_\vartheta(\overline{r}, z, t)$ that we linearly interpolate to arrive at the circumferential velocity profile $u_\vartheta(r, z, t)$.

4. Vortices under environmental shear

In the preceding chapters we provided a basis for a numerical investigation of tropical cyclones (TC). In a next step we will introduce a model for such storms followed by a summary of some technical considerations that come with it, e.g. determining its center from the data. Concluding, we will discuss two differently sheared adiabatic vortices. We find that the initial tilt influences the further evolution of the centerline.

4.1. Model parameters

Our long-term goal is to numerically investigate the theory introduced by Paeschke *et al.* (2012) on baroclinic vortices under environmental shear, and we therefore choose the same characteristic parameters and rescaling, cf. table 4.1 and 4.2, representing typical values for a dry atmosphere at sea level in the subtropics.

The domain of interest will consist of a vortex embedded in a geostrophic background. In 2.3.1 we presented a possible rescaling of u_{ref} and t_{ref} to observe the influence of the Mach-number on the flow. Instead, using the geostrophic model 2.1.5 motivates a separation of vertical and horizontal dynamics. Also, in 2.2.3 we have seen that the vertical and horizontal wave propagation are dominated by Brunt-Väisälä or Coriolis frequency, respectively. If both contribute equally to the final internal wave frequency (2.2.15) a specific relationship between the length scales arises (Pedlosky, 1987). The horizontal scale l_b and vertical scale h_b correspond to the wave vector $\mathbf{a}_e = (2\pi/l_b, 2\pi/l_b, 2\pi/h_b)$ that needs to fulfill

$$f_0^2 \frac{(2\pi)^2}{h_b^2} = N_0^2 \frac{(2\pi)^2}{l_b^2}. \tag{4.1.1}$$

A typical vertical length scale was found during nondimensionalization: the pressure scale height h_{sc}, (2.3.3a). It denotes the height an air column would need to induce the reference pressure p_{ref}, assuming a constant ρ_{ref}, starting from where the reference values are measured, e.g. sea level. It will continue to serve as the vertical length scale. Let l_{syn} be the according horizontal length scale, it is determined by (4.1.1),

$$l_{\text{syn}} = \frac{N_0}{f_0} h_{\text{sc}}. \tag{4.1.2}$$

This is the *synoptic scale* specifically of interest when investigating TCs and their surroundings, in turn the vortex core size is much smaller and on the order of l_{mes}, the length scale of the *mesoscale*. The assumption of constant potential temperature stratification and a consequently constant $N \equiv N_0$ is made here as well. However, at this point the Coriolis parameter is described by the β-plane approximation giving rise to a meridional

dependence. This in turn gives rise to *Rossby waves* that appear for non-constant f. As a remark, the dispersion relation (2.2.15) states that the frequency of internal waves depends on the (constant) Coriolis parameter. While we required a constant $f = f_0$ to arrive at the linear system (2.2.14) the outcome would be the same for $f = f_0 + \beta y$ since the the equations (2.2.11) were linearized and a possible variation of f would be eliminated.

Despite the separate length scales we require a unique time scale t_{ref} for both horizontal and vertical displacements. Since environmental shear dominantly affects horizontal motions the time scale that we resolve is the one on the synoptic scale, i.e. $t_{\mathrm{ref}} = l_{\mathrm{syn}}/u_{\mathrm{ref}}$ (Paeschke *et al.*, 2012). Consequently, the velocities are related by

$$w_{\mathrm{ref}} = \frac{h_{\mathrm{sc}}}{l_{\mathrm{syn}}} u_{\mathrm{ref}}. \tag{4.1.3}$$

A useful quantity to describe vortical flows is the Rossby number

$$\mathrm{Ro} := \frac{u_{\mathrm{ref}}}{l_{\mathrm{syn}} f_0} = \left(\frac{l_{\mathrm{syn}}}{u_{\mathrm{ref}}}\right)^{-1} \frac{1}{f_0}. \tag{4.1.4}$$

It denotes the ratio of inertial and Coriolis force, or equivalently the ratio of the time scales for Earth's rotation and advection. Analogously, the vortex Rossby number is

$$\mathrm{Ro}_{\mathrm{mes}} = \frac{u_{\mathrm{mes}}}{f_0 l_{\mathrm{mes}}} \tag{4.1.5}$$

with a characteristic mesoscale velocity u_{mes}. It is a good measure for vortex strength: A high $\mathrm{Ro}_{\mathrm{mes}}$ stands for fast advection compared to the Coriolis effect. In a next step we observe the scaling of the horizontal velocity,

$$\frac{u_{\mathrm{ref}}}{h_{\mathrm{sc}}} \sim \left|\frac{\partial u^{\dagger}}{\partial z}\right|, \tag{4.1.6}$$

that itself will lead to the vertical velocity scale, cf. (4.1.3). The horizontal velocity scale is, starting from the geostrophic model (2.1.41), determined by the thermal wind relation (Klein, 2008, 2010):

$$\frac{\partial u^{\dagger}}{\partial z} \sim \frac{1}{f_0 \rho_{\mathrm{ref}}} \nabla_{\parallel} \frac{\partial p}{\partial z}. \tag{4.1.7}$$

Hydrostatic balance (2.1.40a) and the bouyancy frequency (2.2.10) lead to

$$u_{\mathrm{ref}} \sim h_{\mathrm{sc}} \tan\varphi_0 \frac{N^2}{f_0^2} \beta a \left(\frac{\mathrm{d}\Theta}{\mathrm{d}z}\right)^{-1} \nabla_{\parallel}\Theta \tag{4.1.8}$$

since $f_0 \sim a\beta \tan\varphi_0$. At last, we utilize the arc length from pole to equator and an according temperature difference $\Delta\Theta$, such that

$$\nabla_{\parallel}\Theta \sim \frac{\Delta\Theta}{\frac{\pi}{2}a} \tag{4.1.9}$$

Quantity	Variable	Value
Gravity acceleration	g	$9.81\,\mathrm{m\,s^{-2}}$
Latitude	φ	$30°$ N
Coriolis parameter	f_0	$7.3 \cdot 10^{-5}\mathrm{s^{-1}}$
Meridional variation	β	$2 \cdot 10^{-11}\mathrm{m^{-1}s^{-1}}$
Pressure	p_{ref}	$10^5\mathrm{Pa}$
Temperature	T_{ref}	$300\mathrm{K}$
Brunt-Väisälä frequency	N	$10^{-2}\mathrm{s^{-1}}$
Dry gas constant	R	$287\mathrm{m^2s^{-2}K^{-1}}$
Isentropic exponent	γ	1.4

Table 4.1.: Model parameters (Paeschke *et al.*, 2012)

Quantity	Variable	Estimated value
Density	$\rho_{\mathrm{ref}} = \dfrac{p_{\mathrm{ref}}}{RT_{\mathrm{ref}}}$	$1.16\ \mathrm{kg\,m^{-3}}$
Vertical distance	$h_{\mathrm{sc}} = \dfrac{p_{\mathrm{ref}}}{g\rho_{\mathrm{ref}}}$	$8.8\mathrm{km}$
Horizontal distance	$l_{\mathrm{syn}} = \dfrac{N}{f_0} h_{\mathrm{sc}}$	$1200\mathrm{km}$
Horizontal velocity	$u_{\mathrm{ref}} = h_{\mathrm{sc}}^2 \dfrac{\tan\varphi_0}{\pi/2} \dfrac{N^2}{f_0^2}\beta$	$10\mathrm{ms^{-1}}$
Time	$t_{\mathrm{ref}} = \dfrac{l_{\mathrm{syn}}}{u_{\mathrm{ref}}}$	$1.2 \cdot 10^5\mathrm{s}$
Vertical velocity	$w_{\mathrm{ref}} = \dfrac{h_{\mathrm{sc}}}{l_{\mathrm{syn}}} u_{\mathrm{ref}}$	$0.1\mathrm{ms^{-1}}$

Table 4.2.: Derived scales (Paeschke *et al.*, 2012)

and with $h_{\mathrm{sc}} \sim \Delta z$ we find for (4.1.8) a suitable velocity scale

$$u_{\mathrm{ref}} = h_{\mathrm{sc}}^2 \frac{\tan\varphi_0}{\pi/2} \frac{N^2}{f_0^2}\beta. \tag{4.1.10}$$

As a side note, the regime we consider has a Rossby number (4.1.4) of

$$\mathrm{Ro} = \frac{u_{\mathrm{ref}}}{f_0 l_{\mathrm{syn}}} \approx 0.11, \tag{4.1.11}$$

typical for the incipient stage of a hurricane (Shapiro & Montgomery, 1993). Table 4.2 summarizes the preceding considerations.

4.2. Initialization of a TC-like vortex

Our object of interest are hurricanes at an incipient stage, i.e. with vortex Rossby numbers of order 1. Recent studies (Reasor & Montgomery, 2001, Reasor *et al.*, 2004)

suggested a Gaussian profile for the vortex' vorticity distribution. In contrast to stronger TCs the vorticity is broadly distributed and exhibits a slower decay in the tangential wind (Shapiro & Montgomery, 1993, Willoughby, 1990). We construct a vorticity profile along the lines of Reasor & Montgomery (2001).

An atmospheric vortex is embedded in an initially geostrophic flow, cf. 2.1.5, its center is located at $\mathbf{X}(t)$ and the velocity profile is $\boldsymbol{U}(\boldsymbol{x},0) = (\boldsymbol{u}^\dagger, 0)^\top$. Cylindrical coordinates $(r,\vartheta,z)^\top$ with the orthonormal vectors $\boldsymbol{e}_r, \boldsymbol{e}_\vartheta$ and $\boldsymbol{k}$ are well-suited for this kind of problem, and for the horizontal velocity $\boldsymbol{u}^\dagger(r,\vartheta,z)$ we find the respective components

$$\begin{aligned} u_r^\dagger = \boldsymbol{u}^\dagger \cdot \boldsymbol{e}_r, \quad u_\vartheta^\dagger = \boldsymbol{u}^\dagger \cdot \boldsymbol{e}_\vartheta \quad \text{such that} \\ \boldsymbol{u}^\dagger = u_r^\dagger \boldsymbol{e}_r + u_\vartheta^\dagger \boldsymbol{e}_\vartheta. \end{aligned} \tag{4.2.1}$$

This is a 3D extension to (3.2.2). For the specific case of radial symmetry with $u_r^\dagger = 0$ and $u_\vartheta^\dagger(r,z)$ the differential equation for vorticity (2.1.42) becomes

$$q^\dagger(r,z) = \frac{1}{r}\frac{\partial}{\partial r}\left[r u_\vartheta^\dagger(r,z)\right] \tag{4.2.2}$$

utilizing the representation of ∇ in cylindrical coordinates. It has multiple solutions for $u_\vartheta^\dagger$, including discontinuous ones. Requiring the boundary condition $u_\vartheta^\dagger(0,z) = 0$ leads to a unique solution for $u_\vartheta^\dagger$, at the vortex center the azimuthal velocity is zero. We solve (4.2.2) integrating from the origin to a radius r':

$$\int_0^{r'} r q^\dagger(r,z)\mathrm{d}r = r'\, u_\vartheta^\dagger(r',z). \tag{4.2.3}$$

Therefore, the circumferential velocity is determined by

$$u_\vartheta^\dagger(r',z) = \frac{1}{r'}\int_0^{r'} r q^\dagger(r,z)\mathrm{d}r. \tag{4.2.4}$$

Prescribing the vorticity leads to a velocity profile that is utilized for initialization.

4.2.1. Characteristic parameters

For now we omit the dependence on the vertical coordinate, due to the symmetry expressed in (4.2.4) implementing it later on will be straightforward. Reasor & Montgomery (2001) suggested to model a TC by an axisymmetric potential vorticity

$$q^\dagger(r) = q_m^\dagger e^{-\sigma^2 r^2} \tag{4.2.5}$$

with the constant parameters $q_m^\dagger$ and σ. Their physical meaning becomes clear in the following derivation.

Considering the structure of tropical vortices their extent is often designated by the radius of maximum wind that we call L. With equation (4.2.4) we calculate the radius and corresponding vorticity:

$$\left.\frac{\partial u_\vartheta^\dagger}{\partial r'}\right|_L = 0, \quad \text{equivalently} \quad q^\dagger(L) - \frac{1}{L^2}\int_0^L r q^\dagger(r)\mathrm{d}r = 0. \tag{4.2.6a}$$

This gives with (4.2.2)

$$q^\dagger(L) = \frac{1}{L} u_\vartheta^\dagger(L). \tag{4.2.6b}$$

Now in the specific case of (4.2.5) the condition for maximum wind (4.2.6a) translates to

$$e^{-\sigma^2 L^2} = \frac{1 - e^{-\sigma^2 L^2}}{2\sigma^2 L^2}, \quad \text{or rewritten with } n := \sigma L \tag{4.2.7}$$

$$e^{n^2} = 1 + 2n^2. \tag{4.2.8}$$

To solve this equation we make use of the Lambert W function that is the solution to $s = W(s)\exp W(s)$, in our case $s \in \mathbb{R}$ and

$$-\frac{1}{2}\exp\left(-\frac{1}{2}\right) = \left(-\frac{1}{2} - n^2\right)\exp\left(-\frac{1}{2} - n^2\right), \quad s \geq -e^{-1} \tag{4.2.9a}$$

$$\text{and we have} \quad W\left(-\frac{1}{2}e^{-1/2}\right) = -\frac{1}{2} - n^2, \tag{4.2.9b}$$

such that the solution is

$$n = \sqrt{-W\left(-\frac{1}{2}e^{-1/2}\right) - \frac{1}{2}}. \tag{4.2.10}$$

The Lambert W function exhibits two branches in the interval $(-e^{-1}, 0)$, so we have to consider both as a solution to our equation (4.2.8). However, considering the principal branch leads to the trivial solution $n = 0$, i.e. a spatially constant potential vorticity and linearly increasing velocity, no radius of maximum wind can be defined. Thus we accept the value of the $-1th$ branch as a solution that corresponds to

$$\sigma L \approx 1.12. \tag{4.2.11a}$$

In a second step we determine $q_m^\dagger$ by (4.2.6b):

$$q_m^\dagger = e^{\sigma^2 L^2} \frac{u_\vartheta^\dagger(L)}{L}. \tag{4.2.11b}$$

Concluding, with (4.2.11) the parameters $q_m^\dagger$ and σ are determined by the radius of maximum wind L and the maximum wind speed $u_\vartheta^\dagger(L)$.

4.2.2. Wind profile

Reminding the underlying model parameters 4.1 the maximum wind speed $u_\vartheta^\dagger(L)$ will be on the order of u_{ref} in the model, i.e. roughly 10ms^{-1}. With regards to the synoptic scale and the incipient stage of the TC a reasonable choice of the radius of maximum wind is 100km. With $u_r^\dagger = 0$, $u_\vartheta^\dagger(r)$ in (4.2.4) and (4.2.5) the initial velocity profile is

$$\begin{aligned} \boldsymbol{u}^\dagger(x,y) =& q_m^\dagger \frac{1 - e^{-\sigma^2 r^2}}{2\sigma^2 r} \begin{pmatrix} -\sin\vartheta \\ \cos\vartheta \end{pmatrix} \\ & \text{where } r = \sqrt{x^2 + y^2} \text{ and } \vartheta = \operatorname{atan2}(y, x) \end{aligned} \tag{4.2.12}$$

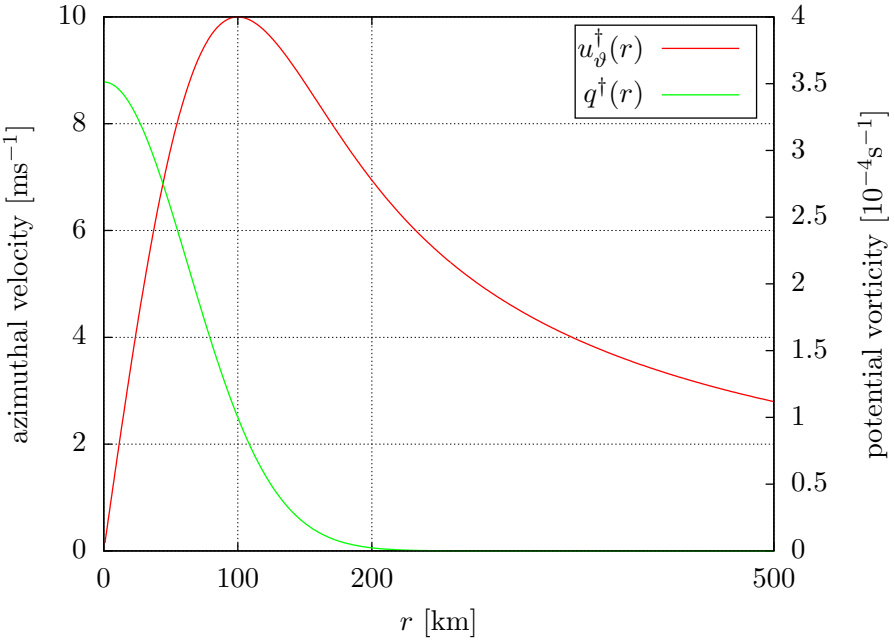

Fig. 4.1.: Characteristic profile for a TC determined by $L = 100\text{km}$ and $u_\vartheta^\dagger(L) = 10\text{ms}^{-1}$.

Figure 4.1 shows vorticity and circumferential velocity for $L = 100\text{km}$ and $u_\vartheta^\dagger(L) = 10\text{ms}^{-1}$. The center of the vortex at $r = 0$ with maximum vorticity and zero velocity is also called the *eye* of the storm. Further, the neighborhood of the strongest winds surrounding $r = L$ is referred to as the eye wall region.

The vortex is initially placed in the middle of a box that is $H = 10\text{km}$ high (compare with h_{sc}) and has a square base of $4000\text{km}\times4000\text{km}$, representing a part of the Earth's atmosphere. In order to model an atmospheric vortex on a finite domain we need to discuss the boundary conditions. We have seen that the velocity only slowly decays, but to retain a vanishing circulation at the boundary we need the velocity to approach zero. To obtain a concentrated vortex we define the lower and upper limit

$$r_0 = 1000\text{km}, \quad r_\infty = 1750\text{km} \tag{4.2.13}$$

and introduce the mollifier

$$m(r) = \cos^2\left(\frac{\pi}{2}\frac{r - r_0}{r_\infty - r_0}\right) \quad \text{for } r \in [r_0, r_\infty]. \tag{4.2.14}$$

In the interval $[r_0, r_\infty]$ this is a smooth reduction, and the final form of the initial velocity profile is

$$\boldsymbol{u}_\parallel^\dagger(x,y) = \begin{cases} \boldsymbol{u}^\dagger(x,y) & \text{if } r < r_0 \\ m(r)\cdot\boldsymbol{u}^\dagger(x,y) & \text{if } r_0 \le r \le r_\infty \\ 0 & \text{else} \end{cases} \tag{4.2.15}$$

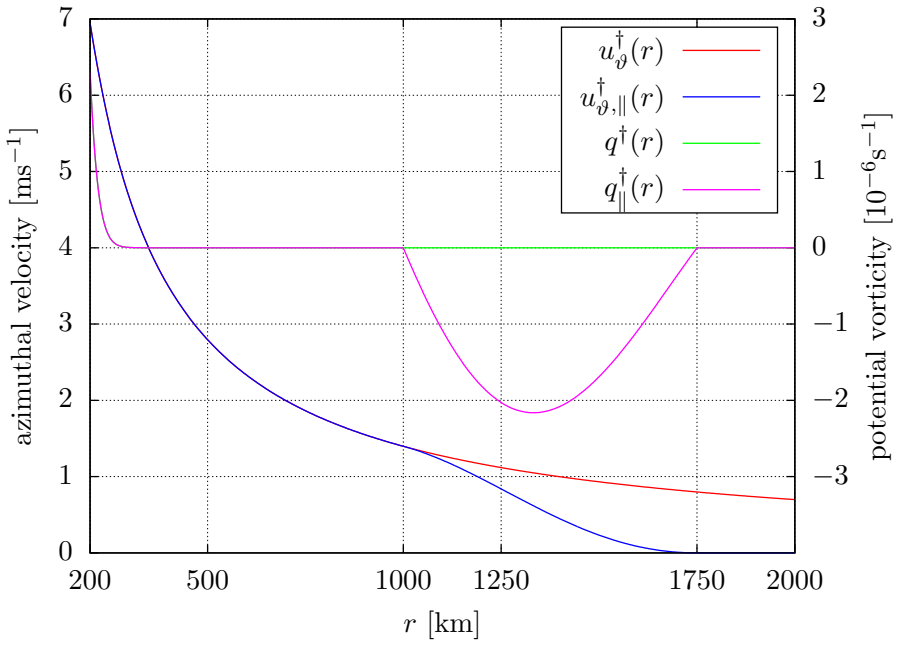

Fig. 4.2.: Same as in figure 4.1, but considering the decay of velocity. Velocity and vorticity profiles are identical with 4.1 for $r \in [0, r_0]$. Note the different unit for potential vorticity.

demonstrated in figure 4.2. These bounds are reasonable since the undisturbed vortex stretches over twice the synoptic scale, and there is enough room towards the boundary for a slow decay of velocity. Accordingly, the vertical vorticity is

$$q^\dagger_\parallel(r) = \begin{cases} q^\dagger(r) & \text{if } r < r_0 \\ m(r) \cdot q^\dagger(r) + m'(r) \cdot u^\dagger_\vartheta(r) & \text{if } r_0 \leq r \leq r_\infty \\ 0 & \text{else} \end{cases} \tag{4.2.16}$$

In accordance with the considerations on total circulation in 3.3.2.1 we also find for this profile

$$\int_0^{r_\infty} r q^\dagger_\parallel(r) \mathrm{d}r = 0, \tag{4.2.17}$$

at this point circulation and $u^\dagger_{\vartheta,\parallel}(r_\infty)$ vanish (3.3.5).

The quasi-geostrophic model also well describes the outer synoptic-scale flow for more general setups, however we do not consider non-zero far-field flow in this work.

4.2.3. Vertical distribution of the horizontal vortex displacement

Picking up the vertical degree of freedom we will discuss two different setups. The variational profile has an amplitude A and is smooth regarding its application in atmospheric

flows, e.g. $\alpha(z)$ is equal to

$$\alpha_c(z) = A\cos\left(\pi\frac{z}{H}\right) \quad \text{or} \tag{4.2.18a}$$

$$\alpha_l(z) = A\left(2\frac{z}{H} - 1\right), \tag{4.2.18b}$$

where H denotes the height of the domain. The initial position of the vortex center $\mathbf{X}(z,0)$ is complemented with a vertical variation, e.g.

$$\mathbf{X}(z,0) = \alpha(z)\,(\boldsymbol{i} + \boldsymbol{j}) \tag{4.2.19}$$

displacing the vortex centerline. If $\alpha(z)$ is different from zero the vortex will be displaced horizontally, but its structure is unchanged. Our goal is to observe the evolution in time, and further the role the different profiles play. This type of experiment is referred to as free-alignment of the vortex, Reasor & Montgomery (2001) discussed the linear case. We set the amplitude $A = 80$km or even $A = 160$km which is on the order of the radius of maximum wind indicating a rather strongly tilted vortex.
The displaced centerline at initialization could physically be the result of an imposed shear flow.

4.3. Implementation

Following the general framework introduced in the preceding sections the numerical implementation of this problem is the next step to take. We have seen in 3.2 that the pseudo-incompressible model in EULAG is well suited for vortical flows. The background state with $\overline{\Theta}(z)$ and $\overline{\rho}(z)$ is initialized appropriately, as described in 3.1.4. Specifically, a stably stratified fluid is the basis, suppressing mean variations of vertical velocity, and the stability parameter (3.1.7) is

$$s = \frac{N^2}{g} \tag{4.3.1}$$

with a constant bouyancy frequency N. The model parameters from table 4.1 are inserted, and the 4000km $\times$ 4000km $\times$ 10km domain is considered on a grid with $208 \times 208 \times 20$ points. In the vertical direction the boundaries are impermeable, consistently with the properties of the troposphere: It is bound by the tropopause on top, a layer of constant potential temperature below the stably stratified stratosphere. Due to the temperature inversion incoming waves are reflected and refracted, the tropopause strongly diminishes internal waves. The chosen time step is $\Delta t = 300$s, leading to an initial maximum Courant number of $C \approx 0.3$. Due to the problem setup the Courant number is very sensitive to vertical velocity, since the vertical spacing is much smaller than the horizontal one. Therefore, we might need to adjust the vortex configuration to fit in the same numerical model, e.g. the amplitude of displacement.

4.3.1. Infinite domain

As explained in 4.2.2 the vortex should not be influenced by boundary effects. Therefore, we need to imitate an infinite domain. Besides the prescribed zero velocity at the

horizontal boundaries we suppress their interaction with the inner domain using an absorber. The previous calculations for gravity waves provide a range of time scale t_R and thickness λ_R of the absorber. Following Klemp & Lilly (1978) we decide for a much bigger absorber with $t_R = 1500$s and $\lambda_R = 750$km at the horizontal boundaries.

4.3.2. Resolving the vortex core

In order to determine the circumferential velocity but also for technical reasons that will become clear when discussing diabatic vortices we need to extract the centerline $\mathbf{X}(z,t)$ from the data, its tilt $\frac{\partial \mathbf{X}(z,t)}{\partial z}$ is then calculated with central differences. Boundary effects strongly influence the determination of the vortex center that is initially placed in the middle of the domain, and we consider horizontally only the innermost 10% of the domain for the calculation. This subset is a reasonable restriction regarding the initial displacement, not exceeding 160km for each point on the centerline, and the narrow distribution of vorticity in figure 4.2 within this area: it is strictly positive and above 200km already down more than 99% of its maximum value. For vortices that experience a stronger tilt this might lead to errors, we will keep this in mind and return to the question later. Then, with $\Sigma = [-200\text{km}, 200\text{km}]^2$ the method presented in 3.3.1, equation (3.3.2), gives the centerline, and the tilt is calculated with central differences. Since our initial vorticity is positive on Σ and the negative values are significantly far away from $\partial\Sigma$, cf. figure 4.2, we expect $\Omega(z,t)$ to be non-vanishing also in the later course of the simulation. Subsequently, the azimuthal velocity is calculated as described in 3.3.2 (3.3.5), utilizing the vorticity routine implemented already in EULAG.

4.4. Aligning vortex

Similar to the setup investigated by Reasor *et al.* (2004) we initially displace the vortex centerline as directed in (4.2.19) and observe the aligning process. Due to the rotation a stretched centerline leads to precession, but also the centerline itself might be subject to change. The influence of the different profiles in (4.2.18) will be analyzed, we choose $A = 80$km. Figure 4.3 shows the initial vortex centerline. Note that the displacement is exactly opposite due to the different sign of the linear and the cosine function, $\operatorname{sgn} \alpha_l = -\operatorname{sgn} \alpha_c$. Since the setup is symmetric this has no influence on our findings.

In the further course of time the vortex precesses and the centerline rotates. Figure 4.4 shows it after three days. The synoptic time scale on which we expect to observe changes is roughly 1.4 days, requiring the simulations to cover at least several days.
While the initially cosine shaped centerline was not deformed or stretched, in the linear case after just a few time steps we get a cosine profile. With increasing time the α_c profile remains unchanged up to minor deviations, but the centerline of the initial α_l profile exhibits visible fluctuations. This is highlighted in the x-y plane in figure 4.4.

Further, we observe in all simulations that maximum wind speed and displacement are reduced within the first time steps, a small mismatch of the initial parameters could lead to this. The subsequent case runs also exhibit this decrease in the beginning.

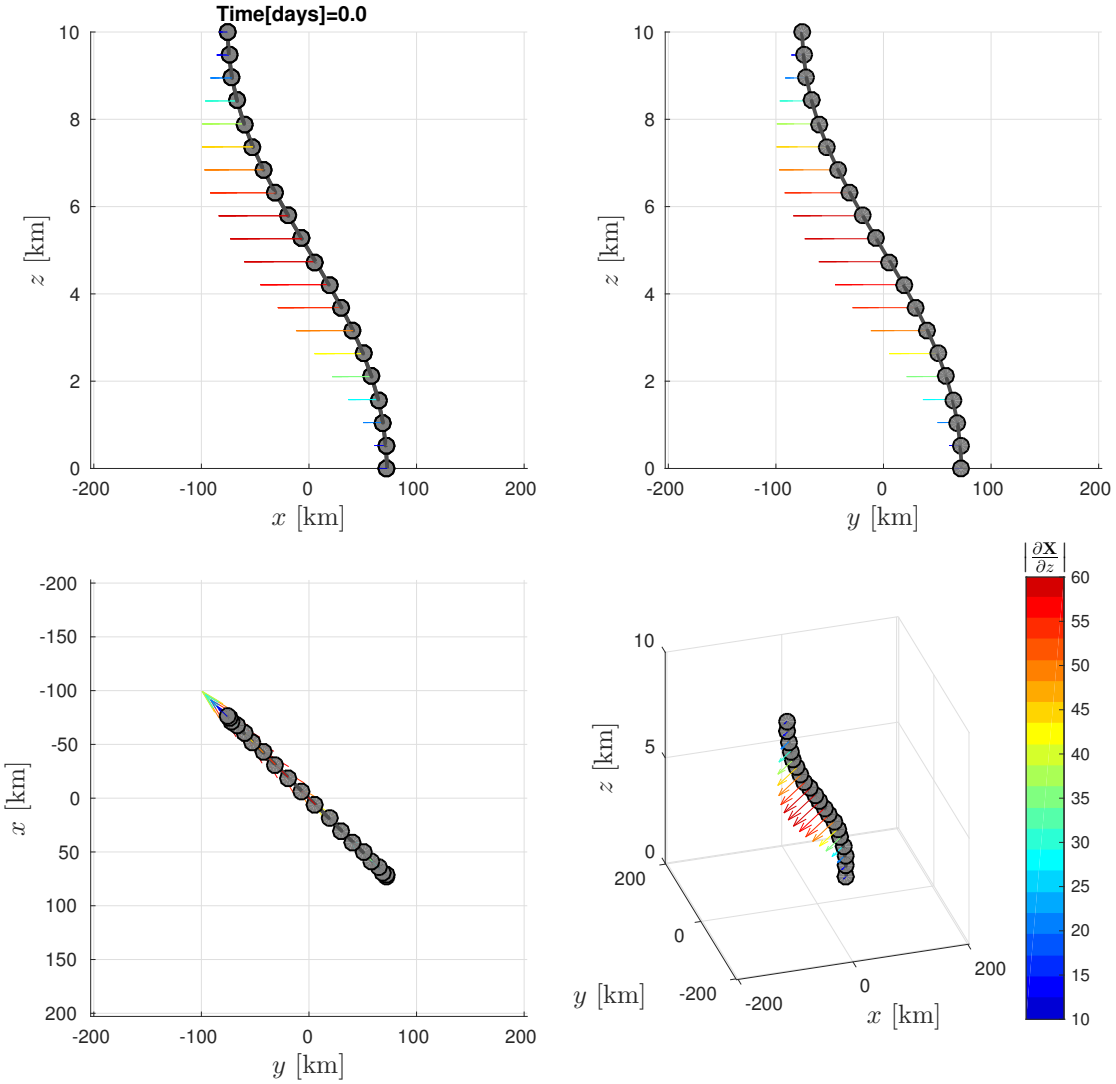

Fig. 4.3a.: Initial vortex centerline with $A = 80$km and the cosine profile $\alpha_c(z)$. Each discrete point of the centerline is complemented with a colored vector denoting the strength (colorscale, absolute value) and direction of the tilt.

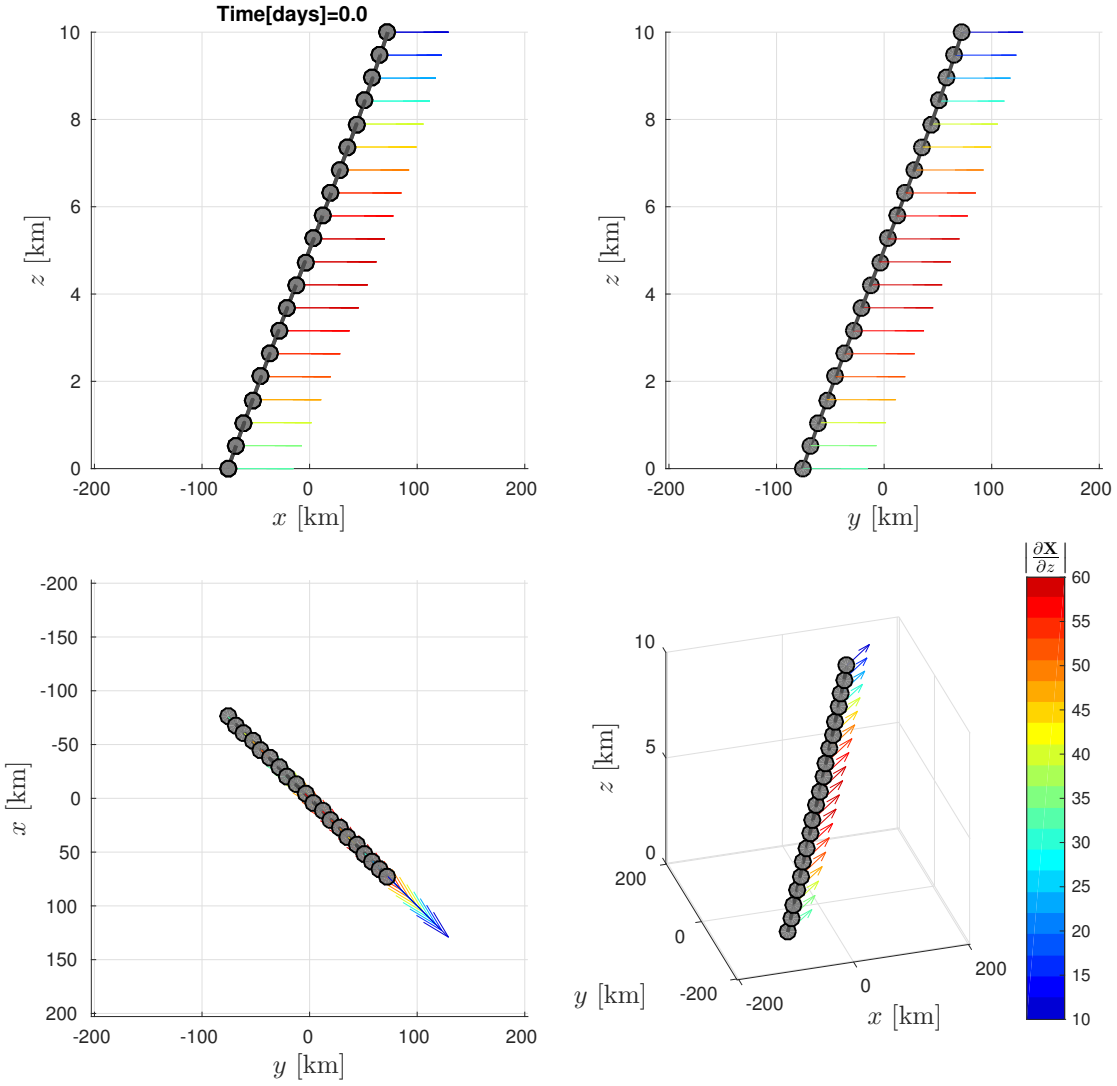

Fig. 4.3b.: As in figure 4.3a but for the linear profile $\alpha_l(z)$.

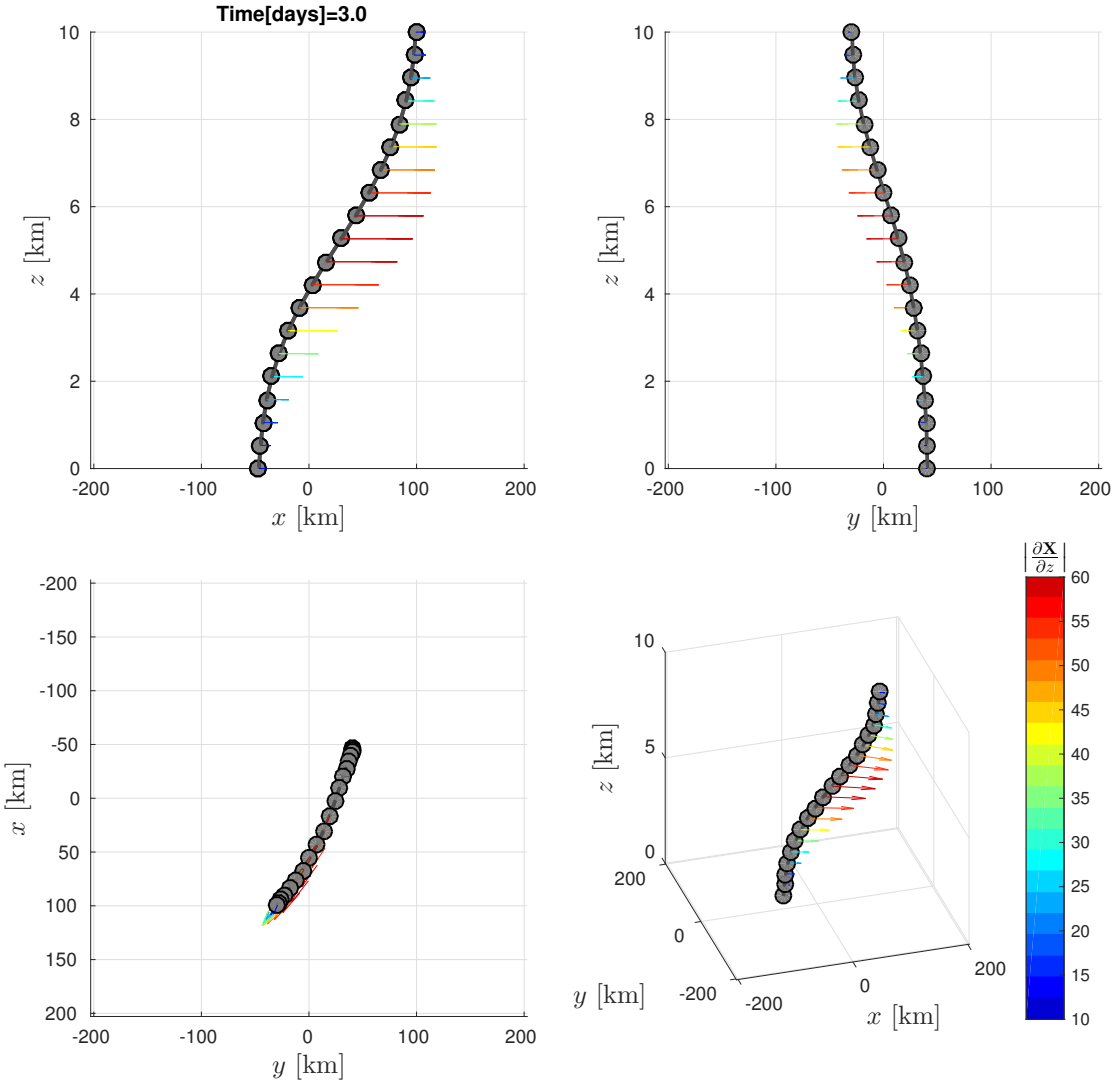

Fig. 4.4a.: Setup as in figure 4.3a (page 60) but after three days. The cosine profile has not changed significantly.

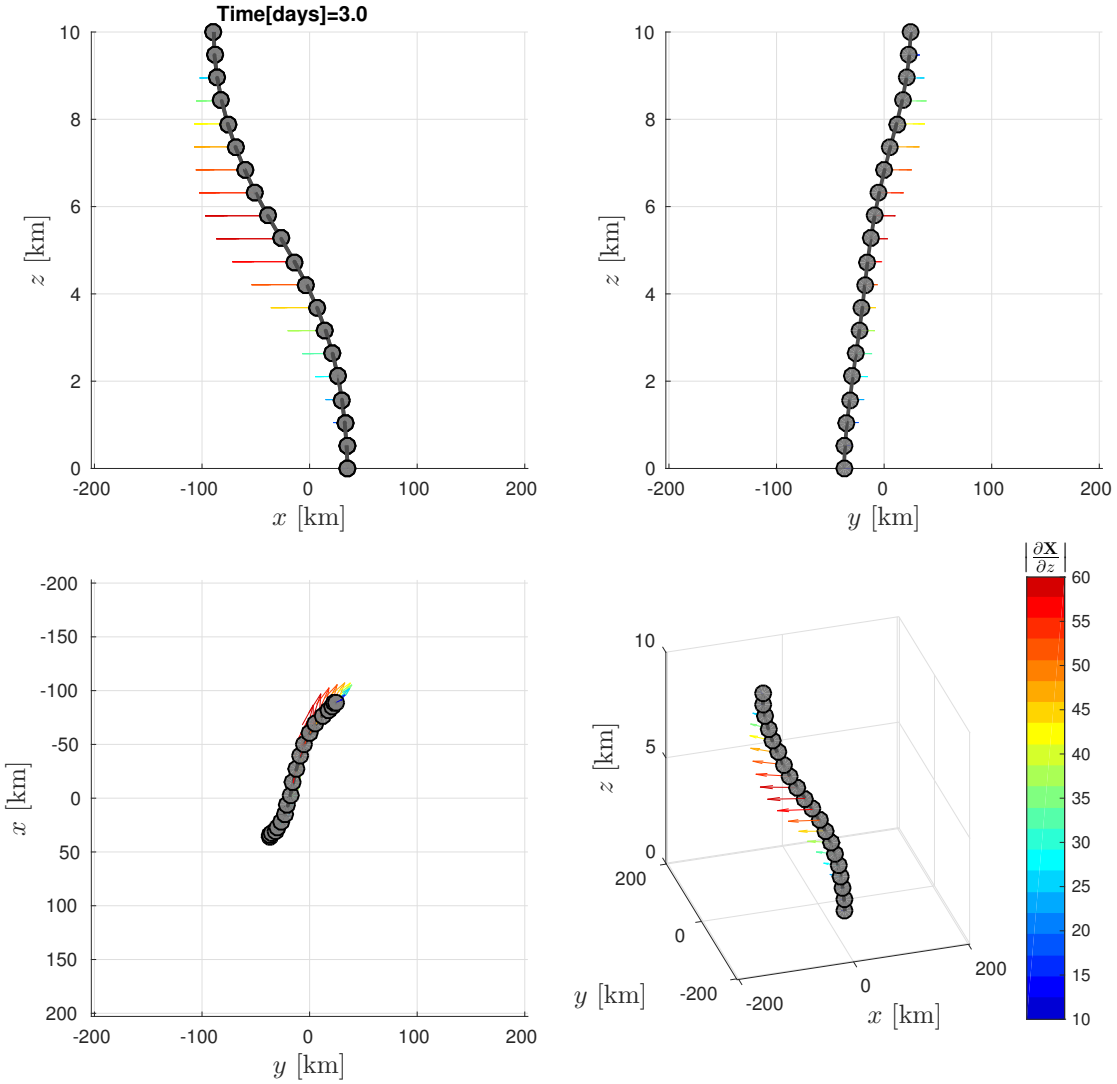

Fig. 4.4b.: As in figure 4.3b (page 61) but for the initially linear profile. The centerline has now assumed a cosine shape. A significant deviation to an initially straight line is observed in the x-y plane.

The preceding behavior in the numerical simulations can be explained with the findings of Paeschke *et al.* (2012): The cosine profile (4.2.18a) is one solution of the centerline evolution equation, the gravest Eigenmode. Generally, the solution consists of a series of Eigenmodes, however we suspect that numerical dissipation filters faster oscillating modes. Consequently, under certain preconditions the centerline of a vortex subject to displacement will converge to the cosine function. Although the imposed background state in this case does not lead to a constant-coefficient differential equation we observe a similar behavior for the gravest mode: The linearly displaced centerline takes on a cosine shape while the initial cosine profile only changes little. Since the solution to the centerline equation depends continuously on the coefficients we expect that almost constant coefficients depict the same principals. The crucial difference lies in the density (3.1.7b) that is not only an exponential function. However, the product of stability parameter and height does not exceed 0.1 and to first order

$$\frac{\mathrm{d}\overline{\rho}}{\mathrm{d}z} \sim \overline{\rho}. \tag{4.4.1}$$

In that case the coefficients in the centerline equation are constant. A Fourier ansatz in the Boussinesq case with $\overline{\rho} \equiv \overline{\rho}_0$ is presented and leads to a cosine shaped centerline. We therefore expect any displacement to follow this tendency, as demonstrated in figures 4.3 and 4.4. Therefore, the deviations for α_c are smaller than the ones for α_l since the former operates closer to the gravest Eigenmode. Fluctuations can still occur due to a non-exact fit or numerical dissipation.

Consequently, the following investigation only consists of the initial cosine profile. We conclude the discussion of the adiabatic vortex at this point, this and future simulations consider the case $A = 160\mathrm{km}$ for α_c if not stated otherwise.

5. Diabatic effects

The preceding analysis focused on adiabatic vortices neglecting the influence of heating that is generally covered by a source term Q_Θ in (2.1.14c). In their paper Paeschke *et al.* (2012) investigate the influence of asymmetric Q_Θ on TC tilt and core structure, giving rise to vortex attenuation or weakening in certain cases. Our numerical approach focuses on those two specific implications and aims to support their hypothesis. For that we need an extension to the previous chapter, complementing it with a spatially varying heating in each time step.

To start with we will outline the theoretical predictions from Paeschke *et al.* (2012), followed by a few details on the implementation and numerical caveats. Subsequently, three different regimes are observed. Conditions for vortex conservation, attenuation or amplification are tested against the numerical model. Additionally, a narrow heat source and the connection between tilt and centerline evolution are reassessed.

5.1. Model prediction

In this part we shortly describe the proposed model equations. According to the scaling presented in table 4.2 we introduce the nondimensional quantities

$$\overset{\star}{p} = \frac{p}{p_{\mathrm{ref}}}, \quad \overset{\star}{\rho} = \frac{\rho}{\rho_{\mathrm{ref}}}, \quad \overset{\star}{\Theta} = \frac{\Theta}{T_{\mathrm{ref}}}, \quad \overset{\star}{\boldsymbol{x}} = \frac{\boldsymbol{x}}{c_1 l_{\mathrm{syn}}}, \quad \overset{\star}{z} = \frac{z}{h_{\mathrm{sc}}}, \tag{5.1.1a}$$

$$\overset{\star}{\boldsymbol{u}} = \frac{\boldsymbol{u}}{u_{\mathrm{ref}}}, \quad \overset{\star}{t} = \frac{t u_{\mathrm{ref}}}{c_1 l_{\mathrm{syn}}}, \quad \overset{\star}{w} = \frac{w}{u_{\mathrm{ref}}} \frac{c_1 l_{\mathrm{syn}}}{h_{\mathrm{sc}}}, \quad \overset{\star}{\beta} = \frac{\beta l_{\mathrm{syn}}}{f_0}. \tag{5.1.1b}$$

Compared to the system in section 2.3.1 we require that the horizontal distance is of order l_{syn} and the velocity scale is u_{ref}, the constant c_1 will be determined later.
To start with, we utilize the scaling introduced in 4.1 and highlight the following nondimensional quantities:

$$(2.3.3\mathrm{c}): \quad \mathrm{M} = \frac{u_{\mathrm{ref}}}{c_{\mathrm{ref}}}, \qquad (4.1.4): \quad \mathrm{Ro} = \frac{u_{\mathrm{ref}}}{l_{\mathrm{syn}} f_0}, \tag{5.1.2a}$$

$$(2.3.3\mathrm{d}): \quad \mathrm{Da} = \frac{t_{\mathrm{ref}}}{T_{\mathrm{ref}}} Q_{\Theta,\mathrm{ref}}, \qquad \mathrm{Fr} = \frac{u_{\mathrm{ref}}}{N h_{\mathrm{sc}}} \tag{5.1.2b}$$

where the latter, the Froude number, denotes the ratio of flow and internal wave velocity. It becomes clear with the scaling of the Brunt-Väisälä frequency,

$$N^2 \sim \frac{g}{T_{\mathrm{ref}}} \frac{\Delta\Theta}{h_{\mathrm{sc}}}. \tag{5.1.3}$$

Then, the potential temperature can be rewritten utilizing the connection between vertical derivative and N,

$$\overset{\star}{\Theta} = 1 + c_2 \frac{\Delta\Theta}{T_{\mathrm{ref}}} \left(\overset{\star}{\Theta}_1(\overset{\star}{z}) + \tilde{\Theta} \right) \tag{5.1.4}$$

with $c_2 = \mathcal{O}(1)$. For thermal wind, internal and sound waves there are three different velocity scales, i.e.

$$u_{\mathrm{ref}} = h_{\mathrm{sc}}^2 \frac{\tan\varphi_0}{\pi/2} \frac{N^2}{f_0^2}, \qquad c_{\mathrm{int}} = N h_{\mathrm{sc}}, \qquad c_{\mathrm{ref}} = \sqrt{\frac{p_{\mathrm{ref}}}{\rho_{\mathrm{ref}}}}. \tag{5.1.5}$$

A distinguished asymptotic limit is set by (Klein, 2010)

$$\frac{c_{\mathrm{int}}}{c_{\mathrm{ref}}} \sim 1/3 \sim \sqrt{\varepsilon}, \quad \frac{u_{\mathrm{ref}}}{c_{\mathrm{int}}} \sim 1/9 \sim \varepsilon, \quad \frac{u_{\mathrm{ref}}}{c_{\mathrm{ref}}} \sim \varepsilon^{3/2} \tag{5.1.6}$$

leading to the scaling

$$\mathrm{M} = \varepsilon^{3/2}, \quad c_2 \frac{\Delta\Theta}{T_{\mathrm{ref}}} = c_2 \frac{\mathrm{M}^2}{\mathrm{Fr}^2} = \varepsilon, \quad \mathrm{Ro} = \frac{\varepsilon}{\widehat{f}_0}, \quad \overset{\star}{\beta} = \widehat{\beta}\varepsilon, \quad c_1 \frac{l_{\mathrm{syn}}}{h_{\mathrm{sc}}} = \frac{1}{\varepsilon^2} \tag{5.1.7a}$$

with $(\widehat{f}_0, \widehat{\beta}) = \mathcal{O}(1)$ as $\varepsilon \to 0$. Consequently, with c_1 set by the limit we find for those nondimensional quantities from (5.1.1)

$$\overset{\star}{\boldsymbol{x}} = \frac{\boldsymbol{x}}{h_{\mathrm{sc}}}\varepsilon^2, \quad \overset{\star}{t} = \frac{t u_{\mathrm{ref}}}{h_{\mathrm{sc}}}\varepsilon^2, \quad \overset{\star}{w} = \frac{w}{u_{\mathrm{ref}}}\frac{1}{\varepsilon^2}. \tag{5.1.8a}$$

While a vortex is embedded in an environment with a typical scale of l_{syn} its typical core size is much smaller and on the order of l_{mes}. There the gradient wind balance is a well-suited model with a vortex Rossby number of order unity due to the balance of pressure gradient, centrifugal and Coriolis terms: $\mathrm{Ro}_{\mathrm{mes}} = u_{\mathrm{mes}}/f_0 l_{\mathrm{mes}} = \mathcal{O}(1)$. Combined with the conservation of circulation $\Gamma = \mathcal{O}(2\pi l_{\mathrm{syn}} u_{\mathrm{ref}})$ and $\mathrm{Ro} = \mathcal{O}(\varepsilon)$ we recover the mesoscale $l_{\mathrm{mes}} = \mathcal{O}(\sqrt{\varepsilon} l_{\mathrm{syn}})$ where the vortex core structure is resolved. Paeschke *et al.* (2012) explain that in both inner and outer flow region the relevant changes happen on the synoptic time scale t_{ref}, reasoned by observed changes in the TCs strength, i.e. $t_{\mathrm{ref}} = l_{\mathrm{syn}}/u_{\mathrm{ref}}$ remains. Due to the factor $\sqrt{\varepsilon}$ that separates the synoptic and the vortex core scale we define

$$\delta := \sqrt{\varepsilon}, \tag{5.1.9}$$

this parameter is utilized for an asymptotic expansion. Following these considerations,

$$\delta \equiv \sqrt{\mathrm{Ro}} \tag{5.1.10}$$

is a valid choice for our numerical approach. The problem setup justifies the use of cylindrical coordinates, and the horizontal coordinates are split in the vortex centerline position $\overset{\star}{\mathbf{X}}$ and the vortex core scale $\tilde{\boldsymbol{x}}$,

$$\overset{\star}{\boldsymbol{x}} = \overset{\star}{\mathbf{X}}(\overset{\star}{t}, \overset{\star}{z}) + \delta\tilde{\boldsymbol{x}} = \overset{\star}{\mathbf{X}}_0(\overset{\star}{t}) + \delta \left(\overset{\star}{\mathbf{X}}^{(1)}(\overset{\star}{t}, \overset{\star}{z}) + \tilde{\boldsymbol{x}} \right) \tag{5.1.11a}$$

since $l_{\mathrm{mes}} = \mathcal{O}(\delta l_{\mathrm{syn}})$. The centerline is separated in a spatially constant part $\overset{\star}{\mathbf{X}}_0$ and the vortex tilt $\overset{\star}{\mathbf{X}}^{(1)}$. Upper indices "$(i)$" highlight the ith order of the term resulting from asymptotic expansion of the respective variable. We focus on the following scheme given by Paeschke *et al.* (2012), imposing a small heating term:

$$\overset{\star}{\Theta} = 1 + \delta^2 \overset{\star}{\Theta}_1 + \mathcal{O}(\delta^4) \tag{5.1.11b}$$

$$\overset{\star}{w} = \widetilde{w}^{(1)} + \mathcal{O}(\delta) \tag{5.1.11c}$$

$$\overset{\star}{u}_\vartheta(\overset{\star}{t}, \overset{\star}{\boldsymbol{x}}, z; \delta) = \delta^{-1} \overset{\star}{u}{}^{(0)}_\vartheta(\overset{\star}{t}, \tilde{r}, \overset{\star}{z}) + \mathcal{O}(1) \tag{5.1.11d}$$

$$\frac{\mathrm{Da}}{\delta^2} \overset{\star}{Q}_\Theta = \delta^2 \overset{\star}{Q}{}^{(2)}_\Theta + \mathcal{O}(\delta^5). \tag{5.1.11e}$$

Consequently, the data is to leading order related to this scaling via

$$\tilde{r} = \frac{\delta^3}{h_{\mathrm{sc}}} r, \qquad \overset{\star}{u}{}^{(0)}_\vartheta = \frac{\delta}{u_{\mathrm{ref}}} u_\vartheta \tag{5.1.12a}$$

$$\frac{\partial \overset{\star}{X}{}^{(1)}_k}{\partial \overset{\star}{z}} = \delta^3 \frac{\partial X_k}{\partial z}, \qquad \overset{\star}{Q}{}^{(2)}_\Theta = \frac{l_{\mathrm{syn}}}{\delta^4 T_{\mathrm{ref}} u_{\mathrm{ref}}} Q_\Theta \tag{5.1.12b}$$

$$\widetilde{w}^{(1)} = \frac{t_{\mathrm{ref}}}{h_{\mathrm{sc}}} w, \qquad \overset{\star}{\Theta}{}'_1 = \frac{1}{\delta^2} \frac{h_{\mathrm{sc}}}{T_{\mathrm{ref}}} \frac{\partial \Theta}{\partial z} \tag{5.1.12c}$$

where $\overset{\star}{\Theta}{}'_1 = \mathrm{d}\overset{\star}{\Theta}_1 / \mathrm{d}\overset{\star}{z}$ and $\tilde{r} = \overset{\star}{r}/\delta$. The Fourier expansion of functions F of ϑ is

$$F(\vartheta) = F_0 + \sum_n \left(F_{n1} \sin(n\vartheta) + F_{n2} \cos(n\vartheta) \right) \tag{5.1.13}$$

and applied to both vertical velocity and heating, indicated by the lower indices. For this specific setup of sufficiently weak heating we find the *core structure evolution equation*:

$$\frac{\partial \overset{\star}{u}{}^{(0)}_\vartheta}{\partial \overset{\star}{t}} + \widetilde{w}^{(1)}_0 \frac{\partial \overset{\star}{u}{}^{(0)}_\vartheta}{\partial \overset{\star}{z}} + \overset{\star}{u}{}^{(2)}_{r,00} \left(\frac{\partial \overset{\star}{u}{}^{(0)}_\vartheta}{\partial \tilde{r}} + \frac{\overset{\star}{u}{}^{(0)}_\vartheta}{\tilde{r}} + \overset{\star}{f}_0 \right) = -\overset{\star}{u}{}^{(2)}_{r,*} \left(\frac{\overset{\star}{u}{}^{(0)}_\vartheta}{\tilde{r}} + \overset{\star}{f}_0 \right), \tag{5.1.14a}$$

$$\text{with} \qquad \widetilde{w}^{(1)}_0 = \frac{\overset{\star}{Q}{}^{(2)}_{\Theta,0}}{\overset{\star}{\Theta}{}'_1}, \tag{5.1.14b}$$

$$\overset{\star}{u}{}^{(2)}_{r,*} = \frac{1}{2} \left(\frac{\partial \overset{\star}{X}{}^{(1)}}{\partial \overset{\star}{z}} \widetilde{w}^{(1)}_{12} + \frac{\partial \overset{\star}{Y}{}^{(1)}}{\partial \overset{\star}{z}} \widetilde{w}^{(1)}_{11} \right) \tag{5.1.14c}$$

$$\text{and} \qquad \overset{\star}{u}{}^{(2)}_{r,00} = -\frac{1}{\tilde{r}} \int_0^{\tilde{r}} \frac{r'}{\overset{\star}{\rho}_0} \frac{\partial}{\partial \overset{\star}{z}} \left(\overset{\star}{\rho}_0 \frac{\overset{\star}{Q}{}^{(2)}_{\Theta,0}}{\overset{\star}{\Theta}{}'_1} \right) \mathrm{d}r', \tag{5.1.14d}$$

and for the vertical velocity modes

$$\widetilde{w}^{(1)}_{1k} = \frac{1}{\overset{\star}{\Theta}{}'_1} \left[\overset{\star}{Q}{}^{(2)}_{\Theta,1k} + (-1)^k \frac{\partial \overset{\star}{X}{}^{(1)}_k}{\partial \overset{\star}{z}} \frac{\left(\overset{\star}{u}{}^{(0)}_\vartheta \right)^2}{\tilde{r}} \left(\frac{\overset{\star}{u}{}^{(0)}_\vartheta}{\tilde{r}} + \overset{\star}{f}_0 \right) \right]. \tag{5.1.15}$$

This result from the analysis in Paeschke *et al.* (2012) recovers the findings from Jones (1995) and Frank & Ritchie (1999): it relates vortex tilt with asymmetric potential temperature and vertical velocity patterns for adiabatic TCs.

Assuming that the heat source is solely composed of 1-modes, i.e.

$$\overset{\star}{Q}{}^{(2)}_{\Theta}(\tilde{r},\vartheta,\overset{\star}{z},\overset{\star}{t}) = \overset{\star}{Q}{}^{(2)}_{\Theta,11}\sin\vartheta + \overset{\star}{Q}{}^{(2)}_{\Theta,12}\cos\vartheta, \tag{5.1.16}$$

the core structure will be the same for each level $\overset{\star}{z}$, and $\widetilde{w}^{(1)}_0 = 0$ and $\overset{\star}{u}{}^{(2)}_{r,00} = 0$. In that case, the azimuthal velocity evolves according to the simplified equation

$$\frac{\partial \overset{\star}{u}{}^{(0)}_{\vartheta}}{\partial \overset{\star}{t}} = -\overset{\star}{u}_{r,*}\left(\frac{\overset{\star}{u}{}^{(0)}_{\vartheta}}{\tilde{r}} + \overset{\star}{f}_0\right), \quad \text{where} \tag{5.1.17a}$$

$$\overset{\star}{u}_{r,*} = \frac{1}{2}\frac{1}{\overset{\star}{\Theta}{}'_1}\left(\frac{\partial \overset{\star}{X}{}^{(1)}}{\partial \overset{\star}{z}}\overset{\star}{Q}{}^{(2)}_{\Theta,12} + \frac{\partial \overset{\star}{Y}{}^{(1)}}{\partial \overset{\star}{z}}\overset{\star}{Q}{}^{(2)}_{\Theta,11}\right) \tag{5.1.17b}$$

dropping the upper order index for $\overset{\star}{u}{}^{(2)}_{r,*}$ and using (5.1.15) to have $\overset{\star}{u}_{r,*}$ depend on the heating instead of the vertical velocity.

Moreover, Paeschke *et al.* (2012) derived the *vortex centerline equations of motion*, stating the dependence of the centerline among others on circumferential velocity and its spatial derivatives. Therefore, we expect that the tilt changes with azimuthal velocity and heating. In detail, for this case of a barotropic vortex and vanishing shear flow, inducing motion solely from the initial displacement, Paeschke *et al.* (2012) predict that temporal and spatial change of the centerline are orthogonal, i.e.

$$\frac{\partial \mathbf{X}}{\partial t}\cdot\frac{\partial \mathbf{X}}{\partial z} = 0. \tag{5.1.18}$$

Our goal is to support the stated evolution equations for core structure and centerline with a numerical model. Figures 5.1 show the initial setup and the quantities that we observe in this context. The maximum initial tilt imposed is $A = 160\text{km}$ but we observe in figure 5.1a a difference of about 30 kilometers, i.e. less than two grid spacings. This is due to the choice of the averaging domain $\Sigma = [-200\text{km}, 200\text{km}]^2$ (cf. section 4.3.2), the centerline is placed not far from its boundary and the integral measure leads to stronger deviations. However, this is true for any center point close to the boundary, and judging from the otherwise consistent cosine shape the initial vortex is well suited for our following numerical investigations.

5.2. Implementation

In order to extend the preceding simulation of an adiabatic vortex in EULAG only few changes are necessary. We start with the general idea of the adaption and explain how the presented variables in 5.1 are inserted.

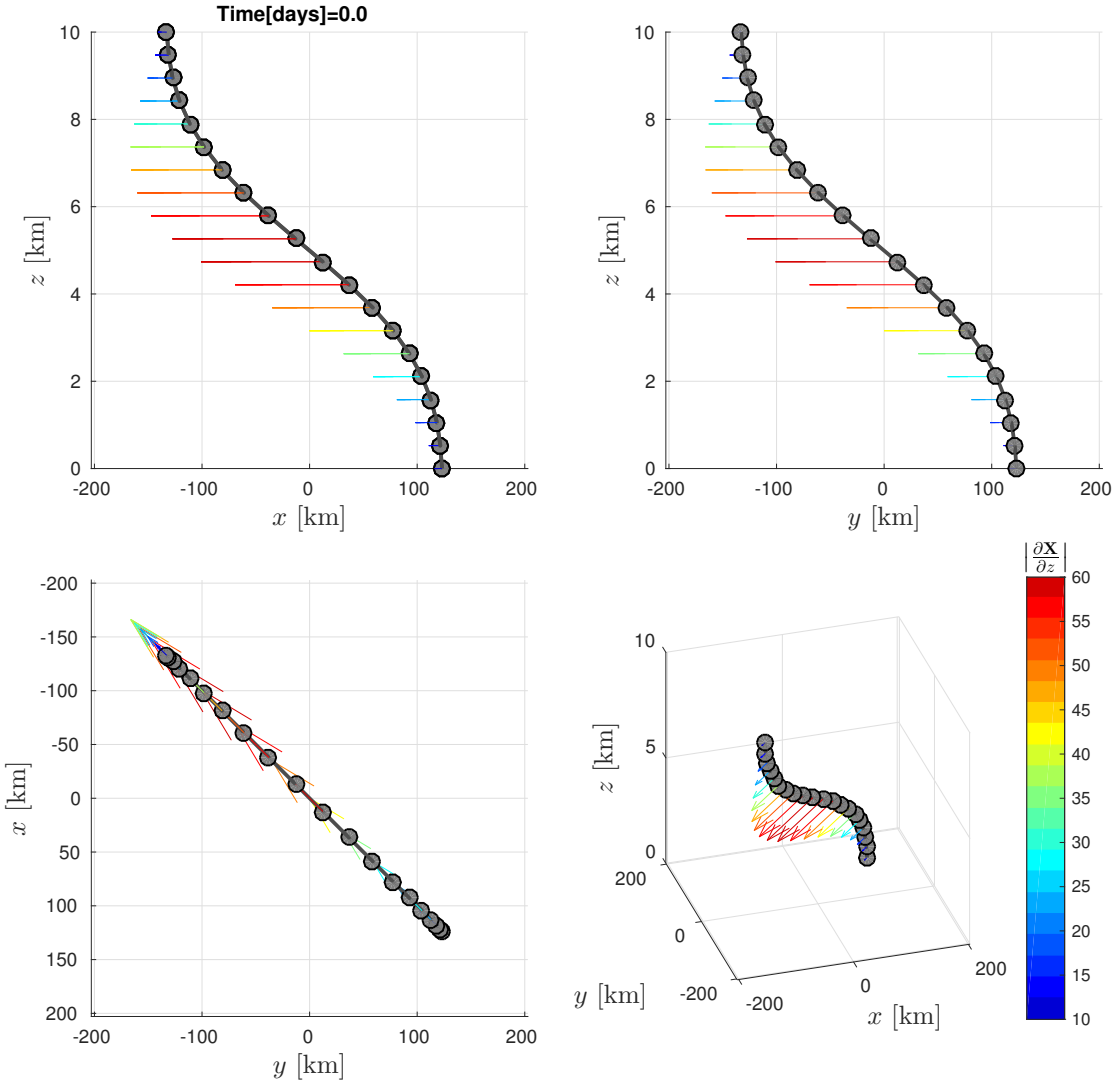

Fig. 5.1a.: Initial vortex centerline. The maximum displacement of 160km for a single vertex is not reached.

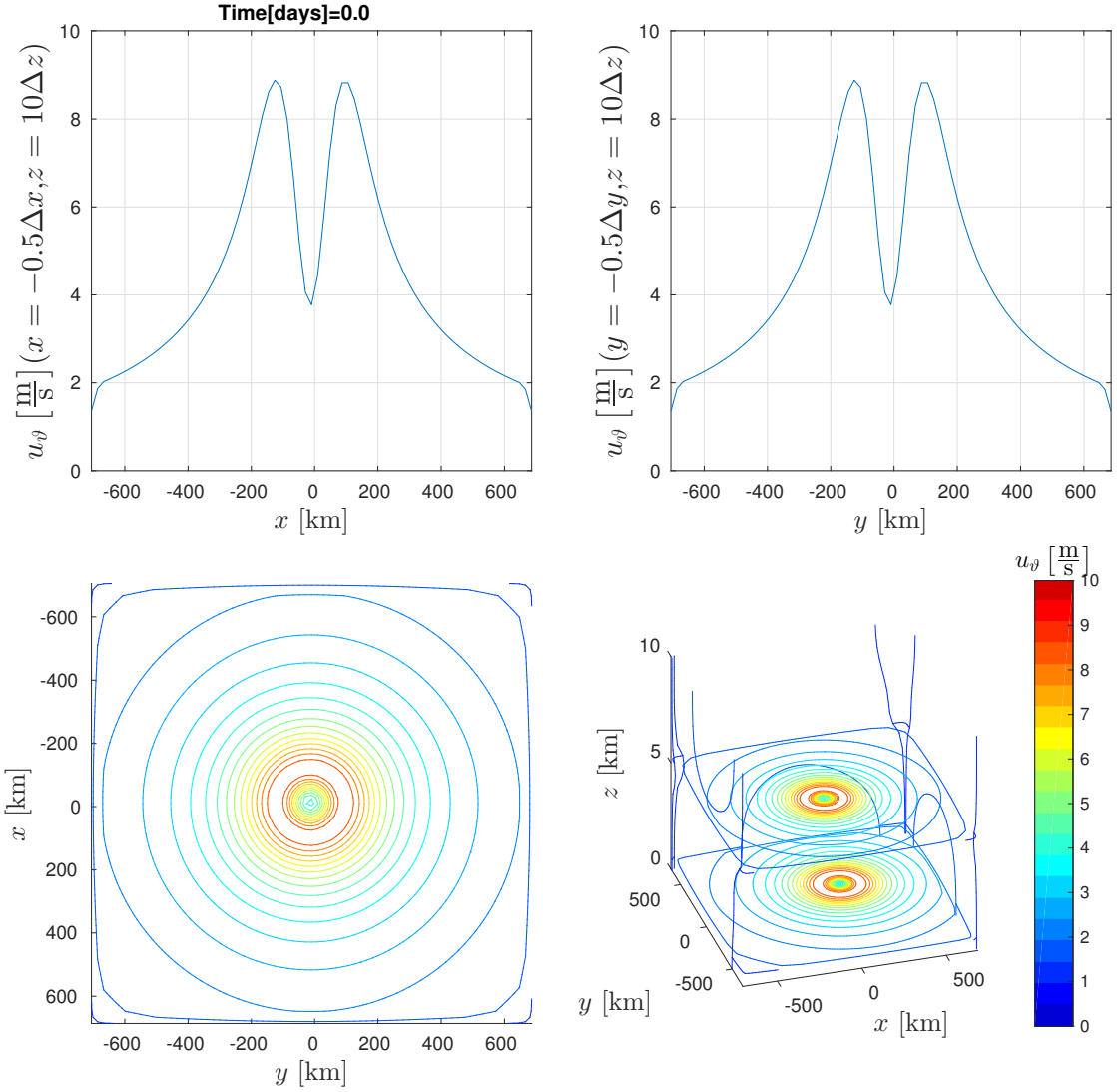

Fig. 5.1b.: Initial azimuthal velocity profile.

The method of Strang splitting that is used in EULAG was briefly outlined in 3.1.3. We will utilize this structure in order to modify the potential temperature according to the conservation of energy (2.1.14c), applicable to any of the available numerical models. With the Euler method we create a function that integrates and sets the potential temperature at half time steps, before and after advection considering the influence of source terms. The discretized variables read

$$\Theta^{\diamond}_{n+1/2} = \Theta^{\diamond}_{n} + \frac{\Delta t}{2} Q_{\Theta,n}^{\diamond}. \tag{5.2.1}$$

In that way, we place this function in the regular EULAG routine twice for each time step, in each call accounting for heating in half a time step.

A question that remains is the choice of the time step. Potential temperature changes in time according to (5.2.1), which in turn gives rise to gravity waves and vertical motion, section 2.2.3, since the heating will generally differ for the vertical layers, i.e. $Q_\Theta(r, \vartheta, z, t)$. The time scale of gravity waves is determined by the Brunt-Väisälä frequency, and if the time step is bigger than N they are not resolved explicitly. This is consistent with the asymptotic approach where the internal waves are suppressed for sufficiently strong mean temperature stratification. However, we use the semi-implicit handling of bouyancy in EULAG in order to retain the influence of gravity waves on the flow. It leads to robust solutions despite $N\Delta t > 1$.

For the numerical model we use $\Delta t = 300$s, although this does not satisfy $N\Delta t < 1$ we find that the results do not differ significantly to the ones with $\Delta t = 10$s. This is a sign for consistency of our approach and justifies the further use of $\Delta t = 300$s. At every eight hours, i.e. in multiples of 96 time steps, we observe the characteristic variables of the system. The time is given in days, and non-integer values are rounded to one decimal place, leaving the possible last digits 0, 3 and 6.

As a remark, imposing this diabatic source happens quasi-stationary, in contrast to a pulse-like behavior. It will become clear later on regarding the specific term of interest, e.g. $\mathcal{Q}$ in figure 5.2b: It is of the order $10^{-5}\mathrm{Ks}^{-1}$, and nondimensionally the heat source is also small, $\Delta t\mathcal{Q}/T_{\mathrm{ref}} = \mathcal{O}(10^{-5})$. The theory presented in Paeschke *et al.* (2012) considers for the vortex core only quasi-stationary processes due to the aforementioned characteristic time scale t_{ref} versus $l_{\mathrm{mes}}/u_{\mathrm{mes}} = \delta^2 t_{\mathrm{ref}}$.

5.3. Vertical motions under heating

The analysis in 5.1 predicted a direct connection between diabatic source and vertical velocity that we aim to reproduce numerically. If not stated otherwise the initial displacement amplitude is $A = 160$km.

5.3.1. Suppressing vertical draft

We utilize the theoretical connection between vertical velocity and diabatic source and

$$\overset{\star}{\mathcal{Q}}_k(\tilde{r},\vartheta,\overset{\star}{z},\overset{\star}{t}) := (-1)^{k+1}\frac{\partial \overset{\star}{X}{}^{(1)}_k}{\partial \overset{\star}{z}}\frac{\left(\overset{\star}{u}{}^{(0)}_\vartheta\right)^2}{\tilde{r}}\left(\frac{\overset{\star}{u}{}^{(0)}_\vartheta}{\tilde{r}}+\overset{\star}{f}_0\right), \tag{5.3.1a}$$

and set

$$\overset{\star}{Q}{}^{(2)}_{\Theta,1k} = \overset{\star}{\mathcal{Q}}_k \tag{5.3.1b}$$

hoping to suppress $\widetilde{w}^{(1)}_{1k}$ according to (5.1.15). Numerically, we would hope to see vertical velocities that are an order of magnitude smaller compared to the case where $Q_\Theta = 0$. However, we did not observe a significant difference in the magnitude of w in our model. A possible explanation for this is a dominant 0-mode of vertical velocity that also occurs for $Q_\Theta = 0$ despite (5.1.14b). Then, the influence of 1-modes is negligible and cannot be measured in this context.

Instead, we analyze the vertical velocity pattern for $Q_\Theta = 0$ and compare it to the heating pattern proposed in (5.3.1).

5.3.2. Weak temperature gradient approximation

On mesoscales the weak-temperature-gradient model is commonly used (Klein *et al.*, 2010), stating at leading order

$$\widetilde{w}^{(1)}\overset{\star}{\Theta}{}'_1 = \overset{\star}{Q}{}^{(2)}_\Theta. \tag{5.3.2}$$

This is consistent with the 0-mode relation in (5.1.14b). It means that to leading order the pattern of heating and vertical velocity agree, and the validity of (5.1.15) for 1-modes is evaluated by the shape. Therefore, an alternative to comparing the magnitude of w for $\overset{\star}{Q}{}^{(2)}_{\Theta,1k} = 0$ and $\overset{\star}{Q}{}^{(2)}_{\Theta,1k} = \overset{\star}{\mathcal{Q}}_k$ is to compare the pattern of w for $\overset{\star}{Q}{}^{(2)}_{\Theta,1k} = 0$ with the pattern of $\overset{\star}{\mathcal{Q}}_k$. According to (5.1.15) and (5.3.1) the vertical velocity $\widetilde{w}^{(1)}_{1k}$ for $\overset{\star}{Q}{}^{(2)}_{\Theta,1k} = 0$ exhibits the same mode structure as $\overset{\star}{\mathcal{Q}}_k$ up to a sign.

This is now subject to numerical investigation, starting from the case highlighted in figures 5.1. An adiabatic vortex is modeled and the corresponding heat source via (5.3.1) is only calculated but not imposed. Figures 5.2 and 5.3 show the vertical velocity for $\overset{\star}{Q}{}^{(2)}_{\Theta,1k} = 0$ and $\overset{\star}{\mathcal{Q}}_k$ at two different times. Indeed we observe that their dipole structure moves with the same speed and their sign is exactly opposite. Further, the vertical velocity profile is slightly disturbed, the oscillations might occur from small instabilities inducing vertical motion.

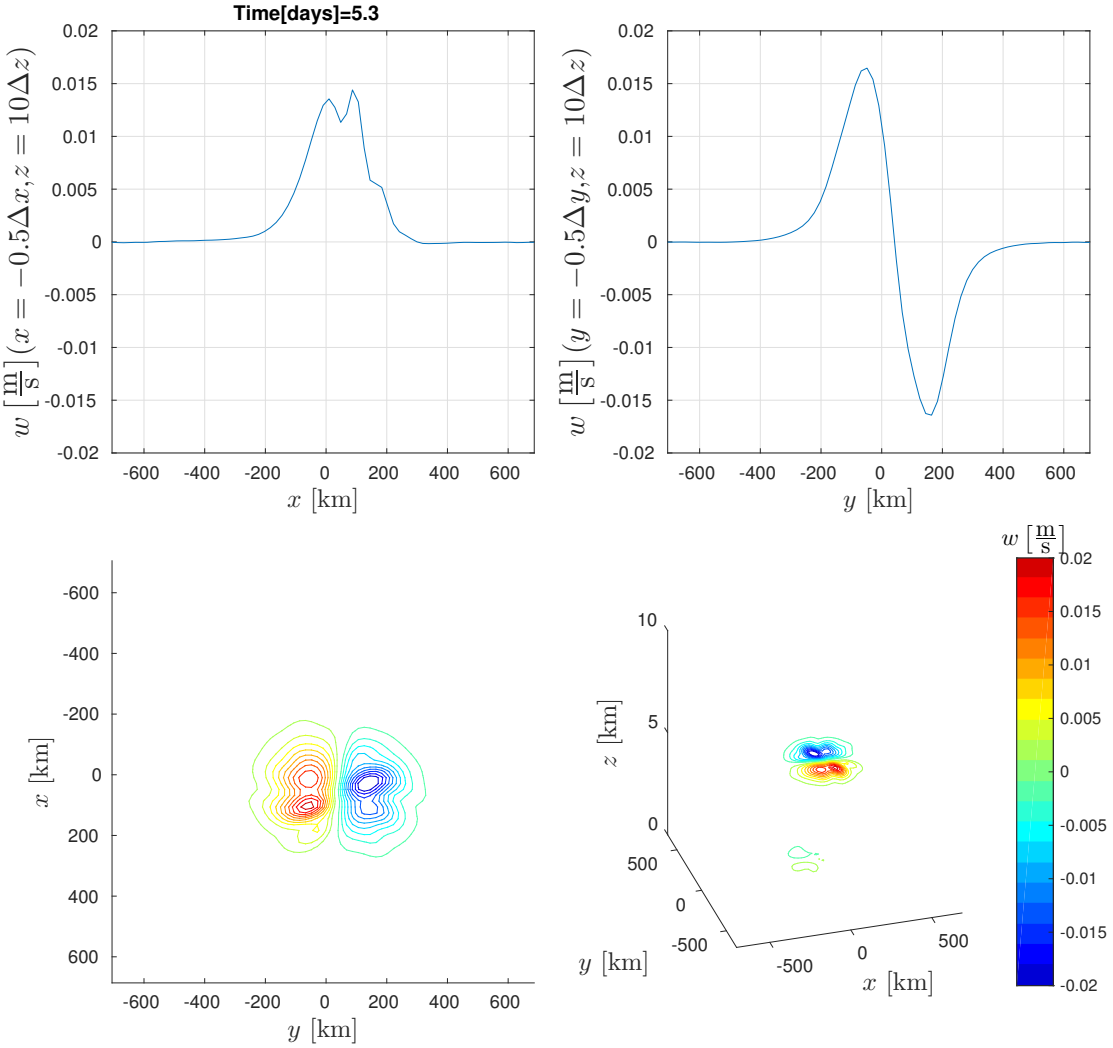

Fig. 5.2a.: Emphasizing the relationship between adiabatic vertical velocity w and $\mathcal{Q}$ after nine days. The vertical velocity is smoothed with a simple Gaussian filter.

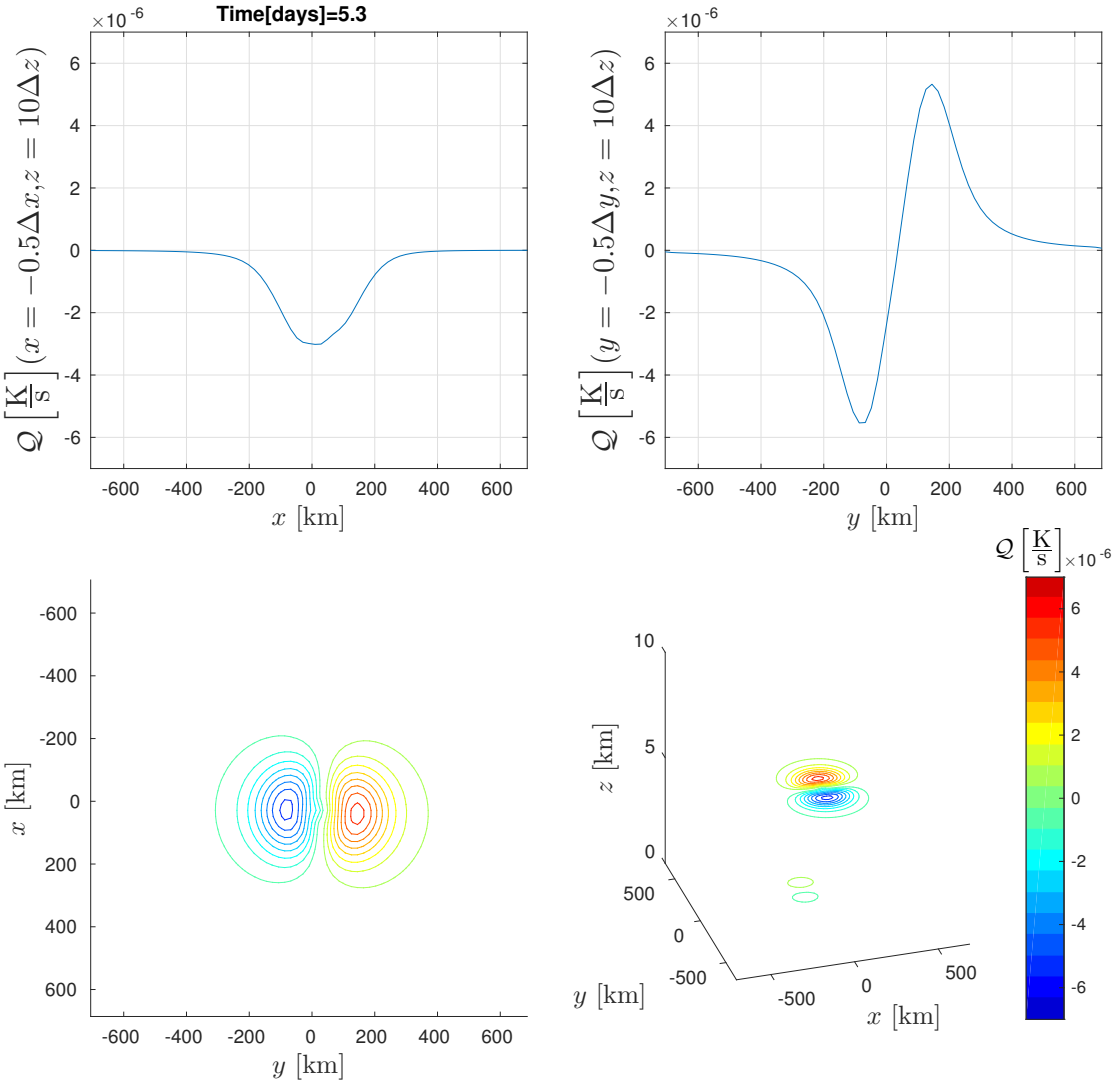

Fig. 5.2b.: Diabatic heating $\mathcal{Q}$ is to be compared with w in figure 5.2a (page 73). The dipole structure of both w and $\mathcal{Q}$ variables coincides up to the sign.

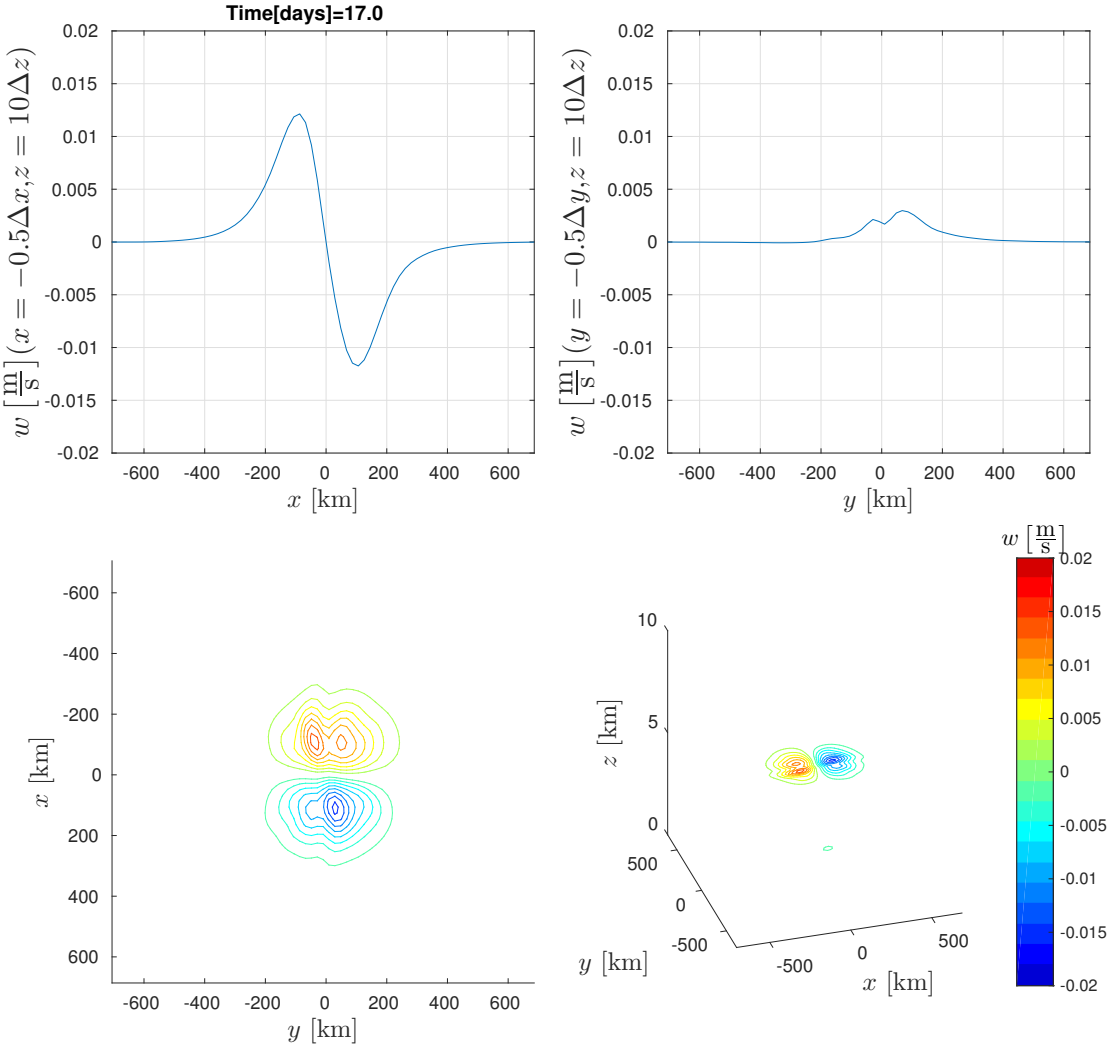

Fig. 5.3a.: Same as figure 5.2a (page 73), but after 17 days.

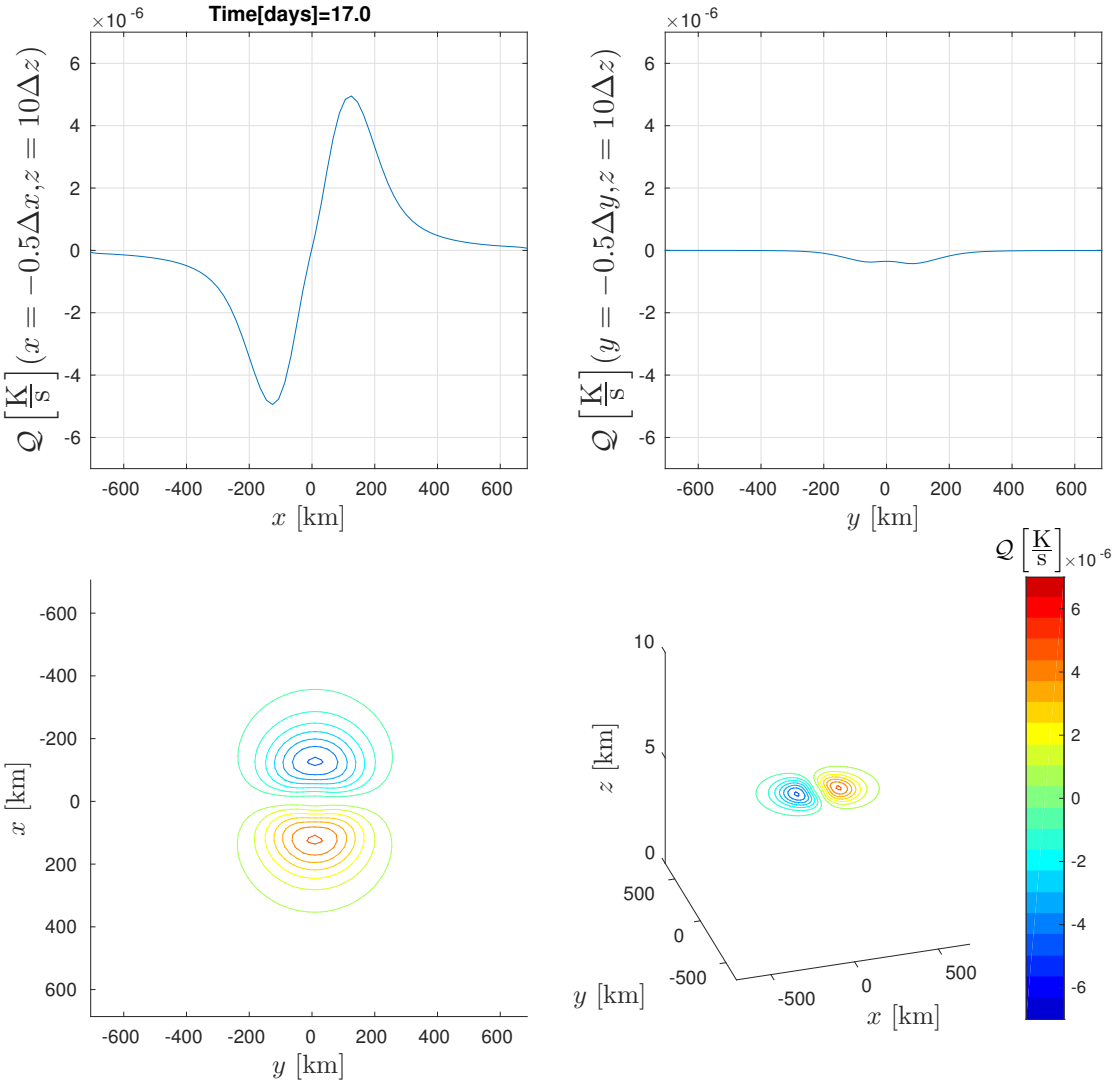

Fig. 5.3b.: Same as figure 5.2b (page 74), but after 17 days.

5.4. Core evolution

Similar to the preceding section we will now impose different diabatic source terms, all solely composed of 1-modes such that we expect the simplified core structure evolution equation (5.1.17) to hold. Accordingly, $\overset{\star}{u}_{r,*}$ is the forcing for the circumferential velocity $\overset{\star}{u}^{(0)}_{\vartheta}$, and since $\overset{\star}{u}^{(0)}_{\vartheta}, \tilde{r}, \overset{\star}{f}_0 > 0$ the sign of $\overset{\star}{u}_{r,*}$ will determine if it has strengthening or weakening character. Regarding (5.1.17b) tilt and heat source play a major role in this.

5.4.1. Stationary core structure

At this point we discuss the cases where $\overset{\star}{u}_{r,*} = 0$, leading to a core structure that remains unchanged in time, cf. (5.1.17). Note that these profiles are nevertheless subject to horizontal advection. Besides the obvious choice of $Q_\Theta \equiv 0$, i.e. the adiabatic case, certain Fourier coefficients also lead to a time-independent $\overset{\star}{u}^{(0)}_{\vartheta}$. We remember the case with (5.3.1), that implies

$$\overset{\star}{u}_{r,*} = \frac{1}{2}\frac{1}{\overset{\star}{\Theta}_1'}\left[-\frac{\partial \overset{\star}{X}^{(1)}}{\partial \overset{\star}{z}}\frac{\partial \overset{\star}{Y}^{(1)}}{\partial \overset{\star}{z}} + \frac{\partial \overset{\star}{Y}^{(1)}}{\partial \overset{\star}{z}}\frac{\partial \overset{\star}{X}^{(1)}}{\partial \overset{\star}{z}}\right]\frac{\left(\overset{\star}{u}^{(0)}_{\vartheta}\right)^2}{\tilde{r}}\left(\frac{\overset{\star}{u}^{(0)}_{\vartheta}}{\tilde{r}} + \overset{\star}{f}_0\right) = 0 \tag{5.4.1}$$

i.e. a stationary core structure. While we could not specifically show the modal relation of w and Q_Θ we indirectly use it to arrive at the simplified core structure evolution equation. We indeed observe that this case corresponds to zero forcing, the azimuthal velocity is changing in time only slightly, its profile is almost constantly advected (figure 5.4). Most of the decrease in maximum wind speed is happening within the first time steps, possibly due to a small mismatch of the initial setup. Moreover, the vortex centerline precesses but is not deformed significantly. It solely rotates and keeps its fixed shape. This is in agreement with the theoretical dependence of the centerline: a symmetric heating pattern and a constant core structure sustain in an otherwise unchanged environment the centerline (Paeschke *et al.*, 2012).
We refer the reader to appendix A.1 where an excerpt of the velocity, pressure and potential temperature profiles for this case are shown.

5.4.2. Attenuation

Subsequently, we consider a certain modification of the diabatic term.
We note that due to the Fourier representation (5.1.16) rotating the heat source by $\pi/2$ exchanges the sine and cosine coefficients and possibly the sign,

$$\overset{\star}{Q}^{(2)}_\Theta\left(\tilde{r}, \vartheta \pm \frac{\pi}{2}, \overset{\star}{z}, \overset{\star}{t}\right) = \mp\left[\overset{\star}{Q}^{(2)}_{\Theta,11}\cos\vartheta + \overset{\star}{Q}^{(2)}_{\Theta,12}\sin\vartheta\right]. \tag{5.4.2}$$

The specific choice of the diabatic heat source resulted in a vanishing forcing in (5.4.1), horizontal and vertical tilt were multiplied with each other. If instead $\overset{\star}{Q}^{(2)}_\Theta$ is rotated by

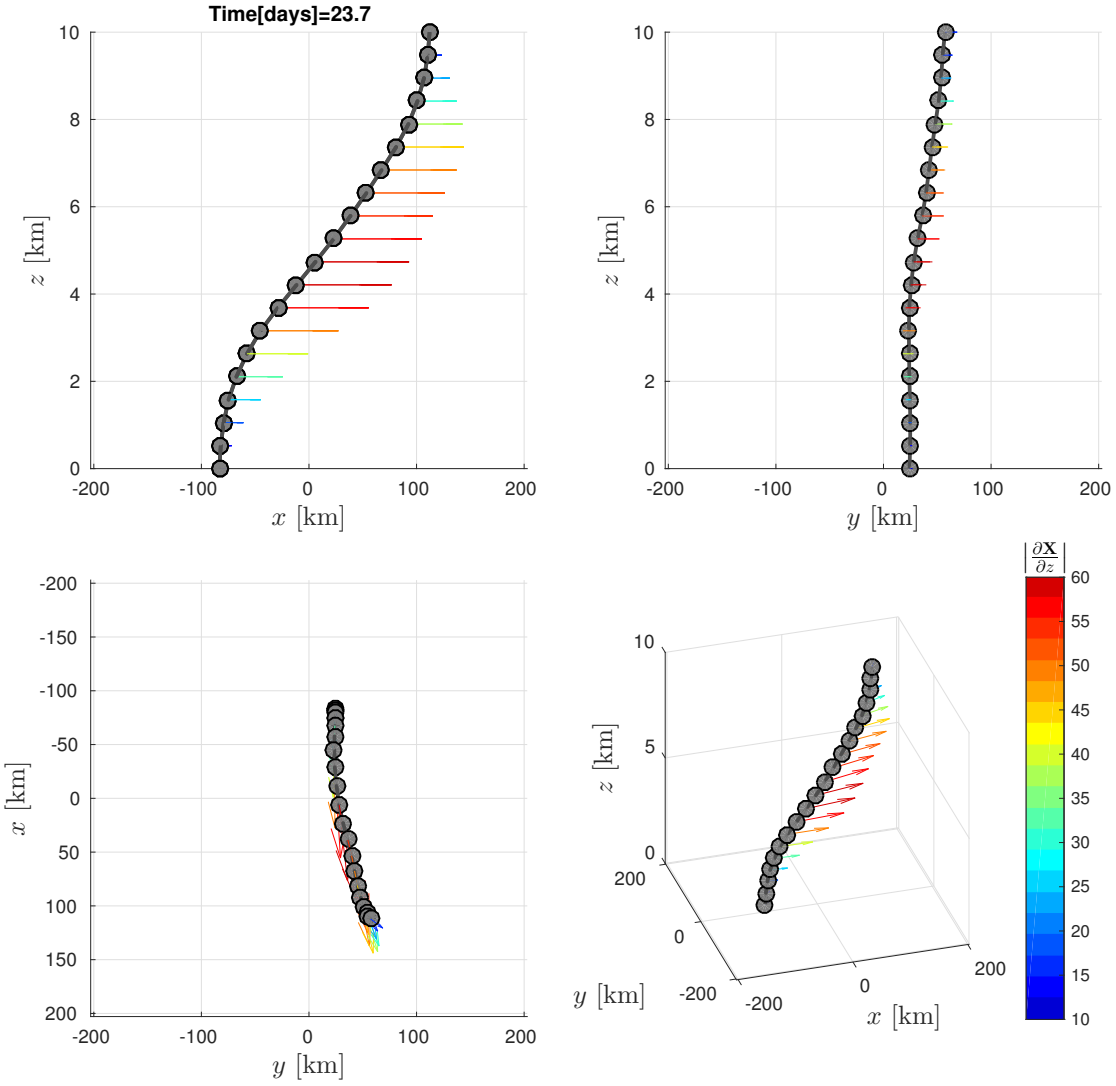

Fig. 5.4a.: Vortex centerline after more than 23 days. Stationary core structure.

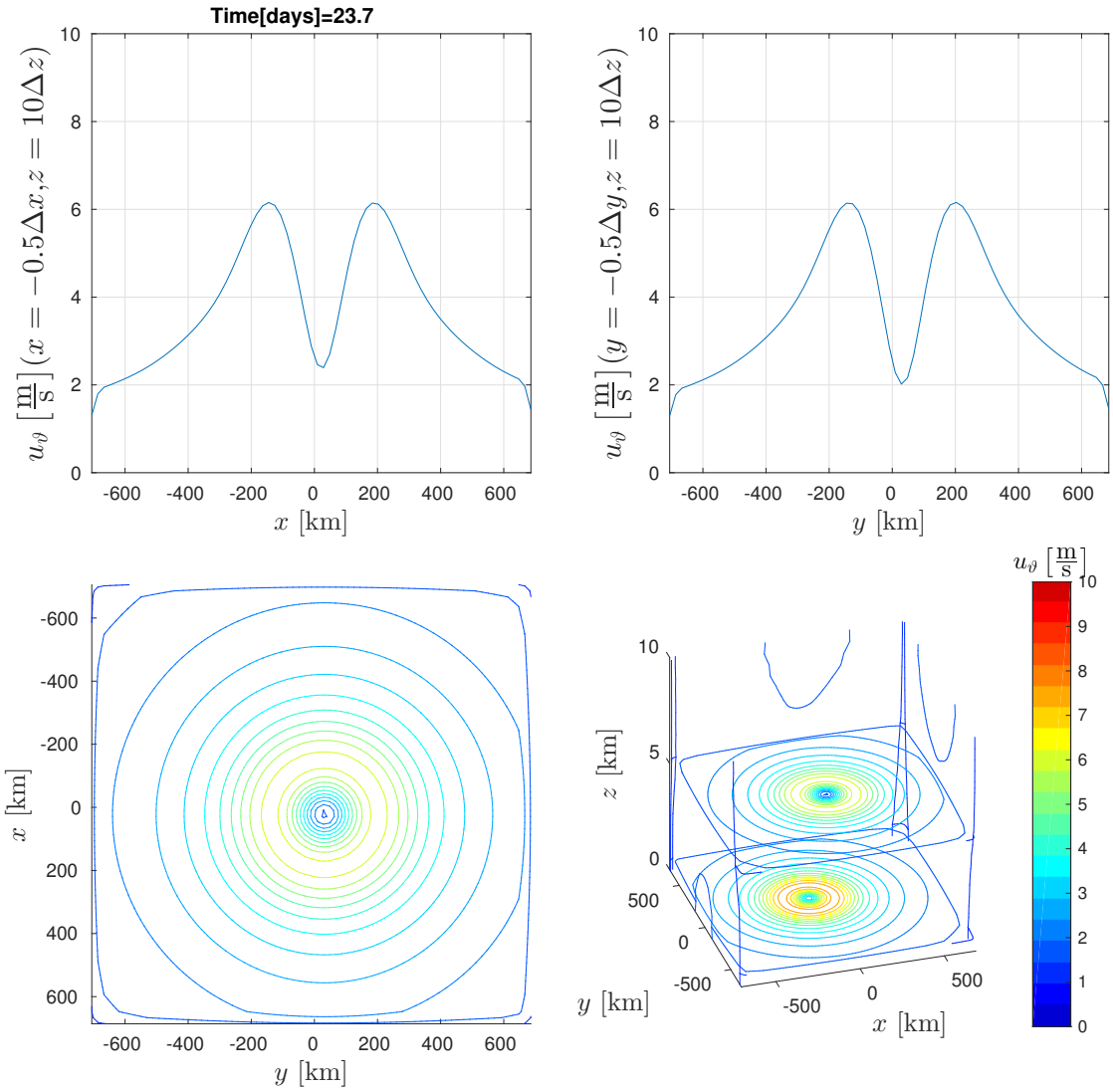

Fig. 5.4b.: Azimuthal velocity in case of stationary core structure.

$\pi/2$ we obtain a contribution of the squared absolute value of the tilt,

$$\left|\frac{\partial \overset{\star}{\mathbf{X}}^{(1)}}{\partial \overset{\star}{z}}\right|^2 = \left(\frac{\partial \overset{\star}{X}^{(1)}}{\partial \overset{\star}{z}}\right)^2 + \left(\frac{\partial \overset{\star}{Y}^{(1)}}{\partial \overset{\star}{z}}\right)^2 . \tag{5.4.3}$$

Consequently, we will distinguish two different forcings, corresponding to a rotation by $\pm\pi/2$:

$$\overset{\star}{u}^{\pm}_{r,*} = \mp \frac{1}{2\overset{\star}{\Theta}_1'} \left|\frac{\partial \overset{\star}{\mathbf{X}}^{(1)}}{\partial \overset{\star}{z}}\right|^2 \frac{\left(\overset{\star}{u}^{(0)}_{\vartheta}\right)^2}{\tilde{r}} \left(\frac{\overset{\star}{u}^{(0)}_{\vartheta}}{\tilde{r}} + \overset{\star}{f}_0\right). \tag{5.4.4}$$

If rotated by $+\pi/2$ the forcing is negative, i.e. $\overset{\star}{u}_{r,*} = \overset{\star}{u}^{+}_{r,*} < 0$, and vice versa. In the first case we expect a weakening of the azimuthal velocity and thus of the vortex strength. Additionally, the centerline will change in time and space. We observe in figures 5.5 that the centerline straightens and the tilt is thus shrinking. Further, the precession amplitude decreases. However, the velocity (5.5b) decreases only slightly and slowly in time. Since the forcing depends on the tilt, with vanishing tilt the forcing will decrease.

If the forcing is chosen ten times as big, i.e. $\overset{\star}{u}_{r,*} = 10\overset{\star}{u}^{+}_{r,*}$, we observe a faster reduction in velocity, see figures 5.6. After more than 23 days the maximum azimuthal velocity differs by about $0.5\mathrm{ms}^{-1}$ from the preceding regime in figure 5.5. The tilt is almost zero everywhere, thus is the heat source and the forcing (additional figures are presented in appendix A.2). Consequently, the change in azimuthal velocity stagnates, in agreement with the evolution equation.

5.4.3. Amplification

In the second case introduced in (5.4.4) we have $\overset{\star}{u}_{r,*} = \overset{\star}{u}^{-}_{r,*} > 0$, i.e. an intensifying vortex: The azimuthal velocity, and with it the maximum wind speed, are expected to grow. At this point we face the challenge of an exploding Courant number due to the problem setup since the increase in vertical velocity is high. Additionally, the domain Σ becomes too small with an initial displacement of already 160km and a likely increase. Therefore, we consider for this case only $A = 80\mathrm{km}$, the initial setup does not differ vastly from figures 5.1 and we refer the reader to appendix A.3 for the respective plots.

Figure 5.7 shows that as theoretically predicted the amplitude of precession increases and the centerline is deformed. These are, after nine days and with regards to later times, the biggest displacement and velocity of a single system. Up to now, the vertical velocity exhibits a dipole structure similar to the one for the neutral forcing (figure 5.2a) but with stronger up- and downdrafts. Shortly after, this structure changes immensely in the observed vertical mid-level, cf. figure 5.8a after 9.3 days. More than two days later, after 11.7 days, at the same level we find a split dipole in figure 5.8b. While it is unclear whether an incipient stage TC would survive such long, we will discuss the abrupt change in dynamics in the following to better understand the observed event.

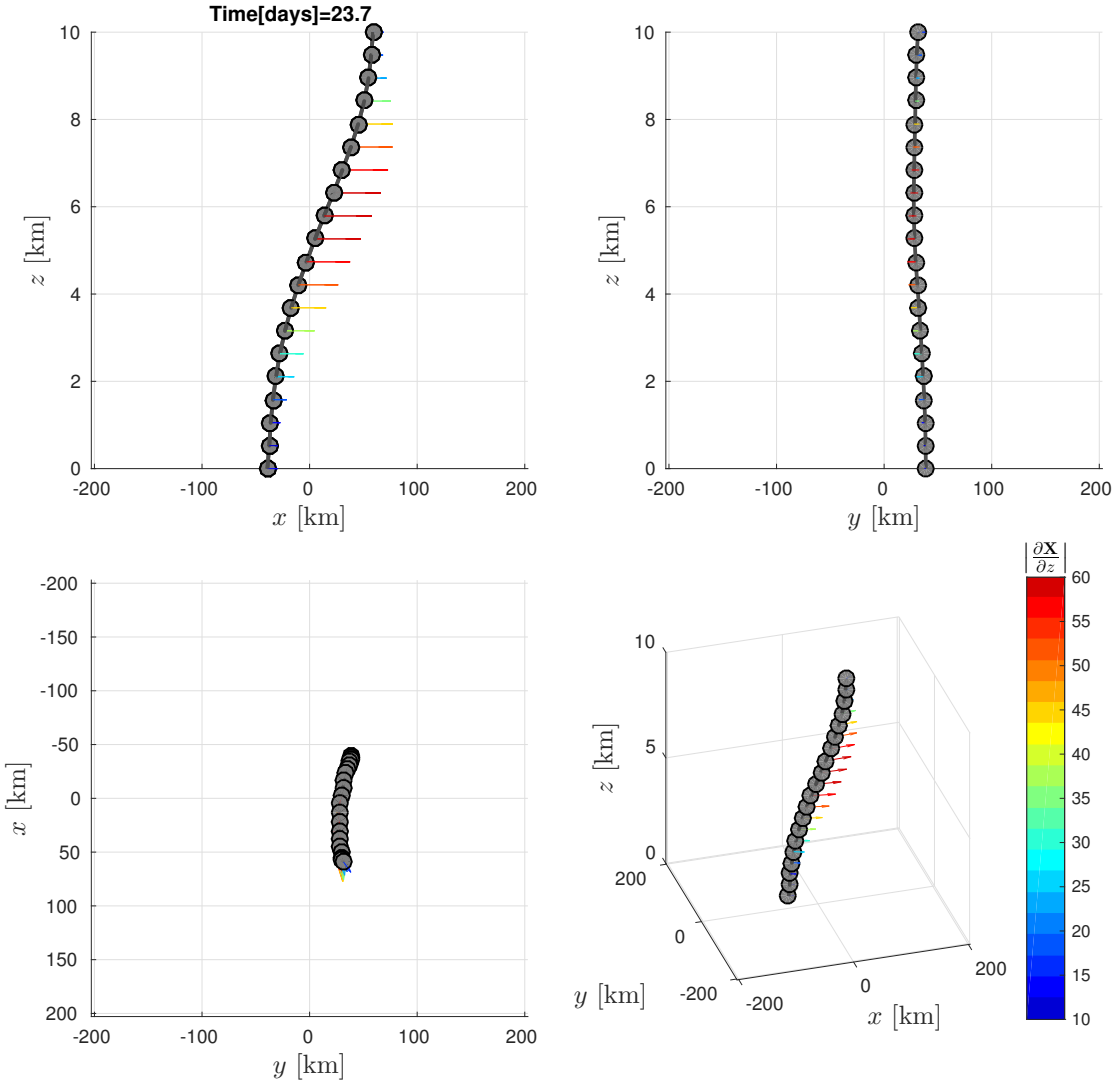

Fig. 5.5a.: Centerline of weakening vortex. The amplitude has decreased significantly.

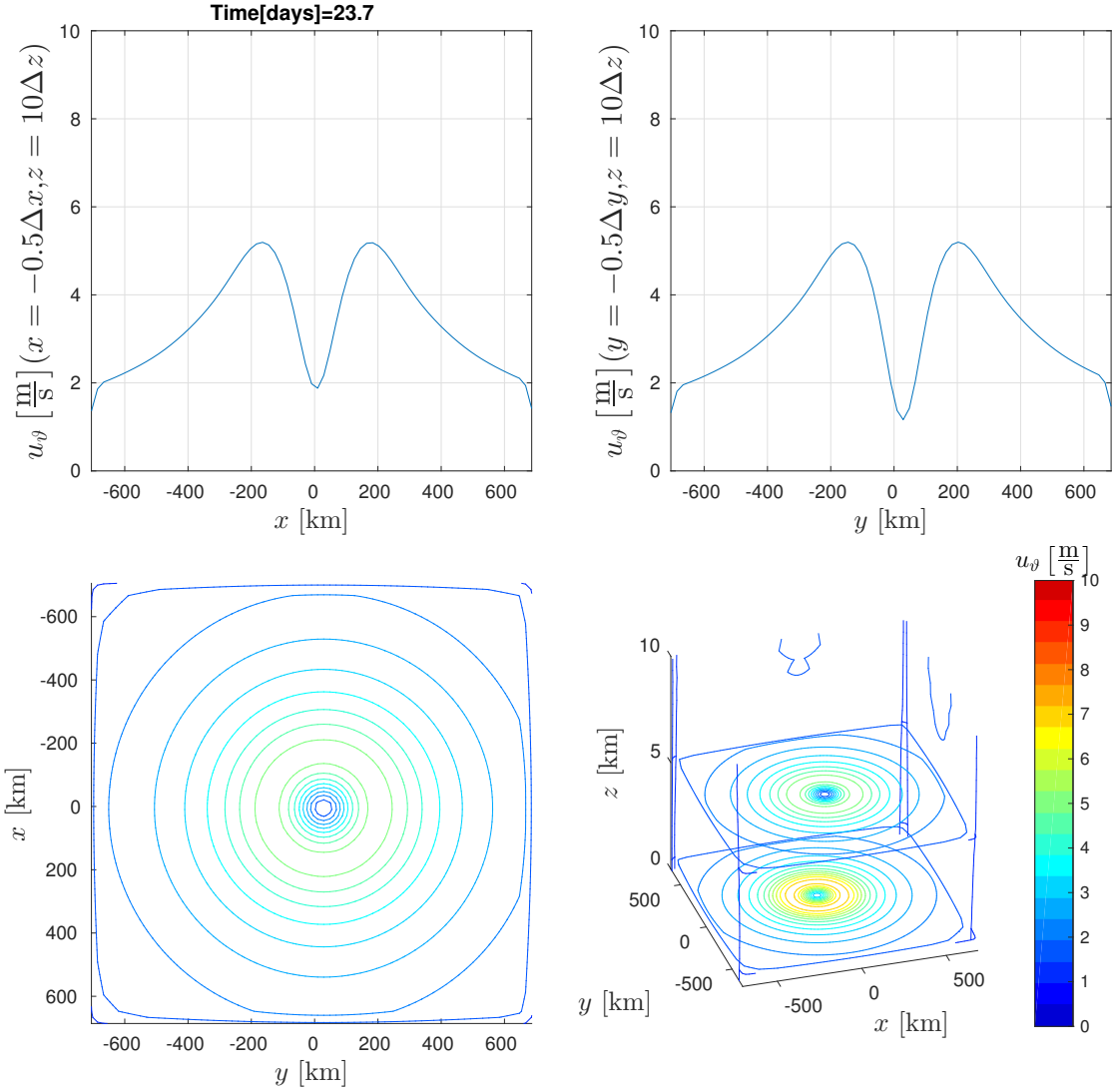

Fig. 5.5b.: Azimuthal velocity of weakening vortex. A significant decrease in velocity compared to the initial state is observed at mid-level.

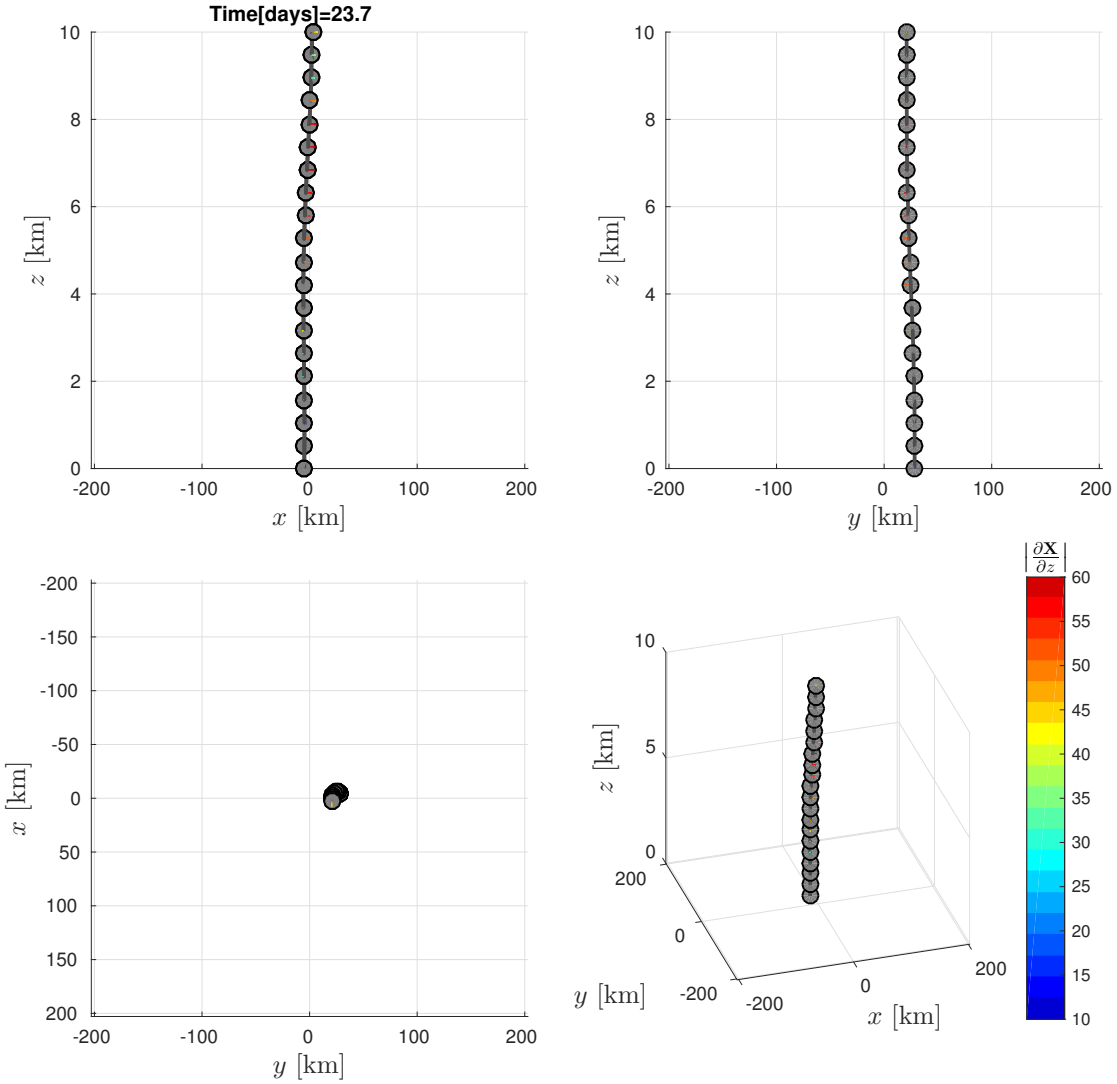

Fig. 5.6a.: Centerline of extremely weakened vortex. The centerline is straight up to small deviations.

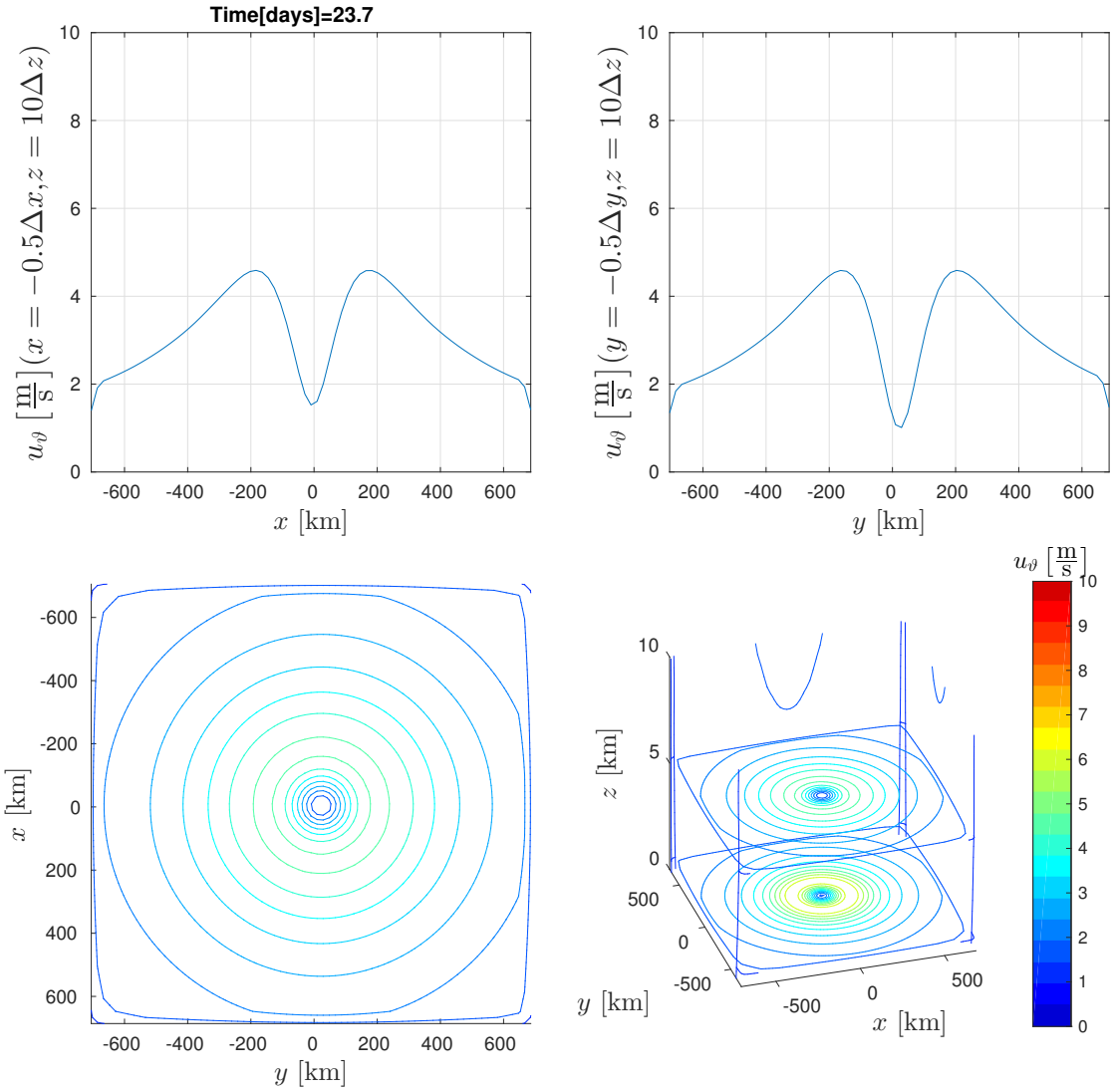

Fig. 5.6b.: Azimuthal velocity for extremely weakened vortex. The maximum value is even lower than for the simple weakening regime in figure 5.5b (page 82), however a further decrease is not observed.

For the critical impact at 9.3 days we further examine in figures 5.9 azimuthal velocity and pressure. The latter shows a spot of higher pressure in the top region, it will vanish not long after. For u_ϑ we observe a low value at the bottom of the domain. During this time, the centerline is distorted, it exhibits a cusp and upper and lower part seem to evolve independently. Figures 5.10 show centerline, azimuthal velocity and pressure after 22.3 days, long after the impact. The vertical velocity decreased vastly in the levels that we observe. Two different vortex parts can be distinguished with regards to the centerline and the pressure profile. The levels considered for the azimuthal velocity belong to the vortex in the low layer, we find that it is much smaller than before the impact and it oscillates just slightly around 6ms^{-1}.

After the splitting event both vortices retain the precession, but the second cell in the top layer drifts further away and the pressure in its center increases. While the tilt of the centerline decreases the vortex itself moves within the inner domain.

The sudden impact and its consequences can be understood with help of the pressure profile and the azimuthal velocity long after it (figures 5.10): At the mid-level height the circumferential velocity is much smaller than at the bottom, and the extent of the pressure drop indicates that the storm did split under shearing. The ongoing positive forcing has reached a point where the vortex could not sustain the shear anymore and drifted apart. The remaining cell at the lower vertical layer is not as tall anymore and does not exhibit a growing azimuthal velocity, yet is stronger than the vortex in the upper layer.

However, it is not certain if this is a realistic szenario for a TC in the incipient regime, by that time it might have faded or turned into a mature hurricane due to environmental disturbances.

5.5. Centerline evolution

The most recent result on the positively driven vortex suggested that the centerline will not only be conserved, stretched or compressed. Instead, it can be torn apart with the vortex itself. In the following part we will take a closer look at the influence of a local heat source predominantly in the region of the centerline and the relation of tilt and centerline evolution in time.

5.5.1. Local driving

An option to construct a heat source that mainly influences the inner part of the vortex is through complementing the source term (5.4.2) with a Gaussian, e.g.

$$Q^{(2)}_{\Theta,1k} = \frac{\mathcal{Q}_k\left(r, \vartheta - \frac{\pi}{2}, z, t\right)}{\sqrt{2\pi} r_C} \exp\left[-\frac{1}{2}\left(\frac{r}{r_C}\right)^2\right]. \tag{5.5.1}$$

The radius r_C is the standard deviation, and we choose $r_C = 200\text{km}$. This locally drives the vortex and potentially we find a different behavior than for the overall intensifying

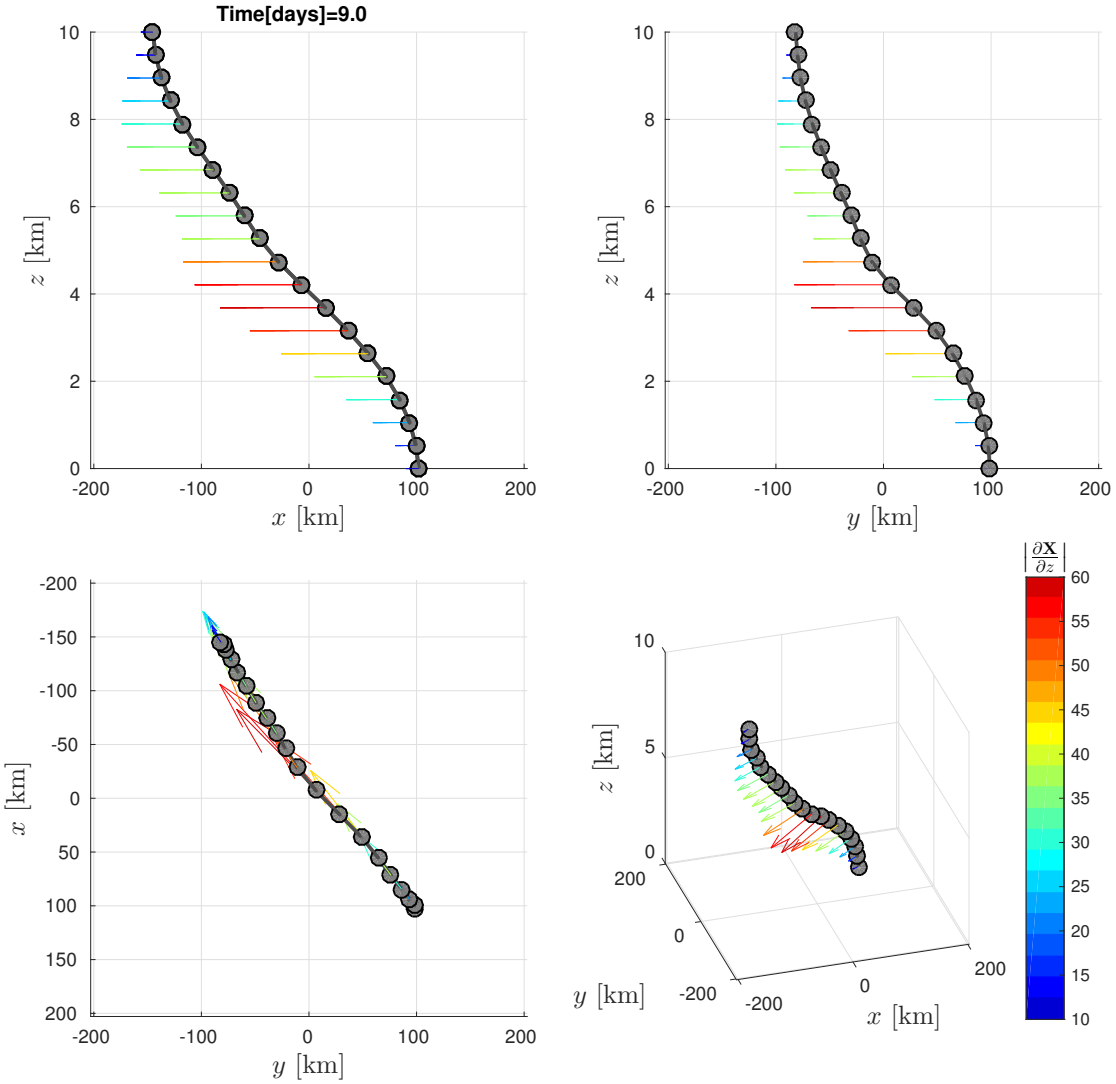

Fig. 5.7a.: Vortex centerline of intensifying vortex. We observe a wide stretched centerline starting from a displacement of 80km going now up to about 150km.

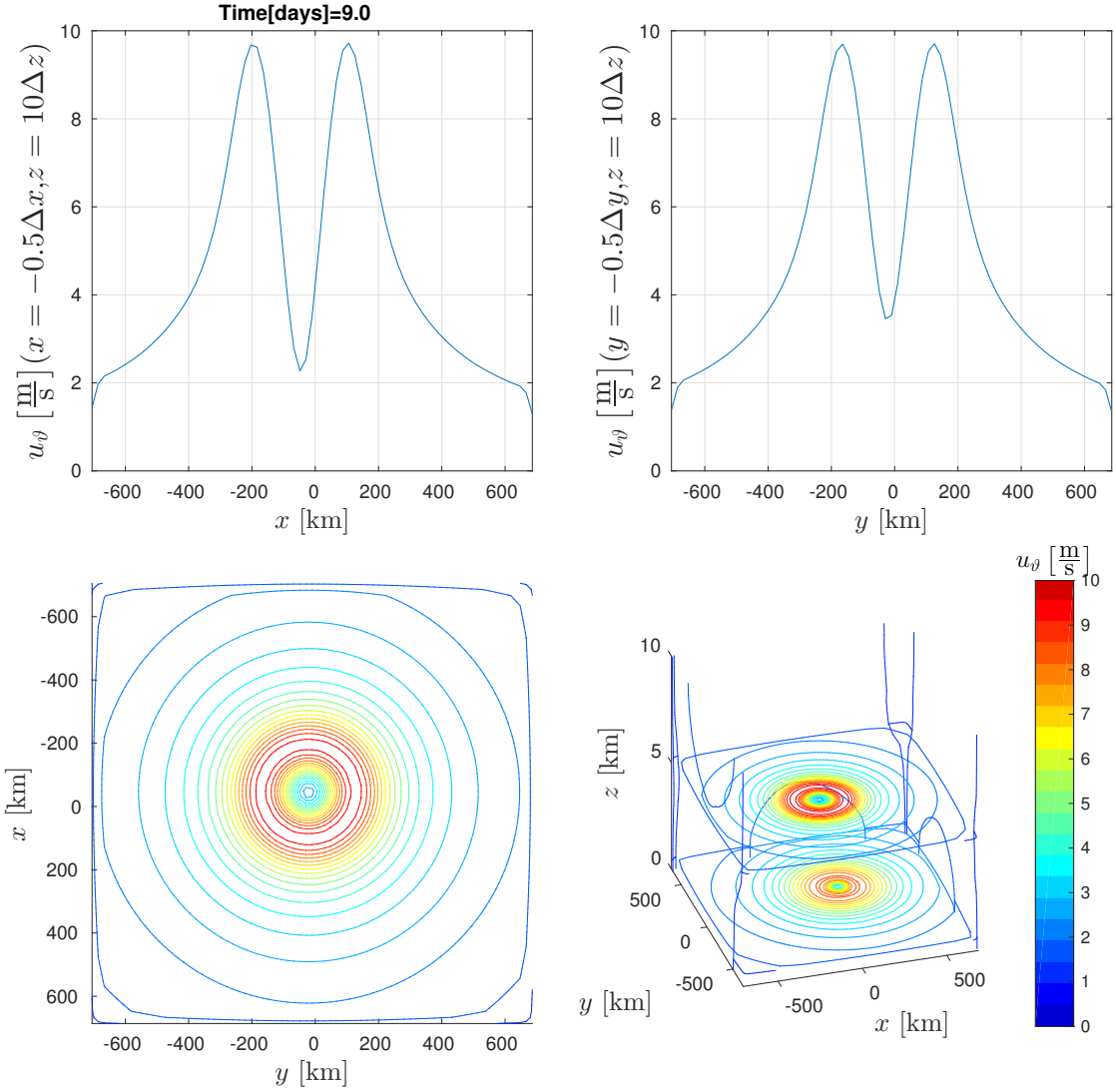

Fig. 5.7b.: Intensifying regime, azimuthal velocity. We see here one of the highest values reached within the time series.

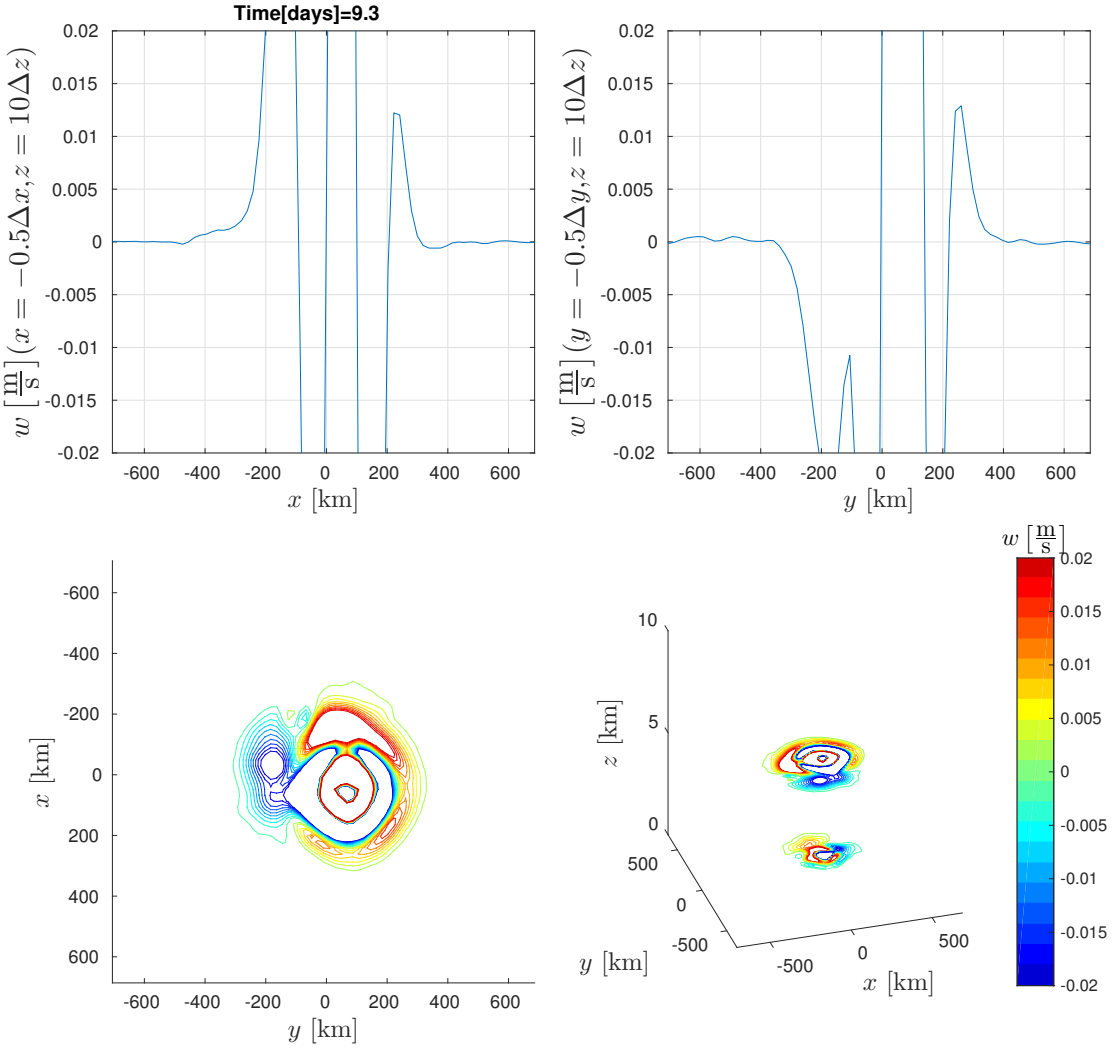

Fig. 5.8a.: Critical event, this "impact" becomes clear when looking at the vertical velocity. It highlights up- and downdrafts in the vortex center.

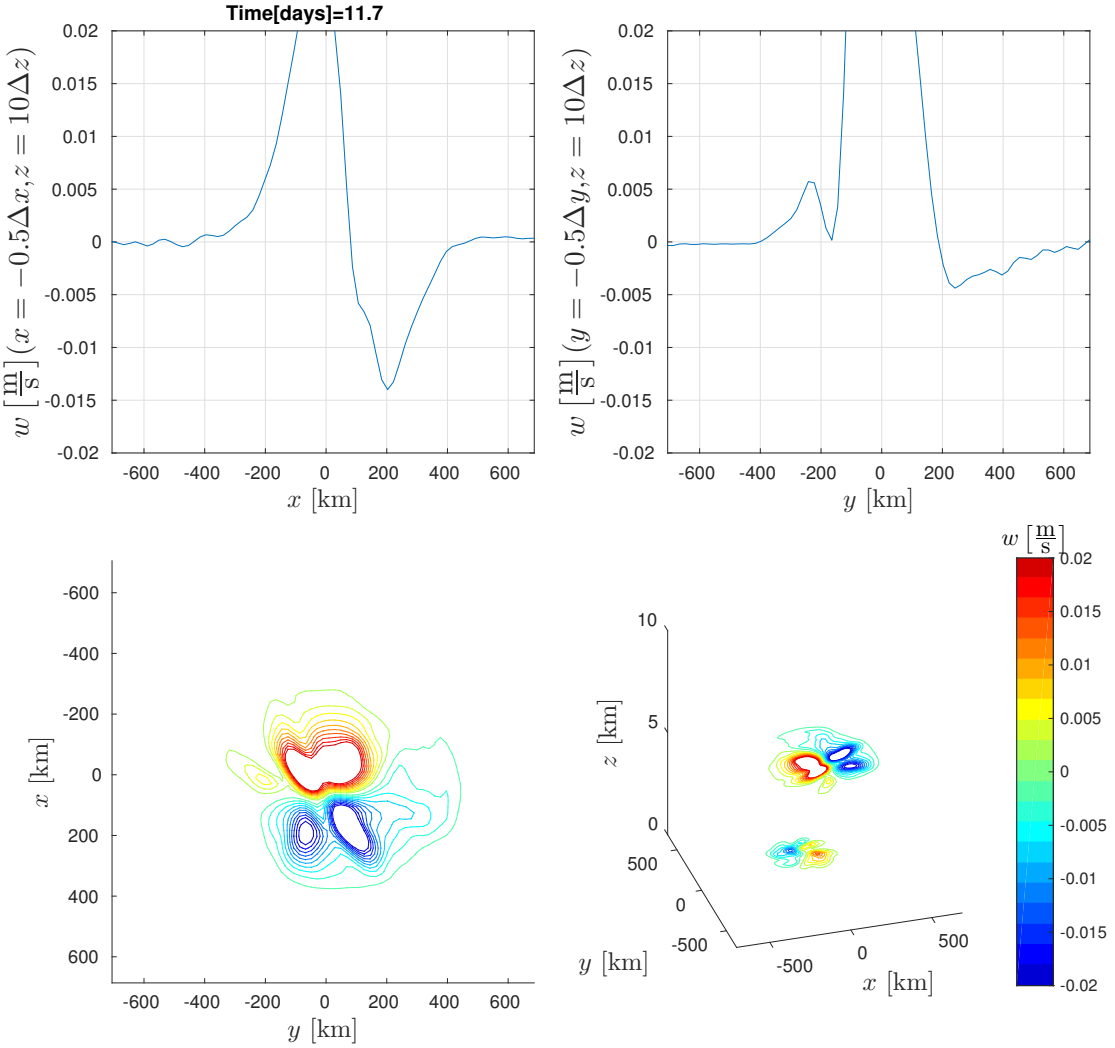

Fig. 5.8b.: Vertical velocity of intensifying vortex 2.4 days after the impact. The main dipole structure is visible again, however it looks like two dipole structures were mixed.

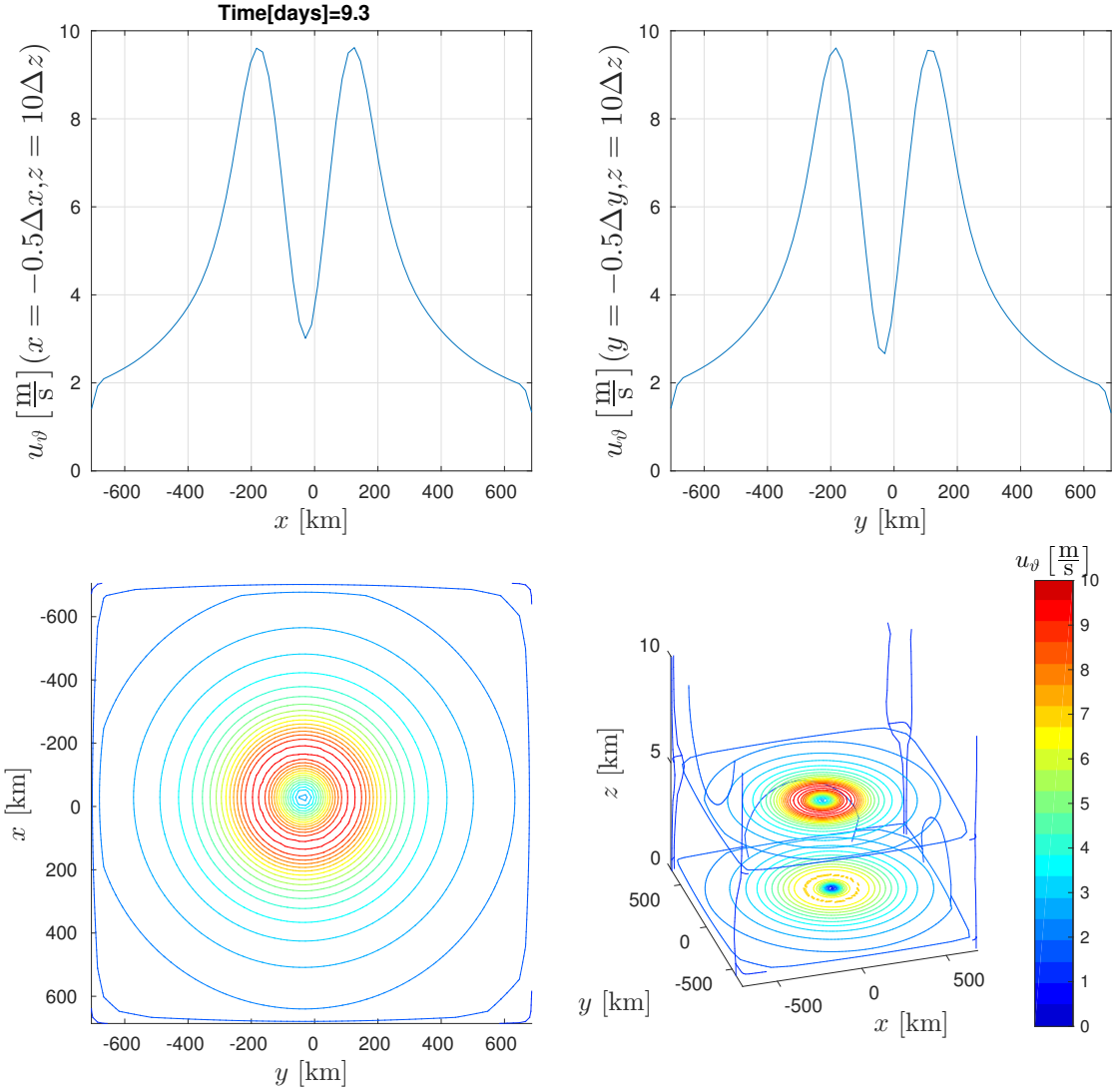

Fig. 5.9a.: Intensifying regime, azimuthal velocity at time of impact. We highlight the drop in azimuthal velocity at the bottom of the domain.

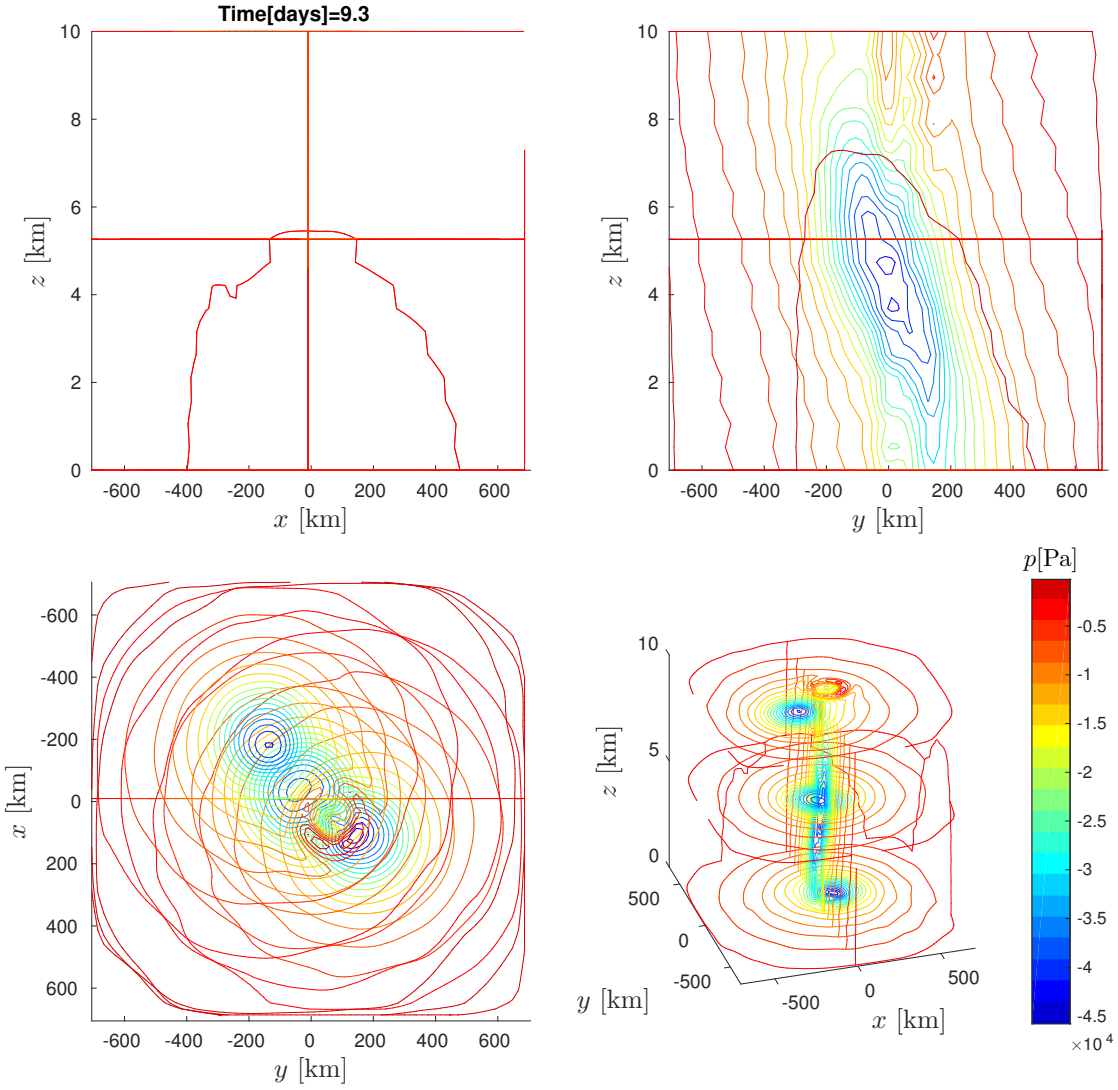

Fig. 5.9b.: Intensifying regime, pressure at time of impact. At the top level a spot of higher pressure appears but will not be distinguishable at other time splits.

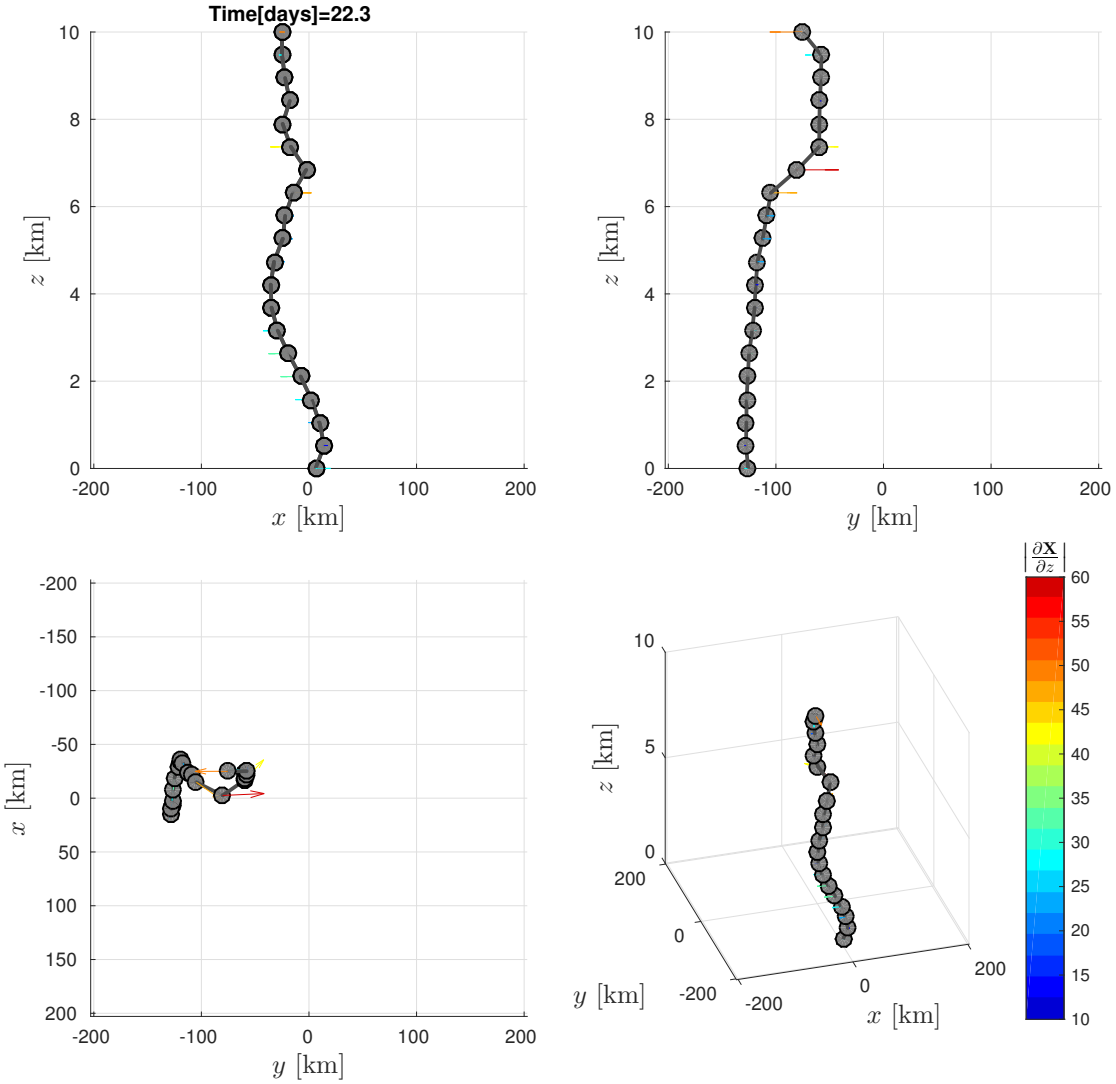

Fig. 5.10a.: Vortex centerline of intensifying vortex long after impact. Between 6km and 8km height we recognize a sudden change in shape, indicating that these are in fact two independent centerlines for two vortices.

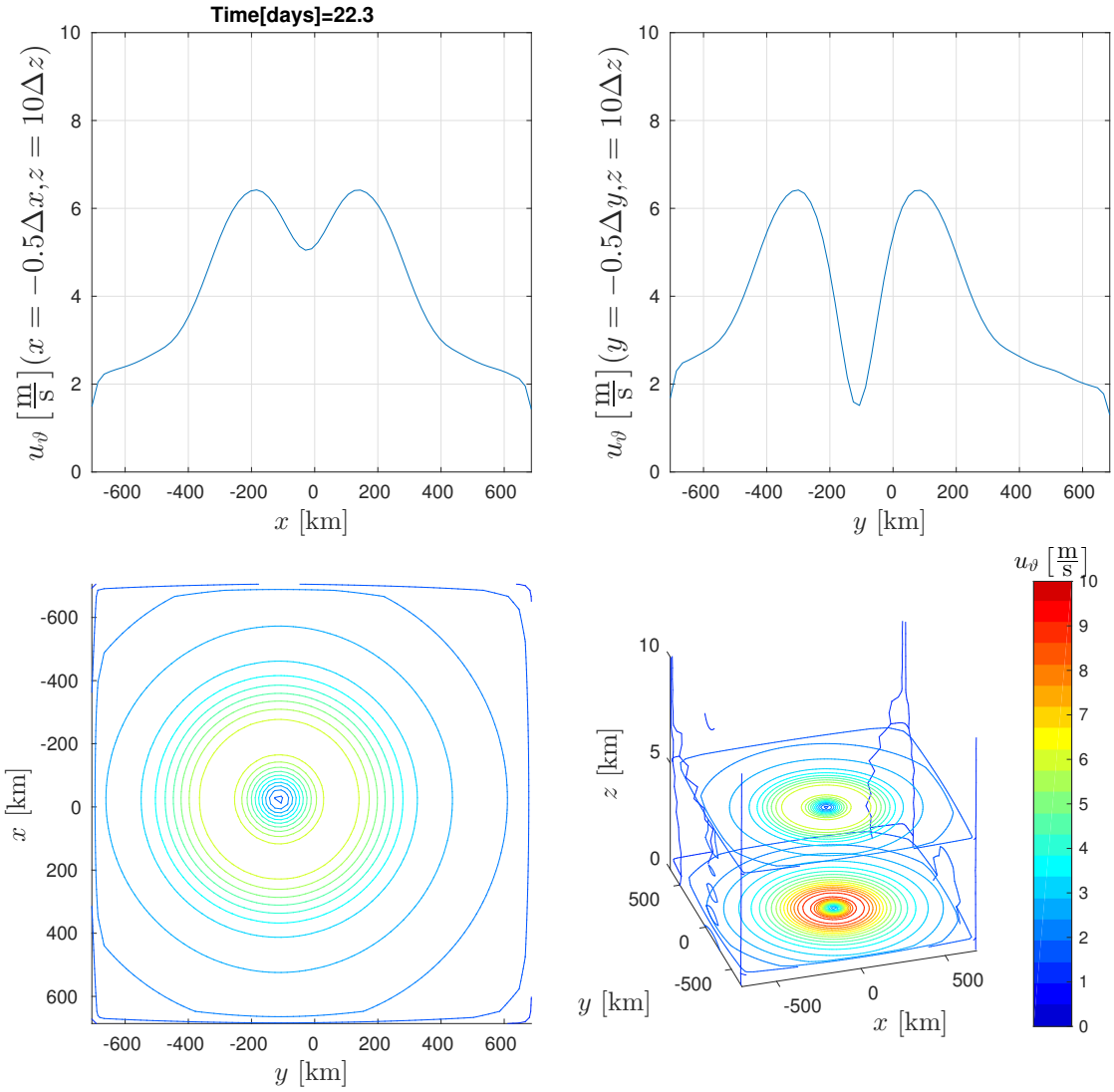

Fig. 5.10b.: Intensifying regime, azimuthal velocity long after impact. The highest value is found at zero altitude. The structure of two maxima corresponding to the radius of maximum wind is retained within the considered slices.

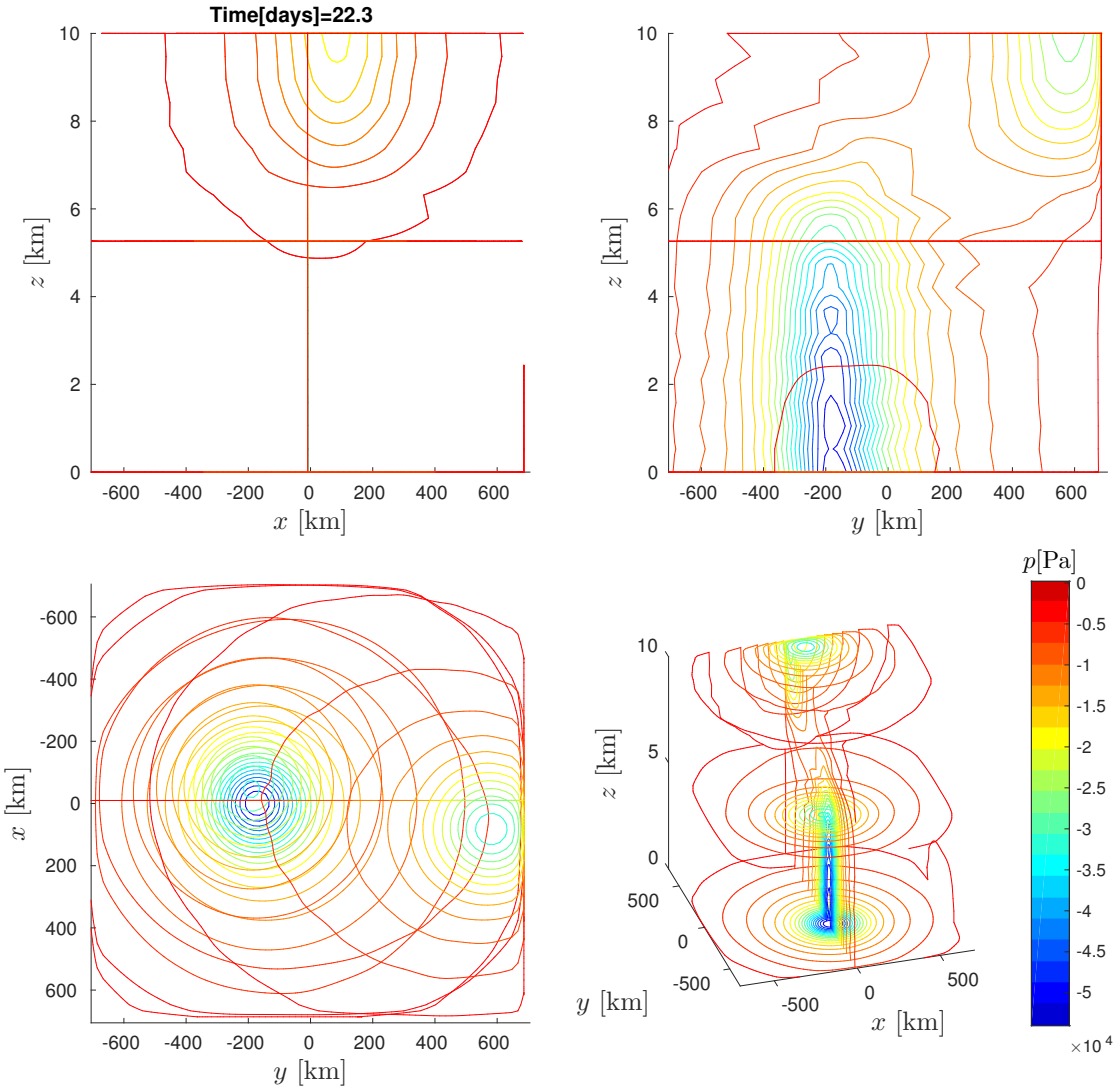

Fig. 5.10c.: Intensifying regime, pressure long after impact. The two vortices in lower and upper layer are clearly visible. The pressure drop in the top vortex is less severe than in the bottom one.

vortex. A first observation is that the case with $A = 160$km is covered well in the model under these circumstances (initial state cf. figures 5.1). There is no need for a smaller displacement in order to reduce vertical velocity and retain numerical stability. Figures 5.11 show centerline, azimuthal velocity and pressure field after 22.3 days. We also discover a cusp in the centerline and a splitting of the vortex, it takes place after around 4.3 days, but in this case our time splits do not contain the critical event as clearly. Compared to the recent case of a split vortex the resulting cell is stronger and the decrease in velocity at the vertical mid-level is not as severe. Also, the azimuthal velocity is not further decreasing in time, it seems to vary little around 8ms^{-1}. The displacement of the bottom vortex remains within 110km distance to the domain center, it is shown after 22.3 days. Despite the ongoing heating and the less vertical extent the tilt decreased further, the vortex straightened up and intensified, the maximum wind speed increased. The centerline plot 5.11a shows that instead motion takes place inside the central part of the domain.

5.5.2. Centerline evolution

Another instructive equation was derived by Paeschke *et al.* (2012) concerning the evolution of the centerline, their equation (6.2), a specific implication being the orthogonality of spatial and temporal differences (5.1.18). In leading order they find

$$\frac{\partial^2 \mathbf{X}^{(1)}}{\partial z^2} = \kappa\, \mathbf{n} + \mathcal{O}(\delta) \quad \text{and} \quad \boldsymbol{k} = \boldsymbol{\tau} + o(1) \tag{5.5.2}$$

with curvature κ, normal vector $\mathbf{n}$ and tangential vector $\boldsymbol{\tau}$. Therefore, the tilt is perpendicular to the terms involved in the differential equation for the centerline, and for a constant $\mathbf{X}_0$ it follows

$$\frac{\partial \mathbf{X}}{\partial t} \cdot \frac{\partial \mathbf{X}}{\partial z} = 0. \tag{5.5.3}$$

We add to the centerline plot another set of vectors denoting $\frac{\partial \mathbf{X}}{\partial t}$, also calculated with central differences. Moreover, we determine

$$\cos \angle \left(\frac{\partial \mathbf{X}}{\partial t}, \frac{\partial \mathbf{X}}{\partial z} \right) \tag{5.5.4}$$

to investigate the deviation from orthogonality. Figures 5.12 show the result for two cases that we already discussed, the neutral and the positive forcing. We indeed observe that for almost all time steps the difference to a right angle stays below 2%.

5.5.3. Future work

It is worthwhile to collect more data in order to observe specific events such as the splitting of a vortex under strong shear. Also, the transition phase could be resolved higher. This case in particular would benefit from higher vertical resolution. This however restricts the time step and we need more computing resources to cover the same range of system time.

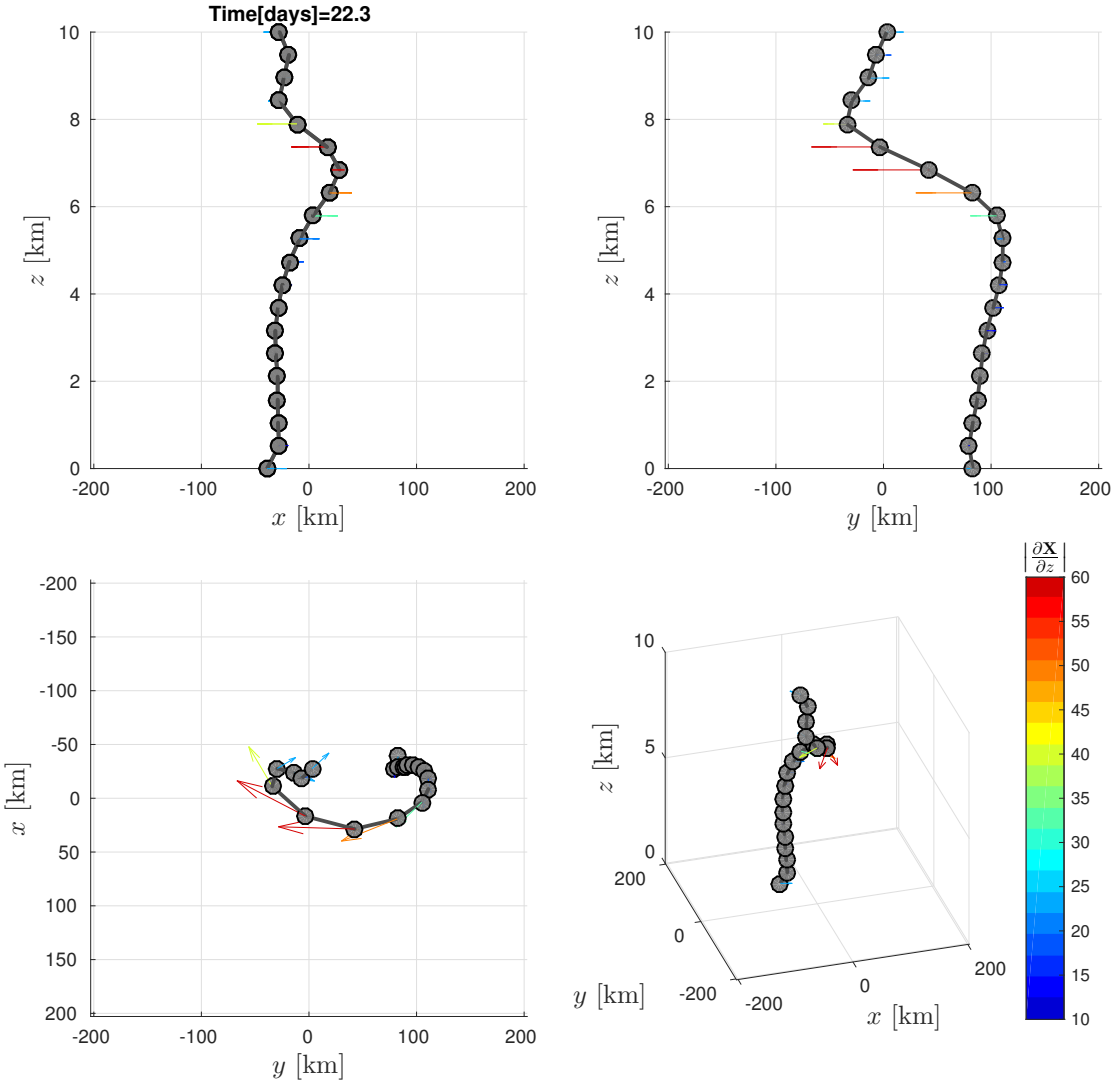

Fig. 5.11a.: Vortex centerline after 22.3 days. Concentrated heating on the inner 200km for an initial displacement of $A = 160$km. Note the cusp of the centerline above 6km.

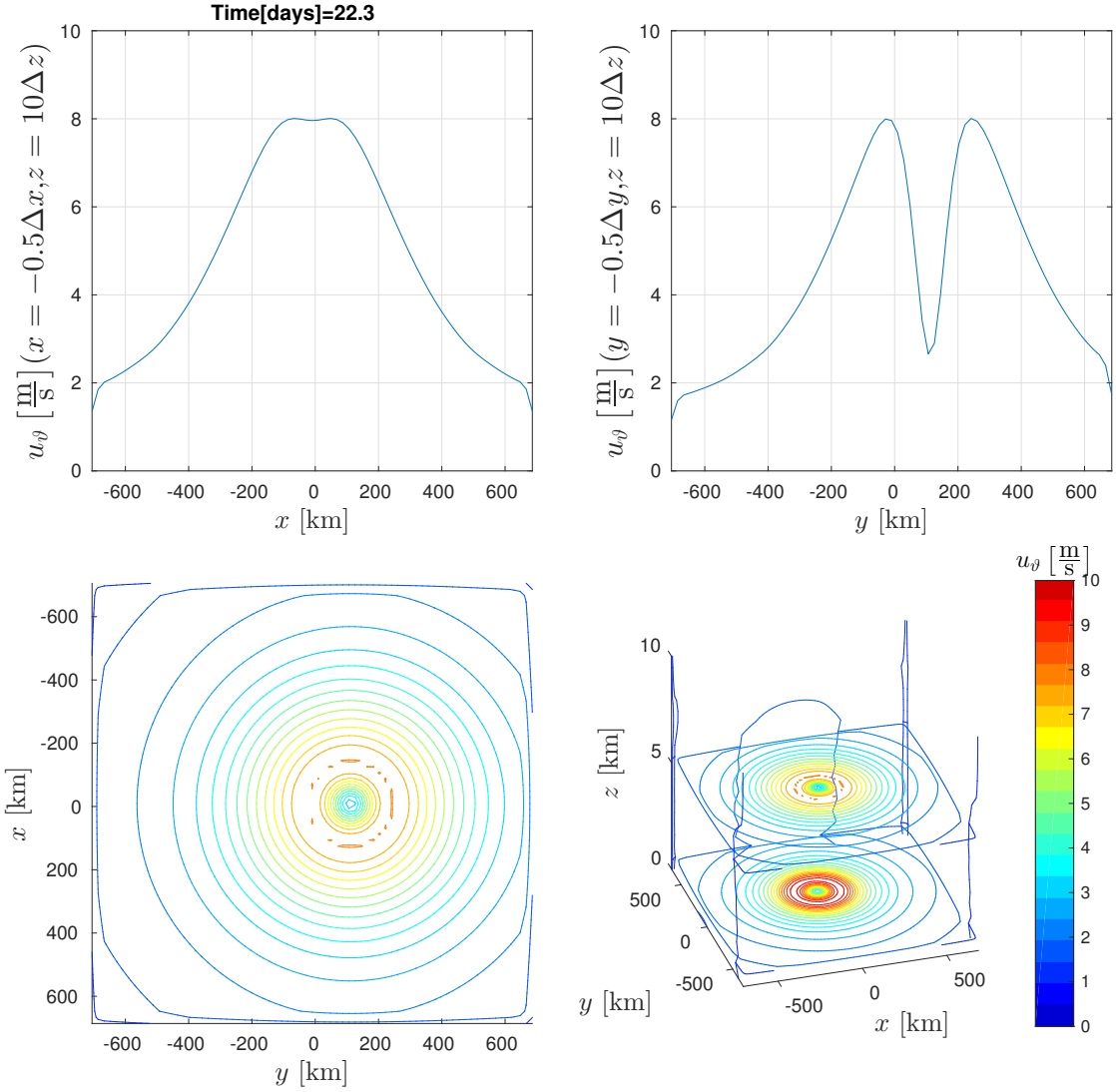

Fig. 5.11b.: Azimuthal velocity after 22.3 days. Concentrated heating on the inner 200km for an initial displacement $A = 160$km.

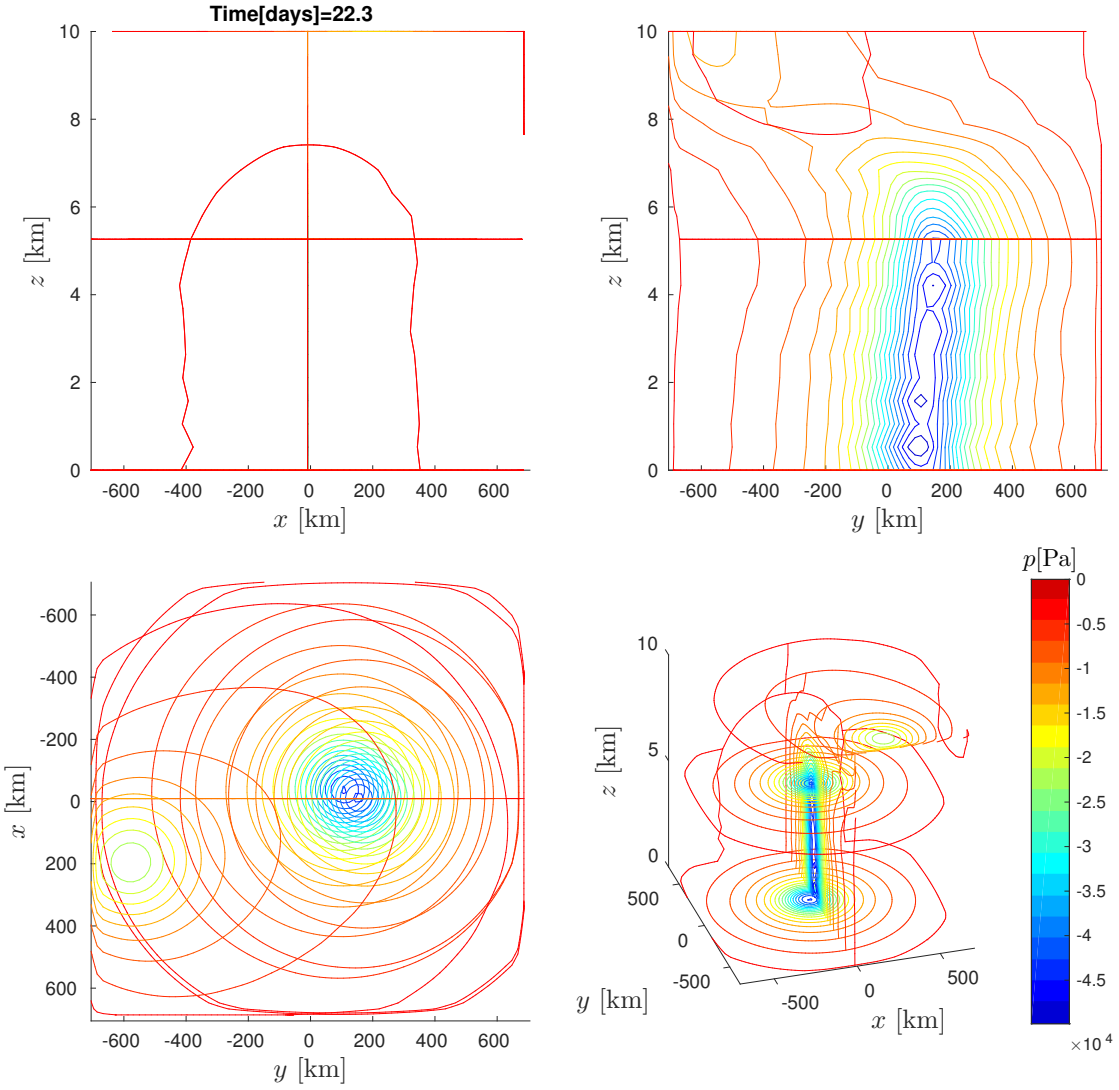

Fig. 5.11c.: Pressure profile after 22.3 days. Concentrated heating on the inner 200km for an initial displacement $A = 160$km.

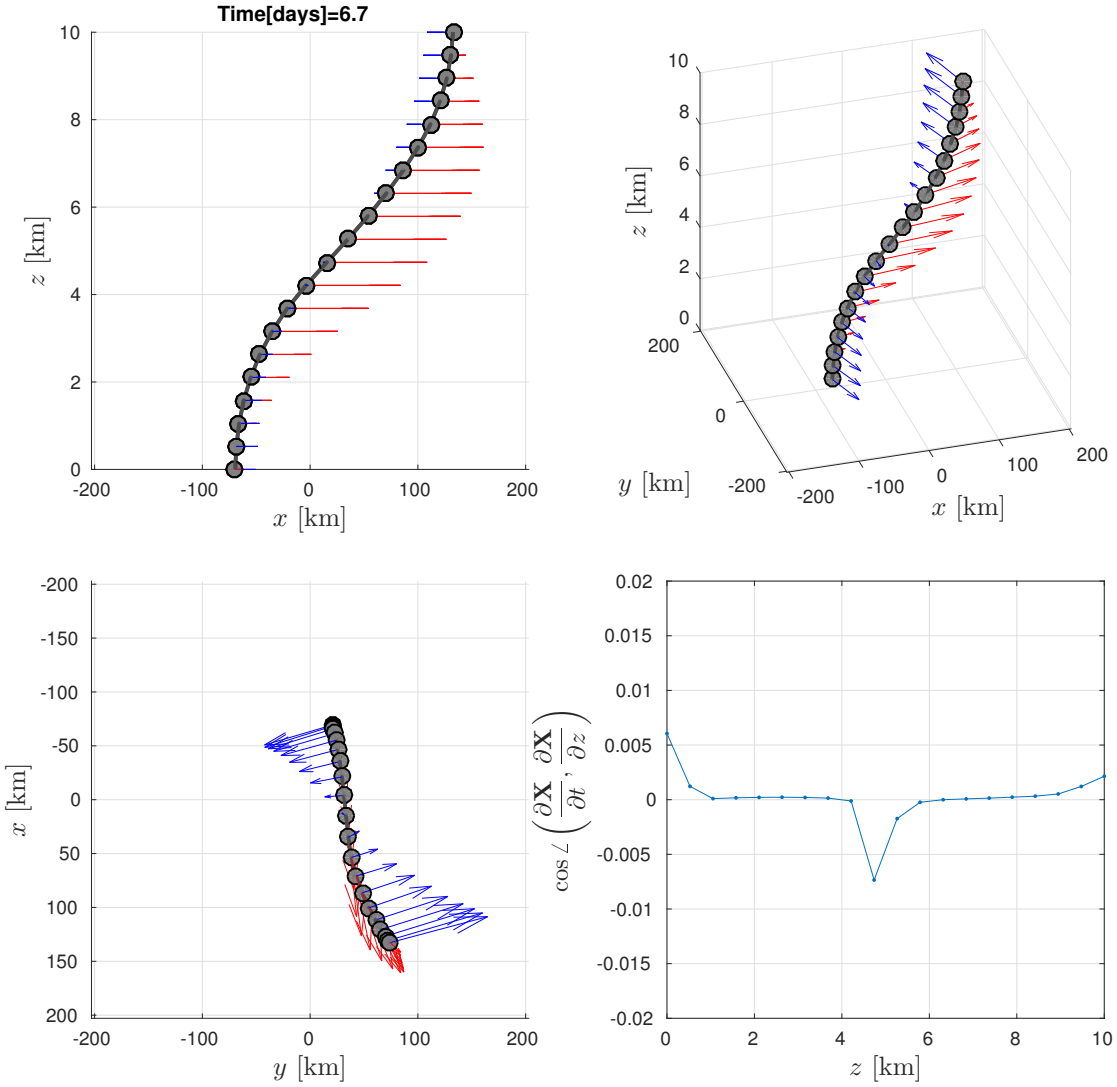

Fig. 5.12a.: Neutral forcing on the vortex, initial displacement of 160km. Red vectors represent $\frac{\partial \mathbf{X}}{\partial z}$ and blue vectors stand for $\frac{\partial \mathbf{X}}{\partial t}$. The plot in the lower right corner highlights the angle between those two vectors in each vertical level.

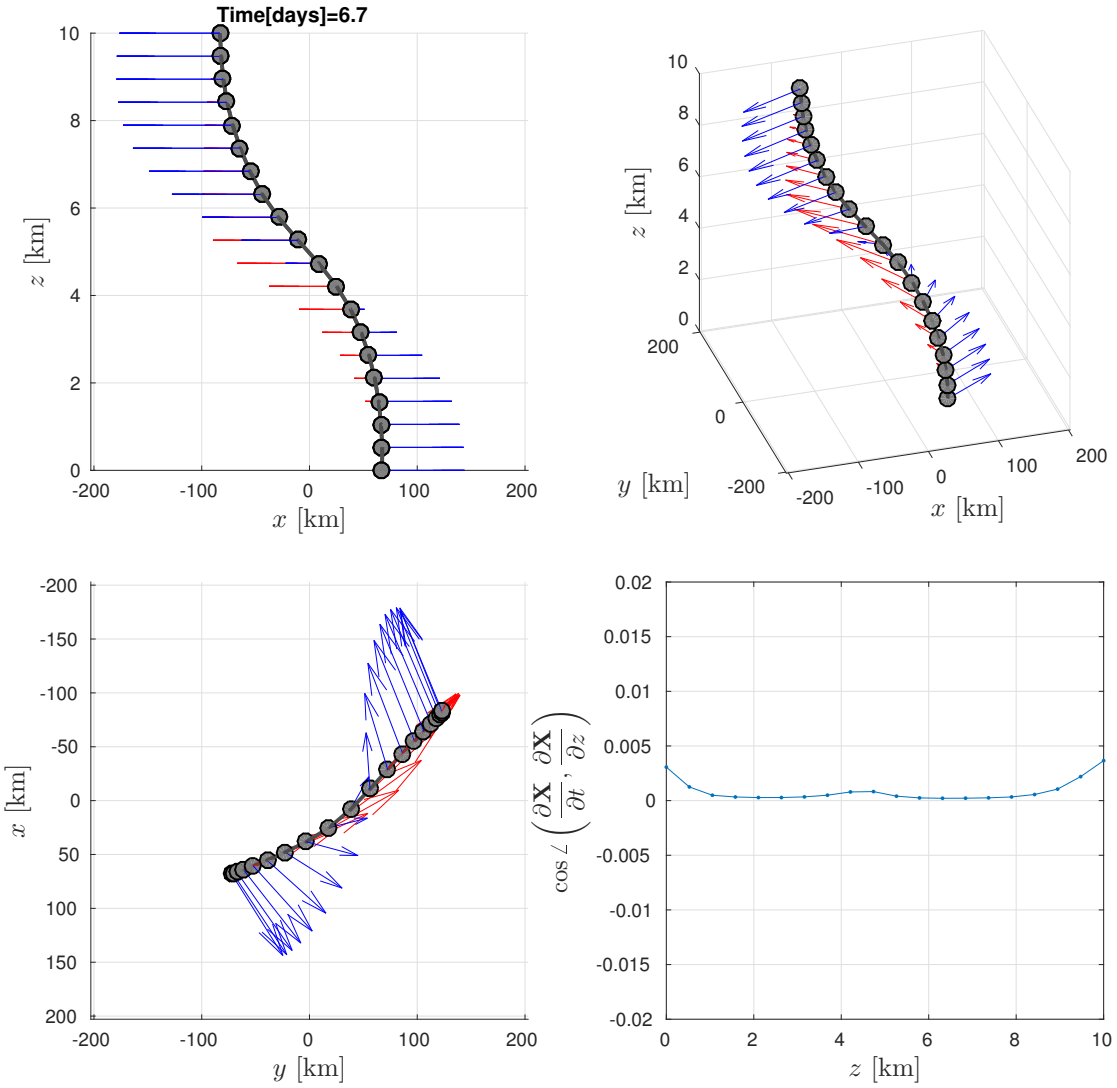

Fig. 5.12b.: Positive forcing on the vortex with an initial displacement of 80km. Tilt (red) and centerline evolution (blue) are denoted by vectors and their angle is determined (lower right corner).

Another concrete example is the local driving of a vortex that finally lead to two vortices as well. One could implement a strong and smooth decay away from the central part of the vortex and only impose a Gaussian further away from it. Under certain circumstances this could prevent the vortex splitting.

Besides the numerical experiments presented here many more options could be tested concerning domain setup, initialization of the vortex, data extracting routines just to name a few. A particularly interesting aspect is the extension to moist processes that play a crucial role in the dynamics of tropical cyclones. A tailored asymptotic analysis needs to be conducted along the lines of the work by Paeschke *et al.* (2012), numerical experiments could complement the findings.

5.6. Conclusion

A thorough parameter study was conducted and supports the findings of Paeschke *et al.* (2012) concerning the Eigenmode of precession and the influence of diabatic heating patterns on vortex core structure. A TC-like vortex embedded in a zero far-field environment is considered and displaced initially, aligning subsequently. If the centerline vertically attains a cosine shape it will persist up to small fluctuations, while a linear curve is deformed quickly. Paeschke *et al.* (2012) proposed an Eigenmode of the centerline that is a linear function of cosine. Moreover, our numerical experiments support that the heating follows the same principle for each of the three different regimes: vortex conservation, attenuation and intensification. Only the orientation of the asymmetric diabatic source decides on the respective case. For the centerline we recover orthogonality of temporal and spatial derivative to a large extent.

During the vortex amplification we observed that at some point the vortex cannot sustain the vertical shear and splits. The event is characterized by extra up- and downdrafts, a decrease of azimuthal velocity at the bottom and a short pressure increase in the top layer close to the boundary. In the aftermath the centerline would need to be pictured in two separate parts, highlighting that now we face two vortices. They remain separate and both retain the precession resulting from the initial tilt, the overall setup stabilizes and the maximum wind speed is not increasing further. Since the tilt is reduced significantly in the proccess for both remaining vortices the influence of the heating is also diminished.

In case of locally strong driving we observe a similar behavior, however leading to a stronger and slightly taller vortex in the lower layer, the cut in vertical altitude is best seen in the vertical pressure profile. The motion range of the centerline is also slightly smaller.

Storm splitting under environmental vertical shear typically leads to counterrotating and countermoving vortices (Holton, 2004). However, we do not impose a constant background wind shear but instead shear the vortex initially. Therefore, we do not expect such a development, and the similarly built vortices in top and lower layer are reasonable.

A. Supplemental material

A.1. Numerical setup

We present here the profiles of velocity, pressure and potential temperature at different times for an adiabatic vortex. The initial displacement is $A = 160$km with α_c.

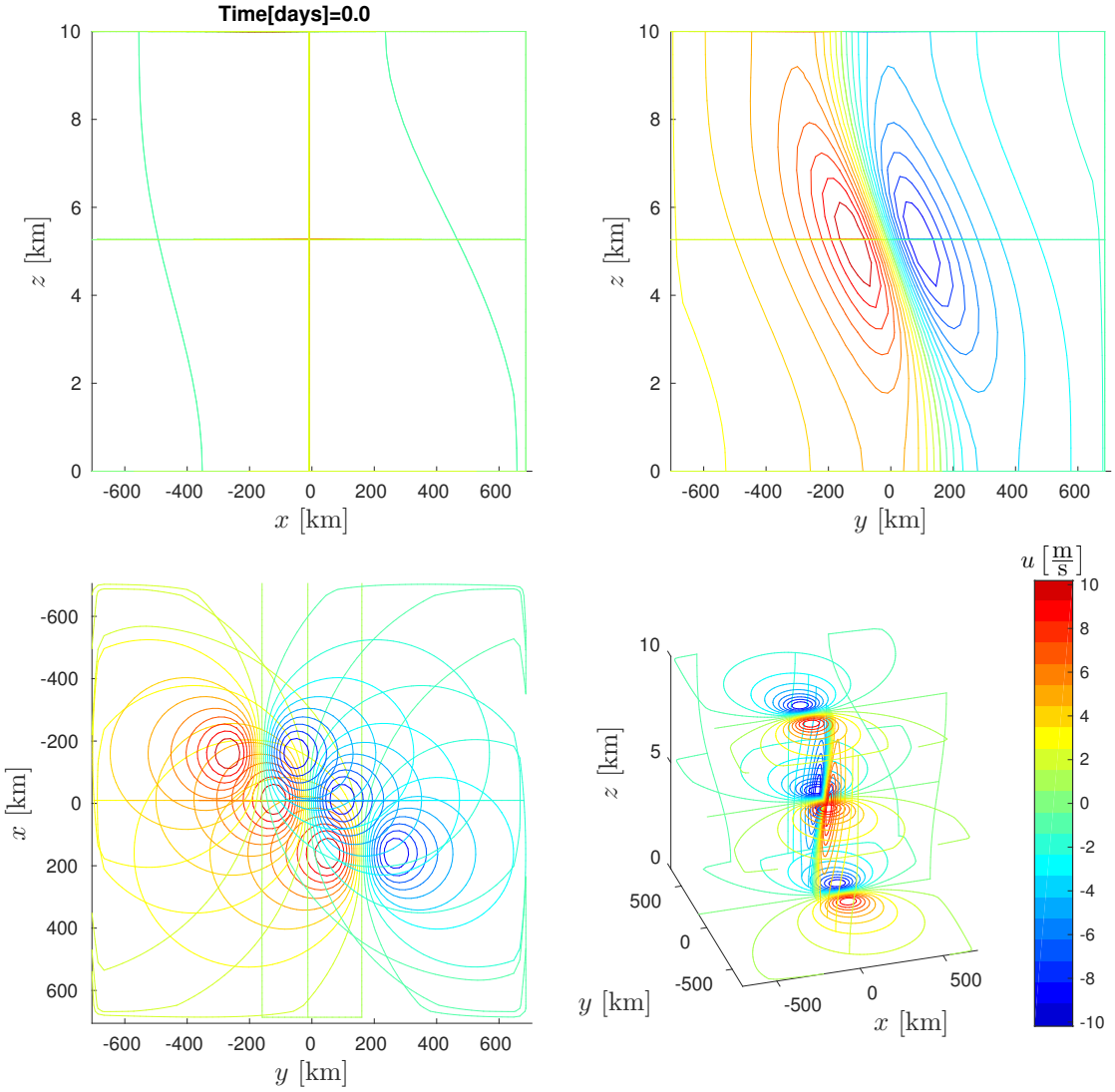

Fig. A.1.: Initial horizontal velocity u.

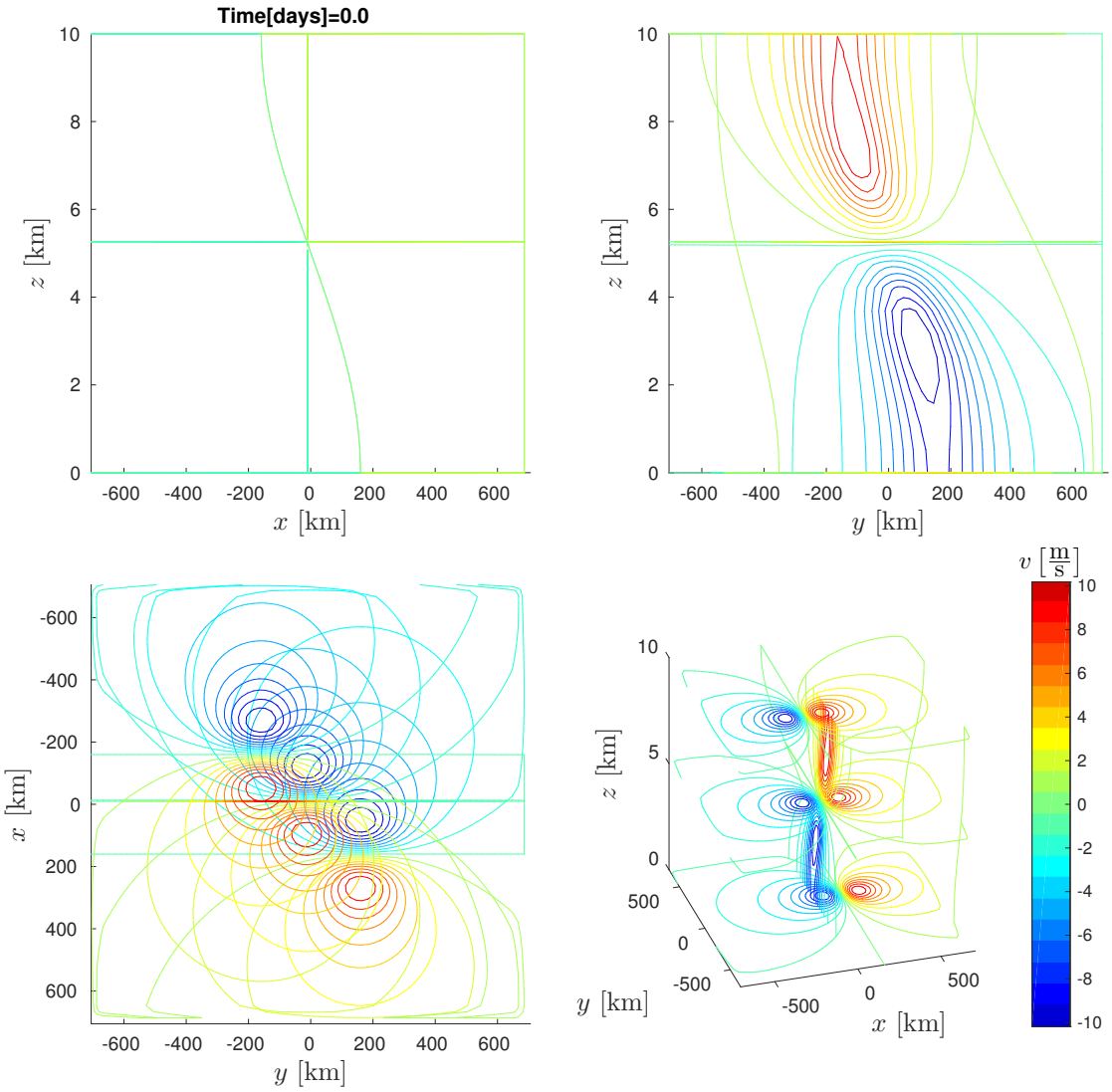

Fig. A.2.: Initial horizontal velocity v.

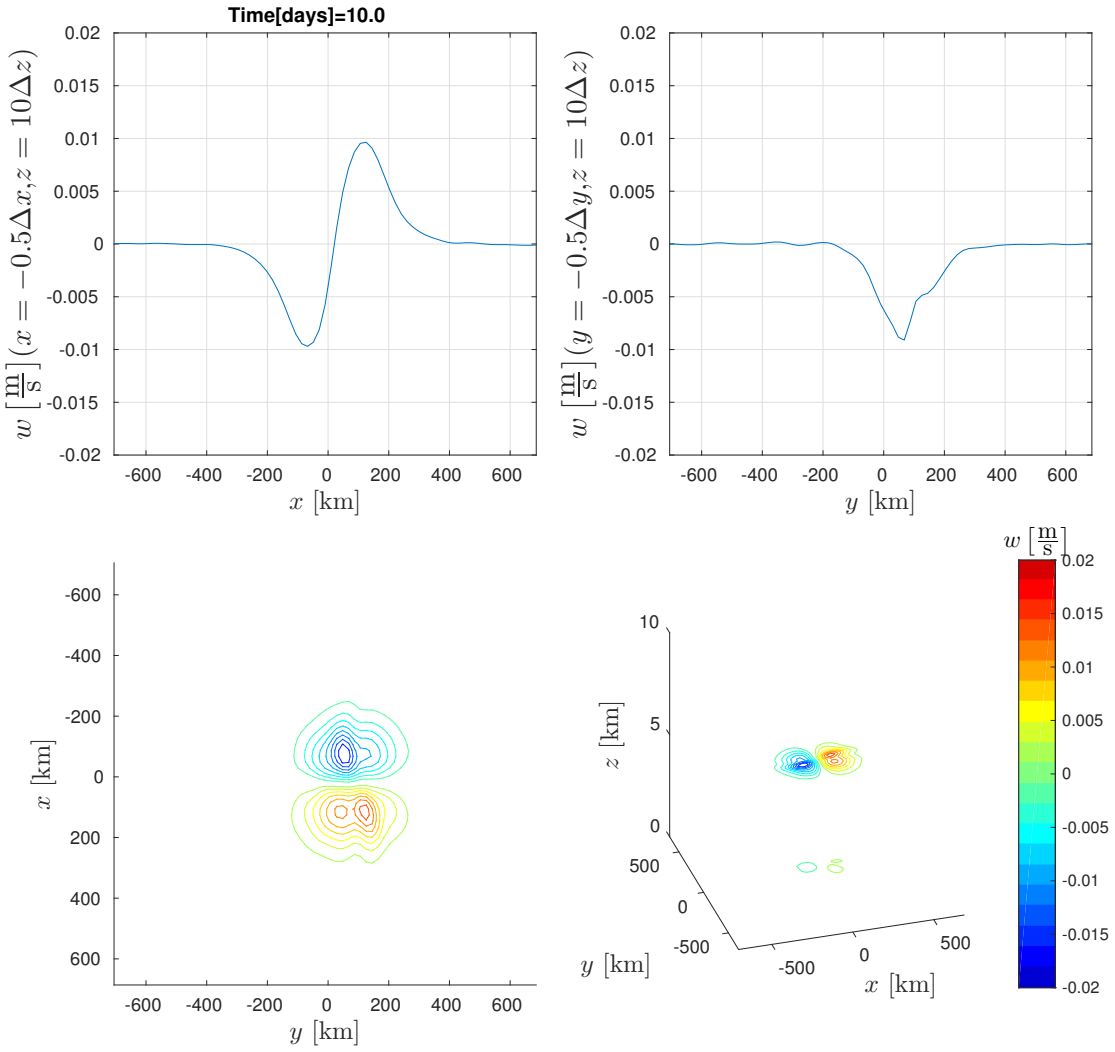

Fig. A.3.: Vertical velocity w after 10 days.

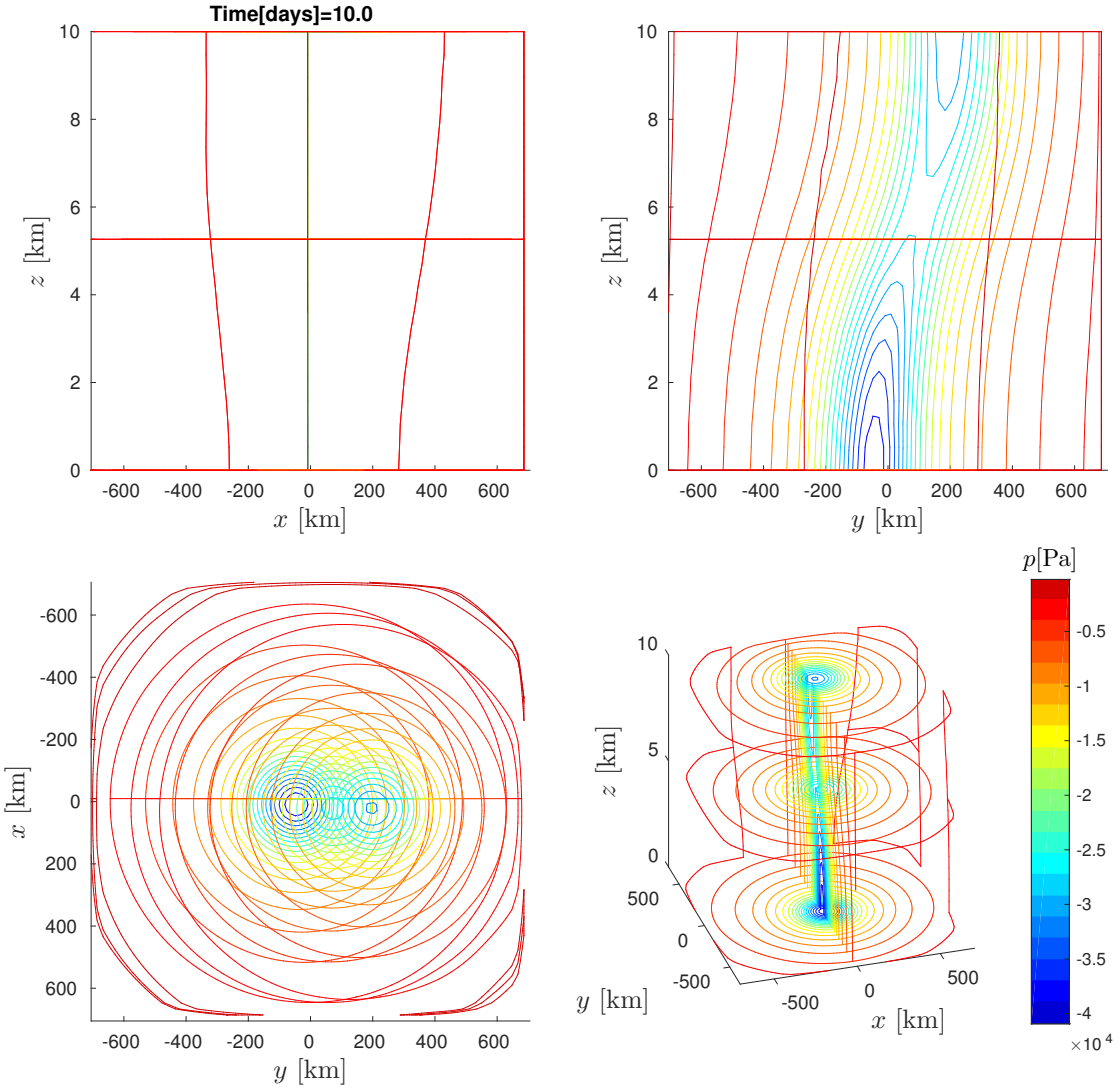

Fig. A.4.: Pressure p after 10 days.

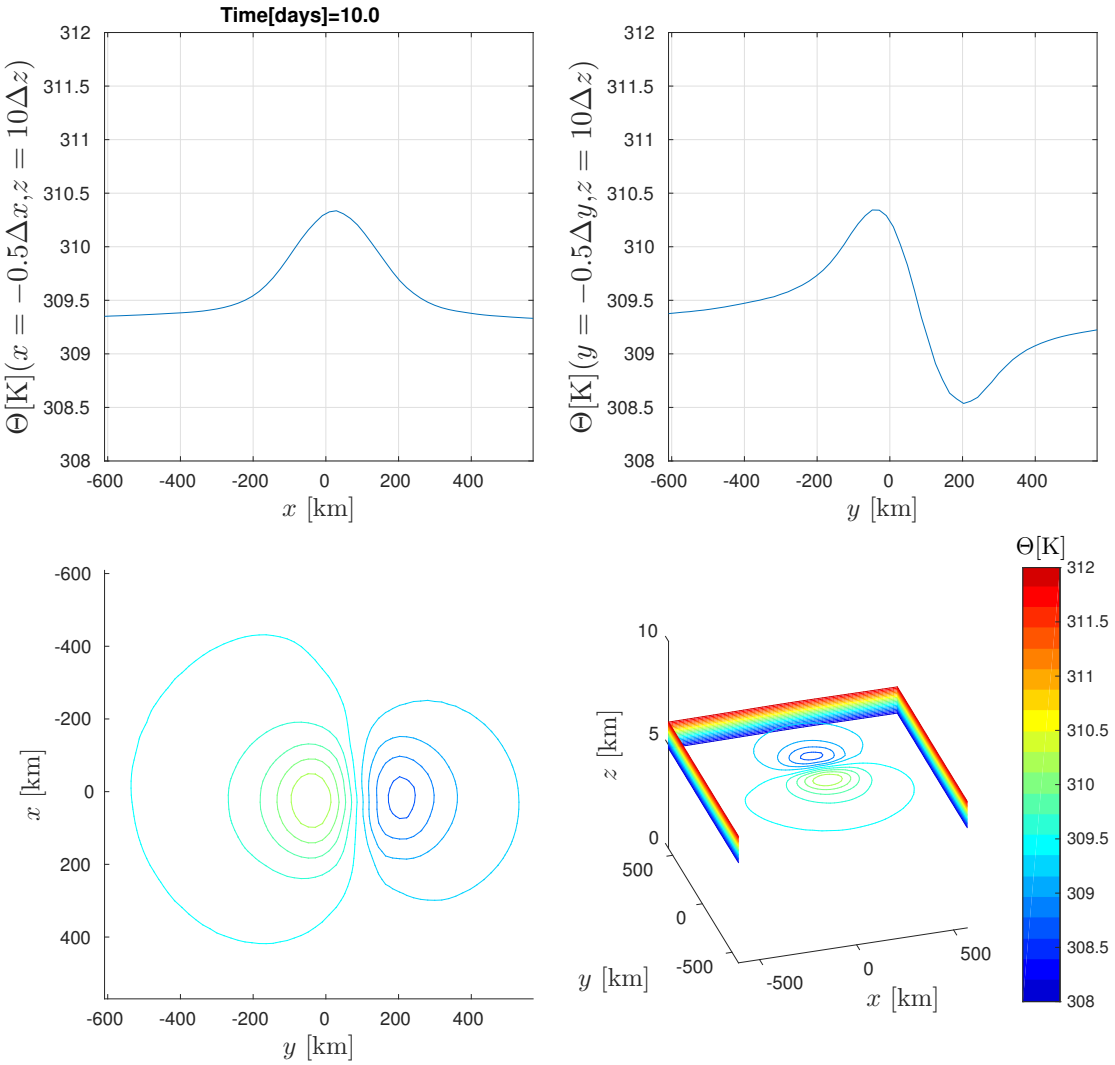

Fig. A.5.: Potential temperature Θ after 10 days.

A.2. Extremely weakening regime

In part 5.4.2 we discussed the weakening regime with a ten times higher forcing. At this point we show that not only the tilt has almost vanished but also has the vertical velocity (A.6a) and the heating (A.6b).

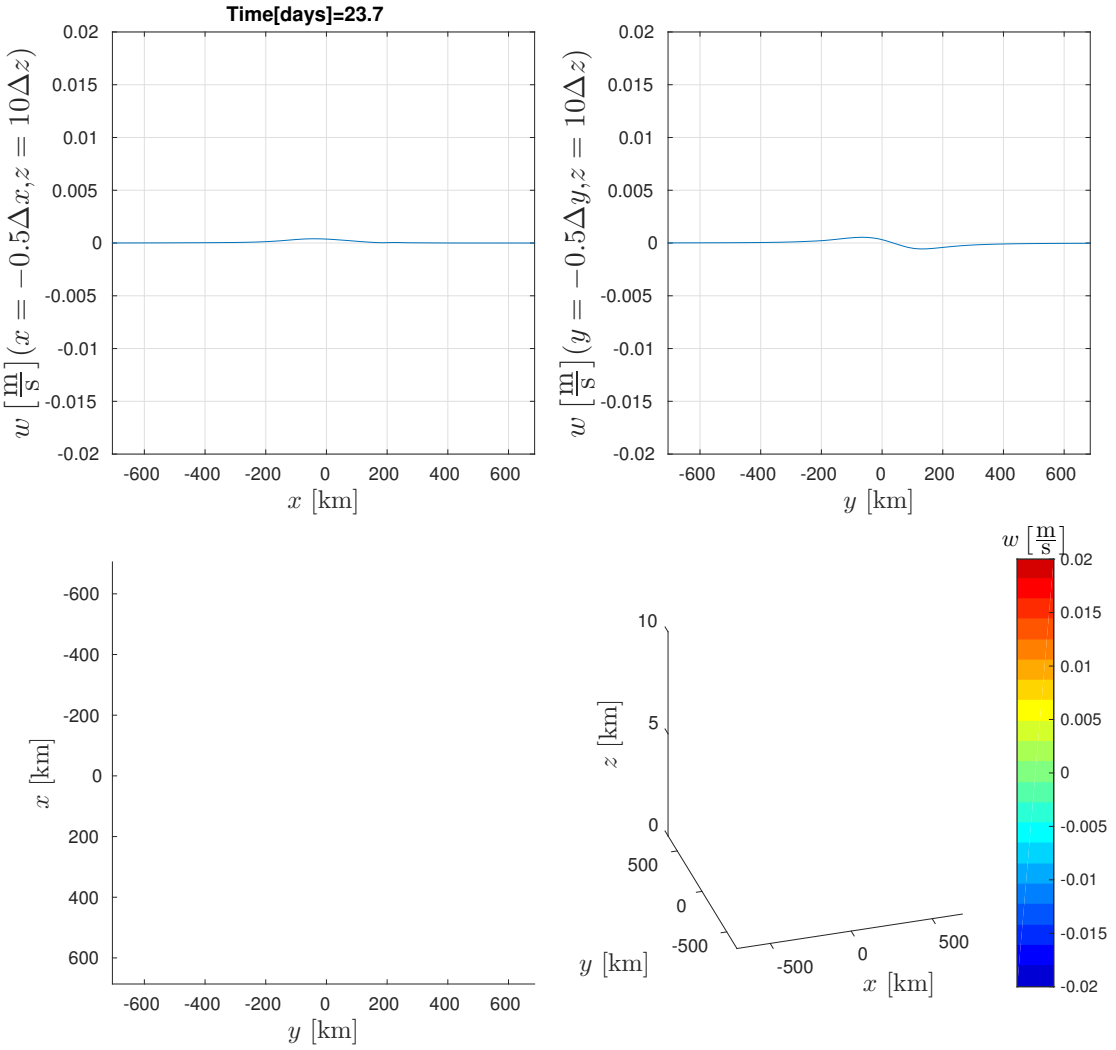

Fig. A.6a.: Vertical velocity for extremely weakened vortex after 23.7 days. The velocity is too small to reach any of the fixed contour line values inside the range.

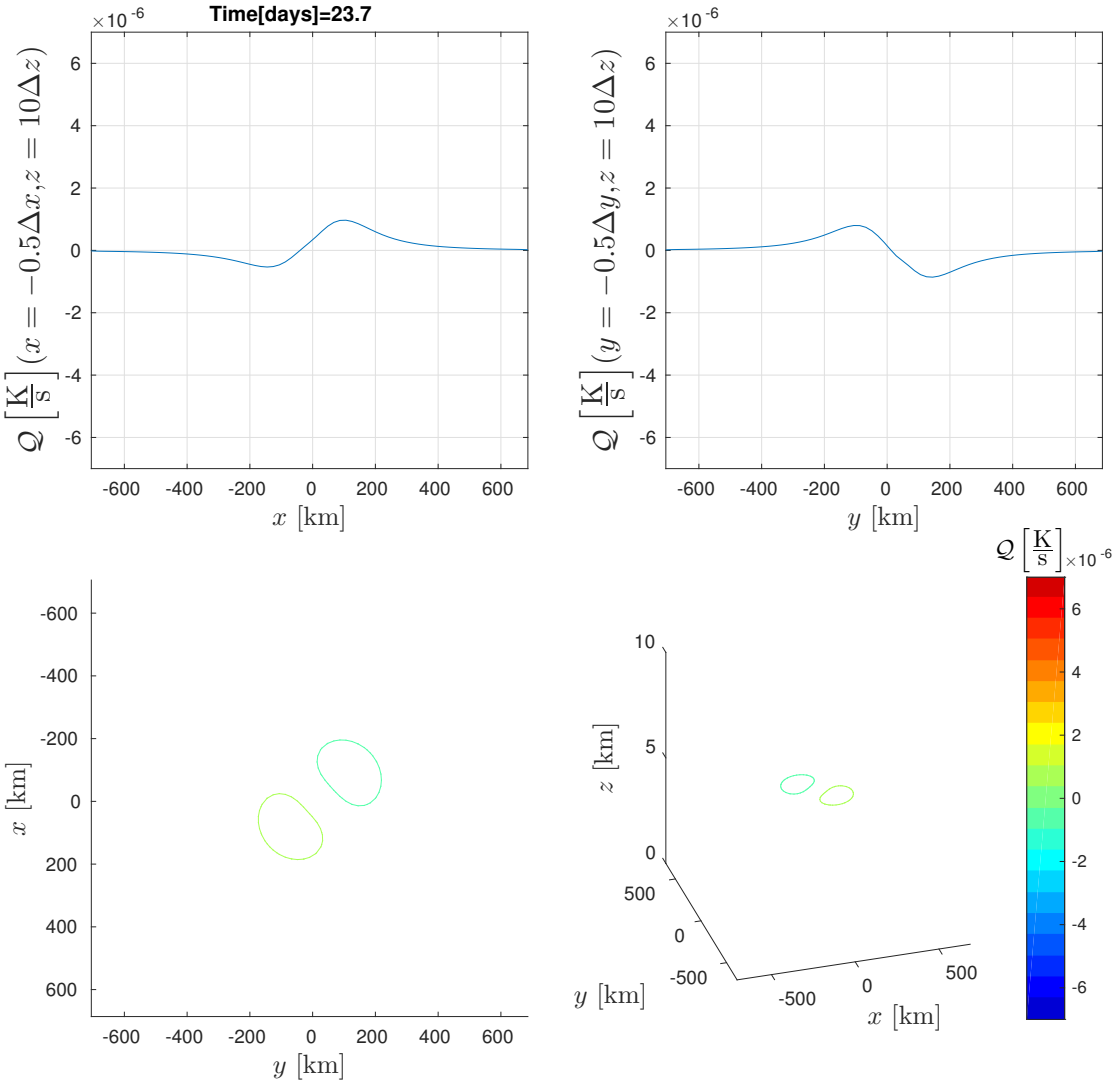

Fig. A.6b.: Diabatic source term for extremely weakened vortex after 23.7 days.

A.3. Initial centerline and azimuthal velocity for $A = 80\text{km}$

The setup is slightly changed for a maximum displacement of 80km for a single centerline vertex and shown in figures A.7.

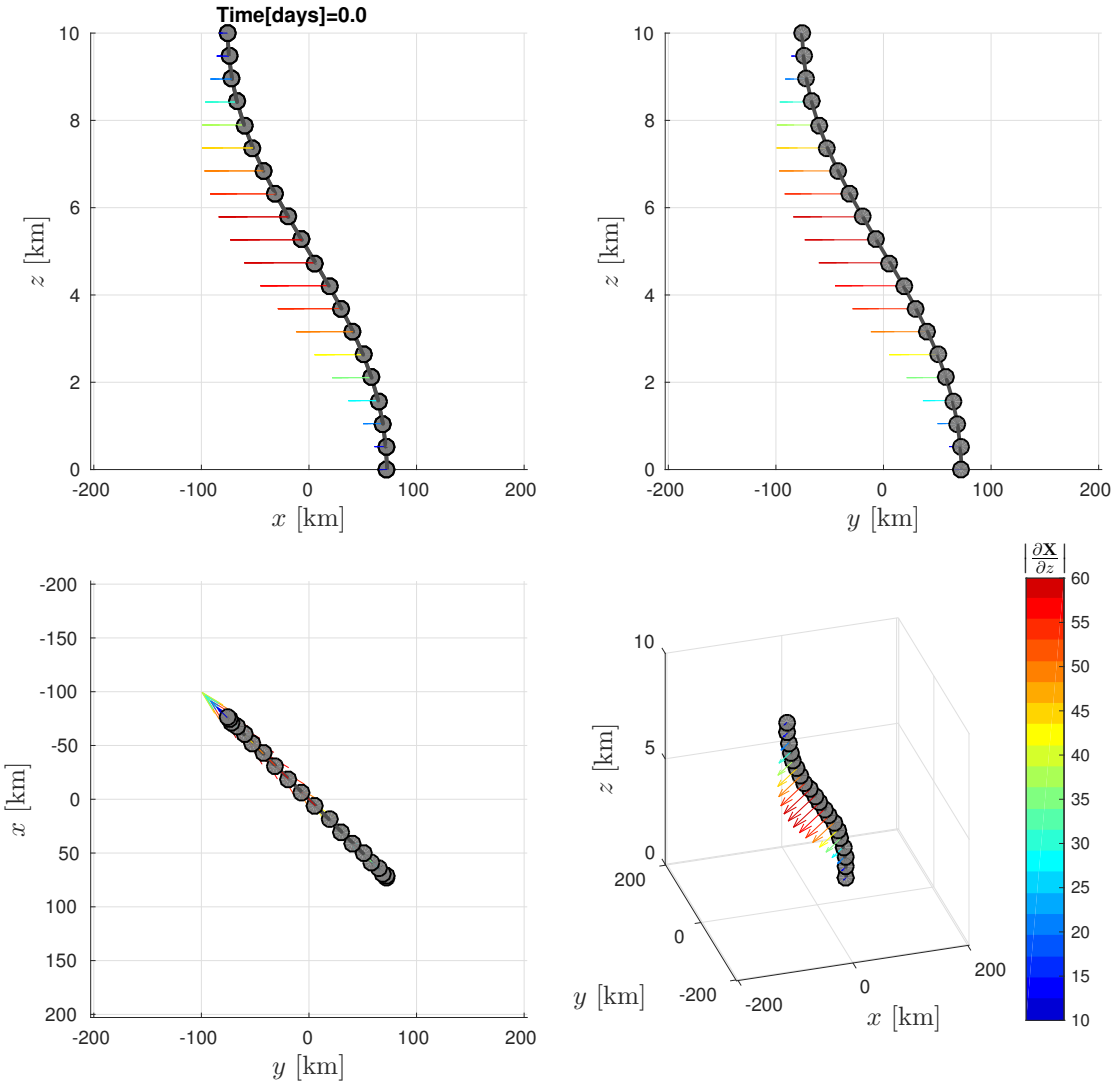

Fig. A.7a.: Initial vortex centerline for $A = 80\text{km}$, considered only for positive forcing on the whole domain.

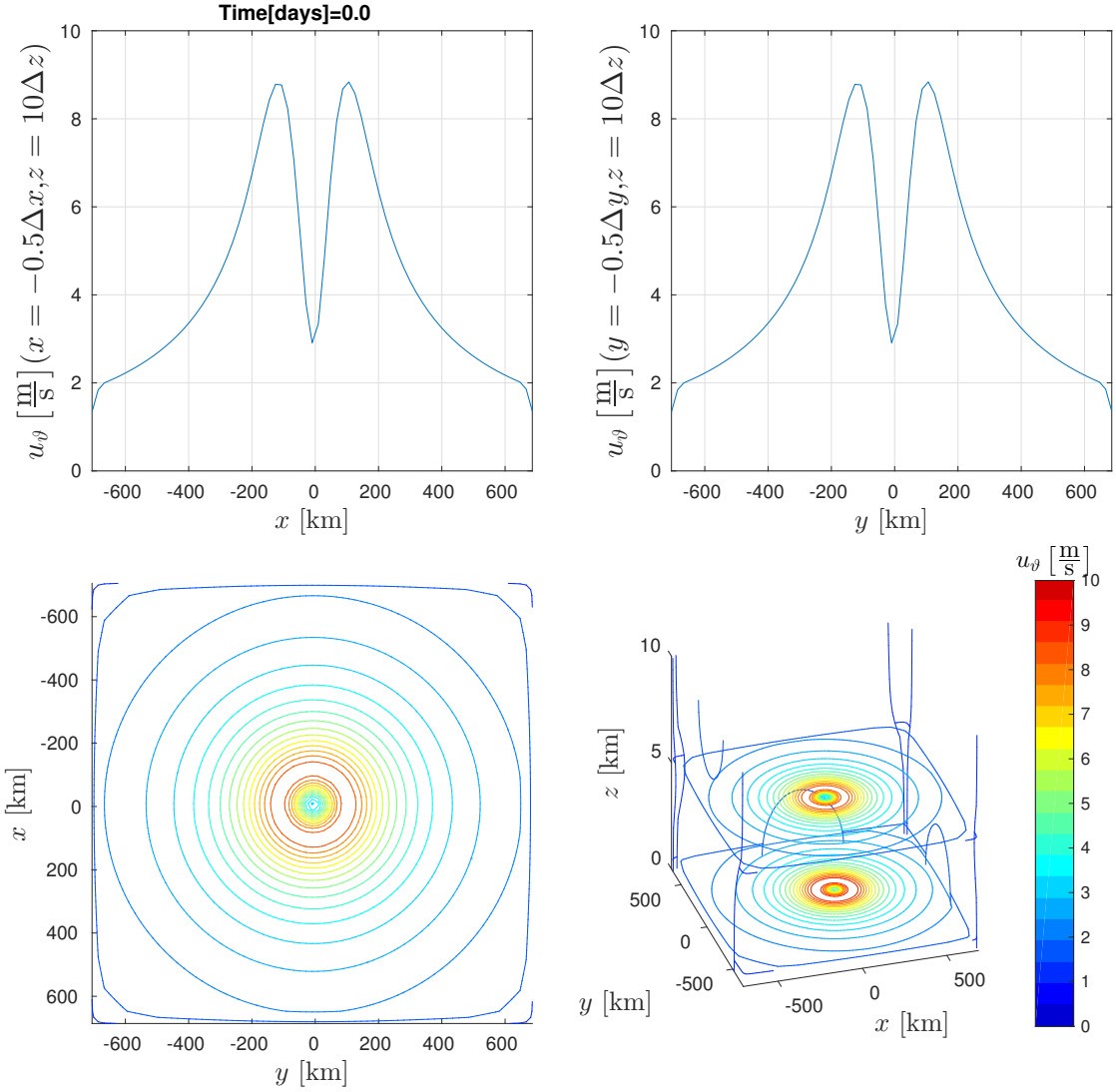

Fig. A.7b.: Initial azimuthal velocity for $A = 80$km, considered only for positive forcing on the whole domain.

References

Charbonneau, Paul & Smolarkiewicz, Piotr K. 2013 Modeling the Solar Dynamo. *Science* **340** (6128), 42–43.

Clark, Terry L. 1977 A small-scale dynamic model using a terrain-following coordinate transformation. *Journal of Computational Physics* **24** (2), 186–215.

Clark, Terry L. & Farley, R. D. 1984 Severe Downslope Windstorm Calculations in Two and Three Spatial Dimensions Using Anelastic Interactive Grid Nesting: A Possible Mechanism for Gustiness. *Journal of the Atmospheric Sciences* **41** (3), 329–350.

Dunkerton, Timothy J., Montgomery, M. T. & Wang, Z. 2009 Tropical cyclogenesis in a tropical wave critical layer: Easterly waves. *Atmospheric Chemistry & Physics* **9** (15).

Durran, Dale R. 1989 Improving the Anelastic Approximation. *Journal of the Atmospheric Sciences* **46** (11), 1453–1461.

Durran, Dale R. 2008 A physically motivated approach for filtering acoustic waves from the equations governing compressible stratified flow. *Journal of Fluid Mechanics* **601**.

Durran, Dale R. 2010 *Numerical methods for fluid dynamics: With applications to geophysics*, , vol. 32. Springer.

Frank, William & Ritchie, Elizabeth 1999 Effects of environmental flow upon tropical cyclone structure. *Monthly weather review* **127** (9).

Holton, James R. 2004 *An introduction to dynamic meteorology*, 4th edn. Burlington, MA: Elsevier Academic Press.

Israeli, Moshe & Orszag, Steven A. 1981 Approximation of radiation boundary conditions. *Journal of Computational Physics* **41** (1), 115–135.

Jones, Sarah C. 1995 The evolution of vortices in vertical shear. I: Initially barotropic vortices. *Quarterly Journal of the Royal Meteorological Society* **121** (524), 821–851.

Kadioglu, Samet Y., Klein, Rupert & Minion, Michael L. 2008 A fourth-order auxiliary variable projection method for zero-Mach number gas dynamics. *Journal of Computational Physics* **227** (3), 2012–2043.

Klein, R. 2008 An unified approach to meteorological modelling based on multiple-scales asymptotics. *Advances in Geosciences* **15**, 23–33.

Klein, Rupert 2009 Asymptotics, structure, and integration of sound-proof atmospheric flow equations. *Theoretical and Computational Fluid Dynamics* **23** (3), 161–195.

Klein, Rupert 2010 Scale-Dependent Models for Atmospheric Flows. *Annual Review of Fluid Mechanics* **42** (1), 249–274.

Klein, Rupert, Achatz, Ulrich, Bresch, Didier, Knio, Omar M. & Smolarkiewicz, Piotr K. 2010 Regime of Validity of Soundproof Atmospheric Flow Models. *Journal of the Atmospheric Sciences* **67** (10), 3226–3237.

Klein, Rupert & Vater, Stefan 2003 *Mathematische Modellierung in der Klimaforschung*. Fachbereich Mathematik und Informatik: Freie Universität Berlin.

Klemp, J. B. & Lilly, D. K. 1978 Numerical Simulation of Hydrostatic Mountain Waves. *Journal of the Atmospheric Sciences* **35** (1), 78–107.

Kundu, P. K. & Cohen, I. M. 2002 *Fluid Mechanics*, 2nd edn. Academic Press.

Lipps, Franik B. & Hemler, Richard S. 1982 A Scale Analysis of Deep Moist Convection and Some Related Numerical Calculations. *Journal of the Atmospheric Sciences* **39** (10), 2192–2210.

Nolting, Wolfgang 2014 *Grundkurs Theoretische Physik 6*. Berlin, Heidelberg: Springer Berlin Heidelberg.

Paeschke, Eileen, Marschalik, Patrik, Owinoh, Antony Z. & Klein, Rupert 2012 Motion and structure of atmospheric mesoscale baroclinic vortices: dry air and weak environmental shear. *Journal of Fluid Mechanics* **701**, 137–170.

Pedlosky, Joseph 1987 *Geophysical Fluid Dynamics*, 2nd edn. Springer.

Prusa, Joseph M. & Smolarkiewicz, Piotr K. 2003 An all-scale anelastic model for geophysical flows: dynamic grid deformation. *Journal of Computational Physics* **190** (2), 601–622.

Prusa, Joseph M., Smolarkiewicz, Piotr K. & Wyszogrodzki, Andrzej A. 2008 EULAG, a computational model for multiscale flows. *Computers & Fluids* **37** (9), 1193–1207.

Reasor, Paul D. & Montgomery, Michael T. 2001 Three-dimensional alignment and corotation of weak, TC-like vortices via linear vortex Rossby waves. *Journal of the Atmospheric Sciences* **58** (16), 2306–2330.

Reasor, Paul D. & Montgomery, Michael T. 2015 Evaluation of a Heuristic Model for Tropical Cyclone Resilience. *Journal of the Atmospheric Sciences* **72** (5), 1765–1782.

Reasor, Paul D., Montgomery, Michael T. & Grasso, Lewis D. 2004 A New Look at the Problem of Tropical Cyclones in Vertical Shear Flow: Vortex Resiliency. *Journal of the Atmospheric Sciences* **61** (1), 3–22.

Rosa, Bogdan, Kurowski, Marcin J. & Ziemiański, Michał Z. 2011 Testing the anelastic nonhydrostatic model EULAG as a prospective dynamical core of a numerical weather prediction model Part I: Dry benchmarks. *Acta Geophysica* **59** (6), 1236–1266.

Schielicke, Lisa, Névir, Peter & Ulbrich, Uwe 2016 Kinematic vorticity number - A tool for estimating vortex sizes and circulations. *Tellus, Series A: Dynamic Meteorology and Oceanography* **68** (0).

Shapiro, Lloyd J. & Montgomery, Michael T. 1993 A Three-Dimensional Balance Theory for Rapidly Rotating Vortices. *Journal of the Atmospheric Sciences* **50** (19), 3322–3335.

Smolarkiewicz, PK & Margolin, LG 1994 Variational solver for elliptic problems in atmospheric flows. *Appl. Math. Comp. Sci* **4** (4), 527–551.

Smolarkiewicz, Piotr K 1984 A fully multidimensional positive definite advection transport algorithm with small implicit diffusion. *Journal of Computational Physics* **54** (2), 325–362.

Smolarkiewicz, Piotr K. 1991 On Forward-in-Time Differencing for Fluids. *Monthly Weather Review* **119** (10), 2505–2510.

Smolarkiewicz, Piotr K. 2006 Multidimensional positive definite advection transport algorithm: an overview. *International journal for numerical methods in fluids* **50** (10), 1123–1144.

Smolarkiewicz, Piotr K. & Clark, Terry L. 1986 The multidimensional positive definite advection transport algorithm: further development and applications. *Journal of Computational Physics* **67** (2), 396–438.

Smolarkiewicz, Piotr K. & Dörnbrack, Andreas 2008 Conservative integrals of adiabatic Durran's equations. *International Journal for Numerical Methods in Fluids* **56** (8), 1513–1519.

Smolarkiewicz, Piotr K. & Grabowski, Wojciech W. 1990 The multidimensional positive definite advection transport algorithm: Nonoscillatory option. *Journal of Computational Physics* **86** (2), 355–375.

Smolarkiewicz, Piotr K. & Margolin, Len G. 1997 On Forward-in-Time Differencing for Fluids: an Eulerian/Semi-Lagrangian Non-Hydrostatic Model for Stratified Flows. *Atmosphere-Ocean* **35** (sup1), 127–152.

Smolarkiewicz, Piotr K. & Margolin, Len G. 1998 MPDATA: A Finite-Difference Solver for Geophysical Flows. *Journal of Computational Physics* **140** (2), 459–480.

Smolarkiewicz, Piotr K., Margolin, Len G. & Wyszogrodzki, Andrzej A. 2001 A class of nonhydrostatic global models. *Journal of the atmospheric sciences* **58** (4), 349–364.

Smolarkiewicz, Piotr K. & Margolin, Len O. 1993 On Forward-in-Time Differencing for Fluids: Extension to a Curvilinear Framework. *Monthly Weather Review* **121** (6), 1847–1859.

Smolarkiewicz, Piotr K. & Szmelter, Joanna 2005 MPDATA: An edge-based unstructured-grid formulation. *Journal of Computational Physics* **206** (2), 624–649.

Smolarkiewicz, P K, Temperton, C, Thomas, S J & Wyszogrodzki, A A 2004 Spectral preconditioners for nonhydrostratic atmospheric models: extreme applications. In *Seminar on Recent developments in numerical methods for atmospheric and ocean modelling, 6-10 September 2004*, pp. 203–221. ECMWF, Shinfield Park, Reading: ECMWF.

Spichtinger, P. & Gierens, K. M. 2009 Modelling of cirrus clouds – Part 1a: Model description and validation. *Atmos. Chem. Phys.* **9** (2), 685–706.

Strang, Gilbert 1968 On the Construction and Comparison of Difference Schemes. *SIAM Journal on Numerical Analysis* **5** (3), 506–517.

Wedi, Nils P. 2006 The energetics of wave-driven mean flow oscillations. *International Journal for Numerical Methods in Fluids* **50** (10), 1175–1191.

Willoughby, H. E. 1990 Temporal Changes of the Primary Circulation in Tropical Cyclones. *Journal of the Atmospheric Sciences* **47** (2), 242–264.

Summary

The dynamics of atmospheric vortices play a great role in many environmental flow phenomena. When vortices experience vertical shear they persist, even intensify, or weaken, up to the point that they fade away. Identifying the parameters and conditions that lead to the respective scenarios is key to understanding the evolution of vortical flows in the atmosphere. Various temporal and spatial scales are involved and pose new challenges that simulations can help to resolve. We consider a numerical approach with the flow solver EULAG that has been successfully applied to a plethora of environmental systems, addressing the multi-scale behavior of the flow. A series of tests for two-dimensional setups is conducted first, borrowed from Klein (2009) and Kadioglu *et al.* (2008) to double-check EULAG's performance on concentrated vortical flows. A first application is the numerical implementation of precessing quasi-modes of three-dimensional atmospheric vortices. Their core structure and centerline change under environmental shear and are of particular interest for the overall evolution in time. Averaged measures are implemented in the code to extract these quantities from data without suffering from numerical oscillations. In a simple model an incipient hurricane is described by an axisymmetric, Gaussian vorticity profile, parameters are the radius of maximum wind and the corresponding wind speed. Modeling the hurricane on a finite grid requires zero velocity at the boundary, imitating an infinite domain, which we enforce with an appropriate mollifier. Instead of inducing shear flow we displace the vortex centerline initially, giving rise to a subsequent realignment phase of the vortex. Thereafter, the problem at hand is implemented and different initial shapes of the vortex centerline are discussed. Theoretical predictions lead us to an Eigenmode of the precession that is as well covered in the numerical experiment. Furthermore, the underlying model is supplemented with a diabatic heat source utilizing EULAG's design. Our choice of the heating term is based on the nonlinear matched asymptotic analysis for vortices with large tilt by Paeschke *et al.* (2012). Ultimately, our numerical study supports the asymptotic hurricane model and provides room for enhancement.

Zusammenfassung

Die Dynamik atmosphärischer Wirbel zu verstehen ist für viele Umweltphänomene von entscheidender Bedeutung. Ein Wirbel kann in vertikaler Scherströmung bestehen bleiben, verstärkt oder abgeschwächt werden. Eine besondere Herausforderung besteht darin die Parameter und Bedingungen zu bestimmen, unter denen die genannten Szenarien auftreten. Ihnen wird eine besondere Rolle bei der zeitlichen Entwicklung von Wirbelströmungen beigemessen. Dass verschiedene zeitliche und räumliche Skalen involviert sind, erschwert die Suche, mit Hilfe von Simulationen können jedoch viele Hindernisse überwunden werden. Wir beschäftigen uns mit dem numerischen Strömungslöser EULAG, der bereits mehrfach erfolgreich bei der Modellierung von Umweltprozessen angewandt wurde. Insbesondere berücksichtigt er auch das Multiskalenverhalten vieler Strömungen. Testreihen mit zweidimensionalen Problemstellungen nach einem Vorbild von Klein (2009) und Kadioglu *et al.* (2008) werden durchgeführt, um EULAGs Eignung und Leistung nochmals zu überprüfen. Eine erste Anwendung besteht in der Implementierung präzessierender Quasi-Moden dreidimensionaler atmosphärischer Wirbel. Unter dem Einfluss von Scherströmungen ändern sich ihre Zentrallinie und Kernstruktur, die für die weitere zeitliche Entwicklung von großem Interesse sind. Um sie anhand von Daten zu bestimmen wird der Code um einige Methoden erweitert, die sich auf gemittelte Größen beziehen und so numerische Oszillationen verringern. In einem einfachen Modell beschreiben wir einen entstehenden tropischen Wirbelsturm mit einer achsensymmetrischen Gaußkurve, die die Wirbelstärke repräsentiert. Wichtige Größen sind die maximale Windgeschwindigkeit und der dazugehörige Radius. Um ein unendlich ausgedehntes Gebiet zu imitieren wird das Geschwindigkeitsprofil in der Nähe des Randes mit einer glatten Funktion bis auf Null herunter gesetzt. Anstatt den Wirbel einer Scherströmung auszusetzen verschieben wir vor dem ersten Zeitschritt seine Zentrallinie und beobachten die Neuausrichtung. Verschiedene Startprofile werden implementiert und diskutiert. Auf der Grundlage eines theoretischen Modells finden wir auch in unserem numerischen Experiment eine Eigenmode der Präzession. Wir erweitern unser Modell, sodass es den Einfluss von Wärmequellen berücksichtigt und machen dabei von EULAGs Aufbau Gebrauch. Die diabatischen Terme werden auf Grundlage asymptotischer Analyse von Paeschke *et al.* (2012) bei Wirbeln mit großer Auslenkung angewandt. Schlussendlich steht unser numerisches Modell im Einklang mit dem asymptotischen Modell eines Wirbelsturms und bietet neuen Raum für Erweiterungen.

Der Lebenslauf ist in der Online-Version aus Gründen des Datenschutzes nicht enthalten.